MEASUREMENT, MODELING, AND PERFORMANCE OF INDOOR MIMO CHANNELS

A Dissertation
Presented to
The Academic Faculty

By

Jeng-Shiann Jiang

In Partial Fulfillment
Of the Requirements for the Degree
Doctor of Philosophy in
Electrical and Computer Engineering

School of Electrical and Computer Engineering
Georgia Institute of Technology

July 2004

MEASUREMENT, MODELING, AND PERFORMANCE OF INDOOR MIMO CHANNELS

Approved:

Professor Mary Ann Ingram, Chairman

Professor Douglas B. Williams

Professor Aaron Lanterman

Date approved by Chairman:

To my family

ACKNOWLEDGMENT

Pursuing a Ph.D. degree is so far the most difficult mission for me. During this twilight-zone-like period, sometimes I felt that life is similar to a “digital system” because the way it repeats itself resembles the cyclic repeating pattern of the frequency response. I hope life could be easier, but fact is it never is. Probably the only way to possess an easy life is to have a pure and simple mind, which is hard to come by. However, in every stage of my life there are always friends who help me out and make life easier. There is an old Chinese saying: “People’s aid, good timing, and right place are three indispensable factors to any success.” I believe so. This dissertation would have not been possible without the help and support from many people. I would like to express my appreciation to my friends from the bottom of my heart.

First I would like to thank my advisor, Dr. Mary A. Ingram for her intellectual guidance, thoughtful comments, and valuable suggestions. She offered me an opportunity to participate in the array-to-array project, and let me use the most expensive measurement system of our laboratory. She treats her students like friends. I will never forget her encouragement and thoughtful advice when I encountered a bottleneck in research in my low period. I also want to express my gratitude to Dr. Douglas B. Williams, Dr. Aaron Lanterman, and Dr. John R. Barry for serving as my reading committees and for their recommendations and inputs for the improvement of the dissertation. My appreciation extends to Dr. John A. Copeland, Dr. Alfred D. Andrew, and Dr. Paul G. Steffes who serve in my supervisory committee.

I also want to thank the students in the Smart Antenna Research Laboratory for their comments, technical discussions, encouragement, and for helping me on the measurement. They are Guillermo Acosta, Nuray At, Fatih Mehmet Demirkol, Lu Dong, Vijay Ganugapati, Sudhanshu Gaur, Daeyoung King, Dong Kyoo, Kuo-Hui Li, Anh, Nguyen, Kathleen Tokuda, Muhammad Usman, Rafa Vano, and Joseph Varachi. I would like to thank Fatih Mehmet Demirkol again for his collaboration on one of my conference papers. Special thanks go to the people who contributed to the successful integration of the MIMO measurement system. Ms. Zhijie Xiong, the predecessor of my project, laid the initial groundwork. Mr. Lorand Csiszar, James Nowell, and Louis Boulanger, the best technologists of our department, built a terrific mobile platform for us. Ms. Cordai Farrar, the most efficient secretary in the GCATT building, helped me contact the manufacturer and deal with many trivial things.

I am grateful to my friends in Taiwan's Student Organization for their friendship. Especially, I want to thank Chi-Ti Hsieh, Hung-Yun Hsieh, Jeng-Fang Li, who helped me in my most difficult time. Finally, I would like to acknowledge my parents, sister, and brothers for their endless support and encouragement.

J-S. Jiang

TABLE OF CONTENTS

LIST OF FIGURES

LIST OF TABLES

SUMMARY

The objective of this dissertation is to investigate the capacity performance of the recently proposed multiple-input multiple-output (MIMO) technology in real indoor environments based on channel measurements centered at 5.8 GHz. First, a MIMO channel sounding system is implemented based on the virtual antenna array infrastructure. This measurement testbed is used to acquire the wideband channel matrices of MIMO systems with arbitrary array geometries. Moreover, the mutual coupling effect, which may cause parameter estimation error, is avoided in our measurement testbed because only a single antenna is employed at each end of the communication link.

Characterization of the MIMO channel requires the statistics of the DOA and DOD of each multipath. These statistics are acquired with high-resolution estimation algorithms, such as multiple signal classification (MUSIC) and the estimation of signal parameters via rotation invariance technique (ESPRIT). The ESPRIT algorithm is employed for parameter estimation in this research because it is robust to sensor location disturbances and its computational complexity is low compared to the other estimation algorithms. The DOA, DOD, and the excess delay parameters have been estimated in sequence, jointly, and in a hybrid way by other research groups. However, they used a uniform linear array or a cross array with few antennas, which has the drawbacks of estimation ambiguity, lower angular resolution, and few number of detectable paths. The discrepancy between the measured and estimated capacities is severe in their measurement results. In our measurement system, we employ 3-dimensional virtual

antenna arrays with a great number of elements, which eliminates the ambiguity problem, increase the angular resolution and increase the number of detectable paths. In order to determine which estimation scheme has highest accuracy, schemes are applied to the measured channels, and compared in terms of the discrepancy between the directly measured and the reconstructed channel capacities. We claim that separate delay estimation followed by joint estimation of DOA and DOD is the most suitable for the estimation of MIMO channel parameters.

One problem with the ESPRIT algorithm is that it assumes the number of paths is *a priori* knowledge. Such knowledge is usually unavailable in real applications. Two novel number-of-paths detection algorithms, the residual estimation error (REE) and variance of transformed rotational submatrix (VTRS) algorithms, are proposed to resolve this issue. The REE algorithm must estimate the parameters as well to detect the number of them. The VTRS detection algorithm, on the other hand, does not require estimation and therefore has lower complexity than REE. We claim that the VTRS detection algorithm is very robust to measurement distortion caused by sensor location disturbances or by element pattern variations in the array, and its low computational complexity makes this algorithm suitable for real-time applications.

In wireless communications, the signal is conveyed on an electromagnetic wave, which is propagated as spherical wave from a point source. However, at a long distance from the source, the spherical wave is approximated as a plane wave for the convenience of analysis. This dissertation claims that the plane wave assumption causes significant underestimation of MIMO channel capacity when the distance of the communication link is short. This situation corresponds to a link geometry that we denote as short-range

MIMO. The short-range MIMO communication link can result in a full-rank channel matrix in free space and thus can achieve the maximum channel capacity. Even when multipath is present with the LOS, the LOS component usually dominates link performance and therefore the LOS must be modeled correctly. The short distance is comparable to distances that are found in home wireless local area networks (WLAN). A threshold distance is proposed to determine whether the spherical wave model is necessary to avoid the performance underestimation. Comparisons of directly measured capacities and capacities of channels based on estimated geometrical parameters show the importance of the spherical wave model in predicting capacity performance.

Measurements conducted in the Residential Laboratory at the Georgia Institute of Technology are used to investigate the impact of element spacing on MIMO channels. The effects of element spacing are strongly dependent upon several factors, such as the availability of LOS component, presence of MIMO interference, spatial correlation between the interfering and data links, and stream control. For example, MIMO capacity is sensitive to the element spacing when LOS is available; significant improvement is observed by increasing the spacing from 0.5 to 2λ. However, this sensitivity to element spacing is reduced when the LOS is blocked. We claim that we are the first to investigate the effects of MIMO interference using the measured data. Our measurement results demonstrate that stream control plays a crucial role in the throughput of the channels with MIMO interference. In addition, the throughput can be improved by increasing the element spacing only when stream control is employed.

Realizing the impact of the array geometry to MIMO capacity, we propose a capacity enhancement scheme that improves the MIMO channel capacity by adapting the

element locations according to the steepest descent algorithm. According to the measurement results, the capacity can be improved by up to 129%.

The final part of the dissertation investigates beam selection and antenna selection. These two schemes improve MIMO performance under the constraint of a reduced number of RF chains. The measurements obtained in the Residential Laboratory are employed to compare the performances of these two selection schemes in both narrowband and wideband channels. Channels with and without MIMO interference are considered. This dissertation claims that when MIMO interference is present, beam selection outperforms antenna selection if the selection is performed at both ends of the link. However, if proper stream control is included, primary throughput improvement comes from the interference suppression provided by stream control, and the difference between these two selection schemes is significantly reduced.

Chapter 1

Introduction

With the popularity of wireless communications in our daily lives, the demand of wireless communication products supporting data transmission has increased drastically. Speedy downloads of large files and some applications, such as multimedia streaming video and internet conferencing, need a high volume of data transmission. As a consequence, the development of novel technologies to meet the high data rate requirement in wireless communications has drawn tremendous attention. Traditionally, the increasing data rate is accomplished either by increasing the bandwidth or by employing more spectrally efficient modulation. Examples in this category include orthogonal frequency division multiplexing (OFDM), multi-carrier code division multiple access (MC-CDMA), and wideband CDMA (WCDMA). These technologies have been employed in many 3G mobile cellular services as well as indoor wireless local area networks (WLAN) like IEEE 802.11a, IEEE 802.11g, and HIPERLAN/II. Another approach to increasing the data rate is to exploit the spatial domain. In this category, the high data rate is achieved by creating multiple channels in space with multiple antennas at both the transmitter and the receiver sites [1,2,3]. Theoretically, in this multiple-input multiple-output (MIMO) technology, multiple co-channel data streams can be transmitted simultaneously and the data rate is proportional to the number of minimum number of antennas at the transmitter and receiver ends of the link [1,3]. The objective of this

dissertation is to investigate the performance of MIMO technology in real indoor environments based on measurements centered at 5.8 GHz.

MIMO, or spatially multiplexed, wireless links, have received a great deal of attention because they can provide extremely high spectral efficiency in rich multipath environments [1]. Many of these studies are concerned with the Shannon capacity of the flat-fading MIMO link and most are based on simulated channels [2,4]. Although MIMO systems possess unprecedented performance in independently, identically distributed (i.i.d) Rayleigh channels, it has been revealed that some factors such as correlation and interference may significantly degrade the performance [4,5,6,7,8,9,10]. The theoretical technologies or analyses need to be validated before being applied to the design of the practical systems like WLAN, personal area network (PAN), and Home RF.

More parameters are required to characterize a MIMO channel than are required to characterize traditional single-input single-output (SISO), single-input multiple-output (SIMO), or multiple-input single-output (MISO) channels [11]. The SISO channel is characterized by number of paths of propagation and by the delays and complex amplitudes of the paths. Additionally, SIMO or MISO requires the direction of arrival (DOA) or direction of departure (DOD), respectively. Characterization of the MIMO channel requires estimation of all of the above parameters.

The angular parameters are acquired with either highly directional antennas or sophisticated parameter estimation algorithms such as multiple signal classification (MUSIC) and the estimation of signal parameters via rotation invariance technique (ESPRIT) [12,13]. Inaccurate parameter estimation will lead to incorrect channel modeling and performance evaluation. For MIMO channels, the requirement of both

DOA and DOD results in higher computational complexity in the estimation procedure and increased cost and difficulty of the implementation of the channel measurement system than for SISO, MISO, or SIMO channels..

Our MIMO channel sounding system is based on the virtual antenna array, which is an array created by moving a single antenna from place to place with an actuator. Virtual arrays have the advantages of lower cost, immunity to the mutual coupling effect, and the ability to measure MIMO channels with arbitrary array geometries. Their disadvantages are the requirement of a stationary environment and long measurement time.

The ESPRIT algorithm is employed for the parameter estimation in this research because it is robust to sensor location disturbances and variations, and its computational complexity is low compared to the other estimation algorithms. Other research groups have proposed several estimation schemes based on ESPRIT algorithms, including the sequential estimation [14,15], joint estimation [16], and hybrid estimation. In order to determine which estimation scheme is most appropriate for characterization of MIMO channels, these schemes are applied to the measured channels, and their estimation accuracies are compared in terms of the discrepancy between the directly measured and the reconstructed channel capacities.

In estimation algorithms, the number of sources is usually assumed to be a known value. However, this value is usually unavailable in reality and needs to be detected before performing the estimation. Minimum description length (MDL) and Akaike's information criterion (AIC) are two traditional algorithms for the detection of number of sources [17,18,19]. However, these two methods are sensitive to the measurement

distortions caused by element gain variations, and by imperfect element spacing of the arrays when spatial smoothing is involved to decorrelate signal sources. To resolve these problems, we propose two robust algorithms to detect the number of signals; one is based on the residual estimation error (REE), and the other is based on the variance of the transformed rotational submatrix (VTRS).

Furthermore, we discuss the impacts of two propagation channel models, the plane wave model and the spherical wave model, on the performance of MIMO channels. In wireless communications, the signal is conveyed on an electromagnetic wave, which is propagated as spherical wave from the point source. At a long distance from the source, the spherical wave is usually approximated as a plane wave for the convenience of analysis [20,21]. We demonstrate how the plane wave assumption causes significant underestimation of MIMO channel capacity when the distance of the communication link is short, a link geometry that we denote as short-range MIMO. Moreover, a threshold distance is provided to determine whether the spherical wave model is necessary to avoid severe performance underestimation. The results are validated by measurement, estimation, and reconstructed capacities with both plane and spherical wave models.

Another part of this dissertation is devoted to investigating the influence of array geometries, particularly the element spacing, on the performance of flat-faded MIMO channels with or without interference. We demonstrate that sensitivity of the capacity to antenna spacing depends on the existence of LOS and the range of the communication link. When the LOS component is available at short-range, wider spacing (up to 3λ in our measurement) provides better performance. When the LOS is obstructed, the performance improvement tends to saturate at spacing 0.5λ. We also show that for

interfering MIMO links, wider antenna spacing is best only when there is stream control, which reduces the number of transmitted data streams to prevent the receiver from being overwhelmed by the interference caused by other MIMO users. We are the first to use measured channels to investigate the impact of MIMO interference on the throughput of MIMO networks. In addition, using our virtual antenna arrays we investigate the MIMO system in which the antennas move adaptively to improve the capacity. Improvements of up to 129% are observed.

The last part of the dissertation addresses beam selection and antenna selection. There are two schemes that improve MIMO performance under the constraint of a reduced number of RF chains. When the selection is only applied at the transmitter site, it is one realization of stream control. The measurements obtained in the Residential Laboratory are employed to compare the performances of these two selection schemes in both narrowband and wideband channels. Both the channels with and without MIMO interference are considered. According to the measurement results, when MIMO interference is present, beam selection outperforms antenna selection if the selection is performed at both ends of the link. However, if proper stream control is included, primary throughput improvement comes from the interference suppression provided by stream control, and the difference between these two selection schemes is significantly reduced.

The remainder of the thesis is organized as follows. In Chapter 2, the backgrounds on MIMO channel technology, channel characterization, parameter estimation as well as number-detection algorithms, and beam and antenna selection are provided. A variety of current MIMO channel sounding systems are also described. Chapter 3 describes the

details of our MIMO channel measurement system, which comprises the HP85301B stepped-frequency antenna pattern measurement system and the 3D actuator system. The measurement and calibration procedure are also described in this chapter. The results of two preliminary experiments are demonstrated to show the stability of the measurement environment and the validity of the virtual antenna array. Chapter 4 addresses the number-of-sources detection algorithms. Two novel detection algorithms, the REE and the VTRS detection algorithms, are proposed. Chapter 5 is devoted to the comparison of various parameter estimation schemes based on the ESPRIT and Fourier transform. In Chapter 6, we illustrate the performance underestimation resulted from inappropriate plane wave assumption for short-range MIMO systems. A threshold distance is proposed here to determine whether or not the more accurate spherical wave model should be considered in evaluating or simulating MIMO channels. Chapter 7 deals with several critical factors that may significantly affect the performance of MIMO channels, including element spacing, availability of LOS component, presence of MIMO interference, the spatial correlation level between the signal and the interfering links, and stream control. The performances of beam selection and antenna selection schemes are compared in Chapter 8. Finally, the contributions of this dissertation are summarized and the future work is suggested in Chapter 9.

Chapter 2

Background

This chapter provides the background for this research. First, we introduce the MIMO technology with emphasis on the channel capacity of MIMO systems. This MIMO capacity, which is used to evaluate the performance of MIMO channels throughout the thesis, is the highest achievable data rate of any MIMO system, so no specific implementation of MIMO system is assumed. Next, we describe parameter estimation algorithms with special attention to the details of the ESPRIT estimation algorithm and its extension to multi-dimensional estimation, which will be employed in Chapter 5 to derive the angular information of multipath from measured data.

The detection of number of sources is a prerequisite in many parameter estimation algorithms. A survey of the detection of number of sources is addressed, and the MDL detection algorithm, which will be compared with the detection algorithms we proposed in Chapter 4, is discussed in detail. At last, the advantages and disadvantages of various MIMO channel sounding systems are discussed.

2.1 MIMO Technology

A MIMO wireless communication link utilizes multiple antennas at both end of the link to virtually create multiple parallel channels. With this architecture, multiple data streams can be transmitted simultaneously at the same time and frequency, and they can

be separately demodulated at the receiver end. As shown in Figure 1, the number of parallel channels or in other words, data streams, is equal to min(n_T, n_R), where n_T and n_R are the numbers of antennas of the transmit and receive arrays, respectively [1].

The signals transmitted in a MIMO link can be coded across time and antennas using, as examples, the Vertical Bell-Labs-Layer-Space-Time (VBLAST) algorithm or Alamouti's space-time block code [22,23]. However, in this dissertation no specific space-time coding is assumed; instead, we evaluate the performances of MIMO channels in terms of Shannon's channel capacity.

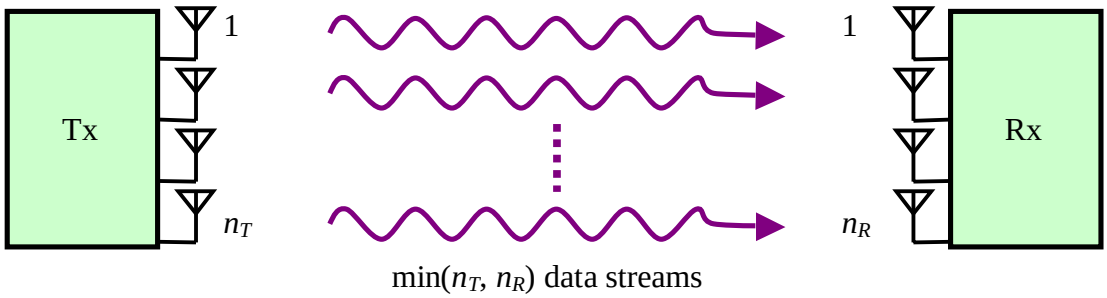

Figure 1: MIMO system with multiple antennas at both ends of the communication link. The number of parallel data streams is equal to the minimum of the number of antennas at both ends, i.e. min(n_T, n_R).

Shannon's channel capacity, defined as the maximum data rate at which the information can be transmitted without errors, is usually used to evaluate the potential of the communication channel [24]. To compute the channel capacity, a signal model is required. Assuming a flat fading channel, the general signal model for a (n_T, n_R) MIMO channel is

$$\mathbf{Y} = \mathbf{HX} + \mathbf{n}, \tag{1}$$

where $\mathbf{X} \in \mathcal{C}_{n_T \times 1}$ and $\mathbf{Y} \in \mathcal{C}_{n_R \times 1}$ are the transmitted and received array signals, respectively. $\mathbf{H} \in \mathcal{C}_{n_R \times n_T}$ is the MIMO channel matrix, and $\mathbf{n} \in \mathcal{C}_{n_R \times 1}$ is the additive white Gaussian noise.

In this dissertation we consider only open-loop MIMO (OL-MIMO), which means that the channel information is not fed back to the transmitter, and that independent data streams are transmitted out of each antenna with equal power. With these assumptions, the OL-MIMO capacity of the channel without interference is calculated according to [1]

$$C = \log_2 \left| \mathbf{I}_{n_R} + \frac{\rho}{n_T} \mathbf{H}\mathbf{H}^{\dagger} \right|. \tag{2}$$

where ρ is the SNR, † stands for the complex conjugate transpose of the matrix, and the MIMO complex channel matrix **H** is normalized such that the components of **H** have unit variance. A popular statistical model for a rich multipath NLOS channel is the i.i.d. Rayleigh channel. In this model, the elements of **H** are i.i.d. zero mean, spherically symmetric, complex Gaussian random variables. Since **H** is random, *C* is also random. Link performance can be quantified in terms of ergodic capacity and the cumulative distribution function (CDF) of the capacity. The ergodic capacity is defined as the average capacity of many realizations of the random channels.

Figure 2 illustrates the average capacities over 1000 trials of i.i.d. SISO, SIMO, and MIMO Rayleigh fading channels. The number of antennas is 4 at the receiver end of SIMO channel, while 4 antennas are employed at both ends in MIMO channel. Although SIMO has better performance than SISO, the primary improvement results from improved SNR and spatial diversity; ranks of the channel matrices are the same and slopes of both curves are equal to 1 bit/s/Hz per 3dB at high SNR. For MIMO channels, the slope of the curve is 4 bits/sec/Hz per 3dB, which is equal to the number of parallel data streams.

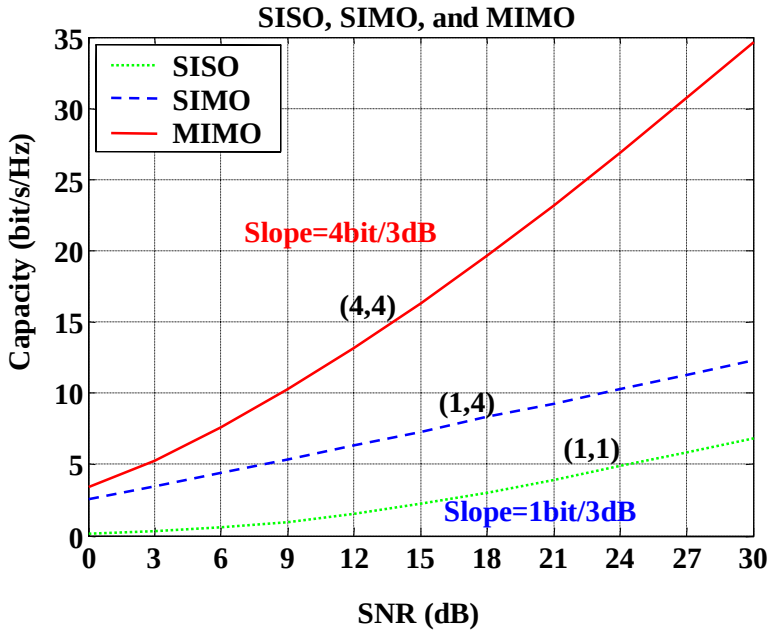

Figure 2: Performance comparison of SISO, SIMO, and MIMO channels. At higher SNR, the performances of SISO and SIMO increases by 1 bit/sec/Hz per 3dB; the performance of MIMO increases by 4 bits/sec/Hz per 3dB. In each case, the slope is equal to the effective rank of the channel matrix.

Although the MIMO technology provides unprecedented channel capacity in an ideal i.i.d. Rayleigh channels, it has been revealed that the MIMO channel capacity may be significantly degraded by many environmental factors. In fact, the MIMO channel capacity is a function of the singular values of the channel matrix. In [25] and [26], the authors proved that under the constraint of the same transmit power, the MIMO capacity achieves its maximum when all singular values of the channel matrix are identical at high SNR condition. In other words, at high SNR the maximum capacity corresponds to the flat singular value distribution. On the other hand, at low SNR the maximum capacity is achieved when there is only one nonzero singular value, which corresponds to the condition where single beam is formed by properly adjusting the weights of transmit and receive antennas.

Since the MIMO channel capacity is a function of the singular values, the capacity may be significantly influenced by the environmental factors that can change the distribution of the singular values. The effects of many environmental factors on the channel capacity, including the spatial correlation between the antennas [27,28], array geometry [27,29,30,31,32], antenna polarization [28,30], and interference [5,33], have been investigated by many research groups.

The capacity of the channels with interference was addressed in [5]. With the presence of interference, the capacity is calculated by

$$C_{\text{int}} = \log_2 \left| \mathbf{I}_{n_R} + \frac{\rho}{n_T} \tilde{\mathbf{H}} \tilde{\mathbf{H}}^{\dagger} \right| \qquad \tilde{\mathbf{H}} = (\mathbf{I} + \mathbf{R}_{\text{int}})^{-1/2} \mathbf{H}, \tag{3}$$

where $\tilde{\mathbf{H}}$ is the whitened channel matrix, and $\mathbf{R}_{\text{int}}$ is the spatial correlation matrix of the interference. The authors also show that the distribution of the singular values is truncated when external interference is present. To be specific, the number of truncated singular values is equal to the number of external interferences, which is caused by the overlap of the signal and interference subspaces. The truncation of the singular value distribution implies the reduction of the rank of the channel matrix or the number of data streams, which in turn, degrades the MIMO capacity dramatically. When the number of total streams, including the desired data and interference streams, is larger than the number of receive antennas, the rank of the whitened channel matrix achieves zero at high SNR, which means the capacity can not improved by increasing the SNR. In this condition, the receiver is *overwhelmed*. This overwhelming situation can be avoided by applying stream control [34,35,36], which deliberately reduces the number of transmitted data streams such that the number of receive antennas is larger than the total number of

streams. Physically the stream control can be implemented by either antenna selection [37,38,39] or beam selection [40,41]. The total channel capacity, the SINR, or some other factors can be used as the selection criterion, depending on the application and allowed complexity of the system.

Antenna selection improves the performance by selecting the MIMO antenna elements from among a larger set of elements at one or both ends of a link [37,38]. An older technology, the switched-beam RF beamforming, which has simple implementations like the Butler matrix [40,41], have drawn tremendous attention in the arena of cellular systems because of their superior interference suppression feature and the space division multiple access (SDMA) capability. Both technologies require a many-to-few switch matrix, which has a considerably more complex implementation than the Butler matrix. By simply inserting a multibeam RF beamformer (like a Butler matrix) between the antennas and the switch, as shown in Figure 3, a MIMO link with antenna selection can be changed into a MIMO link with beam selection. Beam selection is expected to be better than antenna selection in a frequency selective channel because path angles, and therefore best beams, are not very sensitive to frequency, while small scale fading effects, and therefore the best antennas, are sensitive to frequency.

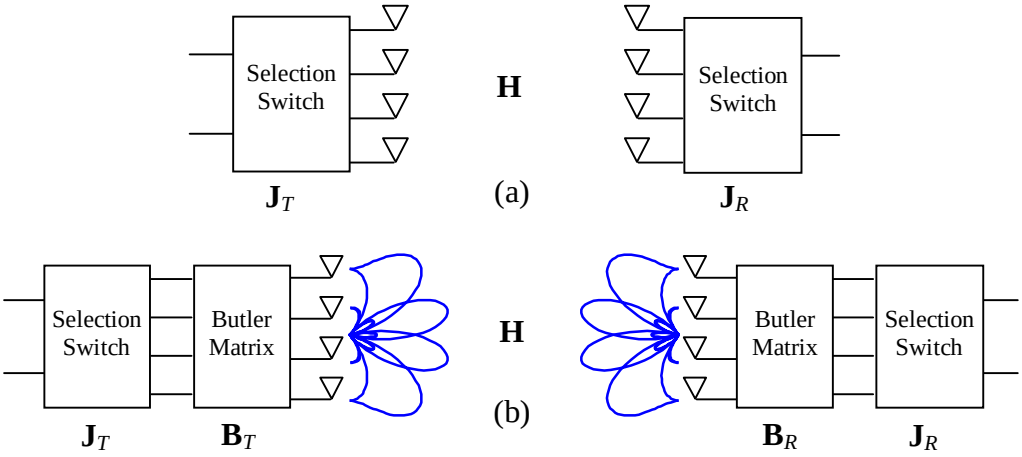

Figure 3: System overview. (a) Antenna Selection. (b) Beam Selection.

Let N_T and N_R denote the total numbers of transmit and receive antennas, respectively, and let n_T and n_R stand for the numbers of selected transmit and receive antennas, respectively. The channel matrix, $\mathbf{H}$, is an $N_R \times N_T$ matrix, which is noise-normalized before being further employed by the beam and antenna selection method. The MIMO channel matrices after antenna selection and beam selection are given by

$$\mathbf{H}_{ant} = \mathbf{J}_R \mathbf{H} \mathbf{J}_T^{\dagger} \tag{4}$$

and

$$\mathbf{H}_{beam} = \mathbf{J}_R \mathbf{B}_R \mathbf{H} \mathbf{B}_T \mathbf{J}_T^{\dagger}, \tag{5}$$

respectively, where $\mathbf{J}_R \in \mathcal{R}_{n_R \times N_R}$ and $\mathbf{J}_T \in \mathcal{R}_{n_T \times N_T}$ are the lossless selection matrices at both ends, $\mathbf{B}_R = [B_R^1 \; B_R^2 \cdots B_R^{N_R}] \in \mathcal{C}_{N_R \times N_R}$ and $\mathbf{B}_T = [B_T^1 \; B_T^2 \cdots B_T^{N_T}] \in \mathcal{C}_{N_T \times N_T}$ are the lossless receive and transmit Butler matrices. The m^{th} columns of $\mathbf{B}_R$ and $\mathbf{B}_T$ are

$$B_R^m(n) = \frac{1}{\sqrt{N_R}} \exp\left\{\frac{j\pi(m-1)[-(N_R-1)+2(n-1)]}{N_R}\right\}, n = 1 \cdots N_R \tag{6}$$

$$B_T^m(n) = \frac{1}{\sqrt{N_T}} \exp\left\{\frac{-j\pi(n-1)[-(N_T-1)+2(m-1)]}{N_T}\right\}, n = 1 \cdots N_T . \tag{7}$$

The comparison of beam and antenna selection will be addressed in Chapter 8. In the dissertation, the beams or antennas are selected to maximize the channel capacity.

2.2 Parameter Estimation Algorithms

Each path in a SISO link is fully described by its excess delay and complex gain. However, for SIMO and MISO links the DOA and DOD respectively are also needed to fully characterize the channels. For MIMO links, however, both the DOA and DOD of each path are required. The derivation of DOAs and DODs of multipath calls for sophisticated parameter estimation algorithms. Moreover, in an indoor environment, the paths can be very close to each other in delay or angle because of rich scattering. In consequence, high-resolution estimation algorithms are required to resolve close multipaths. To sum up, the parameter estimation methods that are suitable for a MIMO measurement system should meet the following requirements:

- High resolution capability to resolve close paths
- Multiple-parameter estimation (delay, complex gain, and 3-D angle estimation, i.e. azimuth and elevation-angle estimation without ambiguity)
- Practical computational complexity for large array size

Current DOA estimation techniques are categorized into three classes in [42,43]: (1) *Spectral-based methods*, (2) *Subspace-based methods*, and (3) *Parametric methods*. The *spectral-based methods* compute the cost function, which is a function of the parameters, and take the values corresponding to the peaks of the cost function as the estimates. A main disadvantage of this method is its intensive computational complexity

for multiple parameter estimation where a multidimensional search is required to determine the peaks of the cost function. The beamforming [44] and the MUSIC algorithm [12] are two representatives of this category. The *subspace-based methods* make use of the algebraic properties of the eigenspace of the signals and noise to estimate the parameters. The primary feature of this category is its low computational complexity achieved by avoiding the search of the peaks. The root-MUSIC [45,46] and the ESPRIT algorithm [13,47,48,49] belong to this category. The *parametric methods*, which use the maximum likelihood function to estimate the parameters, have better performance than the other two categories. However, the optimization of the likelihood function needs a multi-dimensional search, which requires higher computational complexity.

The resolution capability of the beamforming technique depends on the size of the array aperture; therefore, this method is not suitable for this research because the apertures of the arrays in our measurement are small. Although the MUSIC algorithm and the parametric methods have superior resolution capability, the high computational complexity of the multidimensional search for multiple parameters makes them impractical for joint estimation of multiple parameters. The root-MUSIC algorithm replaces the peak-search procedure of MUSIC by resolving the roots of linear functions, but this method can only be applied to the one-dimensional uniform linear array (ULA), from which only azimuth angle can be obtained. The ESPRIT algorithm is a robust method with high resolution capability and low computational complexity. The unitary ESPRIT is a modified version of ESPRIT that improves the performance of ESPRIT while reducing the computational complexity [47]. The multi-dimensional ESPRIT, on the other hand, is an extension of ESPRIT that is capable of jointly estimating multiple

parameters of the signal sources [48,49]. Accordingly, we select the ESPRIT algorithm as the tool to extract the MIMO path parameters from the measured data. With multi-dimensional ESPRIT algorithm, we may obtain the estimates of complex gains, delays, DOAs, and DODs of the multipaths simultaneously. In the following subsections, we describe the theories of the ESPRIT [13], unitary ESPRIT [47], and multi-dimensional ESPRIT algorithms [49].

2.2.1 ESPRIT Estimation Algorithm

ESPRIT is a high-resolution estimation method with low computational complexity [13]. ESPRIT algorithms have been applied to not only angle estimation [13], but also delay estimation [50] or joint estimation of these parameters [51,52]. For convenience, we take angle estimation as an example to introduce the details of the ESPRIT algorithm. However, the algorithm can be applied to delay estimation or harmonic frequency retrieval naturally by modifying the format of the steering vector, which is a function of the parameter of interest. The improvement of the accuracy using unitary ESPRIT, and the extension to multi-dimensional estimation will be described in the next two subsections.

The signal model for the angle estimation problem is

$$\mathbf{Y} = \sum_{m=1}^{L} \mathbf{a}(\theta_m) s_m + \mathbf{n} = \mathbf{A}(\boldsymbol{\theta})\mathbf{s} + \mathbf{n}, \tag{8}$$

where $\mathbf{Y} \in \mathcal{C}_{N\times 1}$ is the array signal, N is the number of elements of the array, L is the number of paths, $\mathbf{s} = [s_1\ s_2\ \ldots\ s_L]^T$ are the complex gains of L multipaths, $\mathbf{n}$ is the noise vector, and $\mathbf{a}(\theta_m)$ is the steering vector of the m^{th} multipath impinging from the direction

θ_m. The steering matrix **A(θ)**, also called the array manifold, is composed of L steering column vectors, i.e

$$\mathbf{A}(\boldsymbol{\theta}) = [\mathbf{a}(\theta_1) \quad \mathbf{a}(\theta_2) \quad \mathbf{a}(\theta_3) \quad \cdots \quad \mathbf{a}(\theta_L)]. \tag{9}$$

The structure of the steering vector $\mathbf{a}(\theta_m)$ depends on θ_m, array geometry, and signal wavelength λ. As an example, for an N-element ULA with element spacing d_x, the steering vector is

$$\mathbf{a}(\theta_m) = [1 \quad e^{iu_m} \quad e^{i2u_m} \quad \cdots \quad e^{i(N-1)u_m}]^T, \text{ where } \quad u_m = \frac{2\pi d_x}{\lambda}\cos\theta_m \tag{10}$$

The spatial correlation matrix of the received array signal **Y** is defined as

$$\mathbf{R}_{yy} = E\{\mathbf{Y}\mathbf{Y}^{\dagger}\}, \tag{11}$$

where $E\{\bullet\}$ denotes expectation value. The generalized eigen-decomposition of the spatial correlation matrix $\mathbf{R}_{yy}$ with noise variance σ^2 and normalized noise correlation matrix $\mathbf{R}_{nn}$ is

$$\begin{cases} \mathbf{R}_{yy}\mathbf{E} = \mathbf{R}_{nn}\mathbf{E}\boldsymbol{\Lambda} \\ \mathbf{E}^{\dagger}\mathbf{R}_{nn}\mathbf{E} = \mathbf{I} \end{cases}, \tag{12}$$

where **E** denotes the generalized eigenvectors, and $\boldsymbol{\Lambda} = \text{diag}\{\zeta_1, \zeta_2, \zeta_3, \cdots, \zeta_N\}$, where $\{\zeta_m \mid m = 1, \cdots, N\}$ are the generalized eigenvalues of $\mathbf{R}_{yy}$ with $\zeta_1 \geq \zeta_2 \geq \zeta_3 \geq \cdots \geq \zeta_N$. According to (8), the spatial correlation matrix is

$$\mathbf{R}_{yy} = E\{\mathbf{Y}\mathbf{Y}^{\dagger}\} = \mathbf{A}\mathbf{R}_{ss}\mathbf{A}^{\dagger} + \sigma^2\mathbf{R}_{nn}. \tag{13}$$

Replacing $\mathbf{R}_{yy}$ in (12) by (13), we obtain that

$$\begin{aligned} \mathbf{R}_{yy} &= \mathbf{R}_{nn}\mathbf{E}\boldsymbol{\Lambda}\mathbf{E}^{\dagger}\mathbf{R}_{nn} \\ \mathbf{A}\mathbf{R}_{ss}\mathbf{A}^{\dagger} &= \mathbf{R}_{nn}\mathbf{E}\left[\boldsymbol{\Lambda} - \sigma^2\mathbf{I}\right]\mathbf{E}^{\dagger}\mathbf{R}_{nn}. \end{aligned} \tag{14}$$

With L non-coherent signal sources, the rank of $\mathbf{AR}_{ss}\mathbf{A}^{\dagger}$ is equal to L. The eigenvalues of $\mathbf{AR}_{ss}\mathbf{A}^{\dagger}$ are corresponding to the largest L eigenvalues of $\mathbf{R}_{yy}$. Assuming $\{\mathbf{e}_m \mid m = 1, \cdots, N\}$ are the eigenvectors with corresponding eigenvalues $\{\zeta_m \mid m = 1, \cdots, N\}$, $\mathbf{R}_{yy}$ can be decomposed into the signal subspace and the noise subspace, i.e.

$$\mathbf{R}_{yy} = \mathbf{E}_s \mathbf{\Lambda}_s \mathbf{E}_s^{\dagger} + \sigma^2 \mathbf{E}_n \mathbf{E}_n^{\dagger}, \tag{15}$$

where $\mathbf{E}_s = \mathbf{R}_{nn}[\mathbf{e}_1\ \mathbf{e}_2\ \mathbf{e}_3\ \cdots\ \mathbf{e}_L]$ span the signal subspace and $\mathbf{\Lambda}_s = \text{diag}\{\zeta_1, \zeta_2, \zeta_3, \cdots, \zeta_L\}$. In many applications, the noise at different sensors are uncorrelated, and the spatial correlation matrix of noise $\mathbf{R}_{nn} = \mathbf{I}$. In this situation, the generalized eigen-decomposition in (12) is simplified to eigen-decomposition.

The idea of the ESPRIT algorithm is to investigate the rotational invariance property of two identical subarrays with the same array geometry, as shown in Figure 4. The locations of the second subarray elements are a constant displacement d_x of the corresponding elements of the first subarray. Although the array geometry can be arbitrary, the ULA is usually employed to reduce the total number of elements by overlapping two subarrays, as shown in Figure 4.

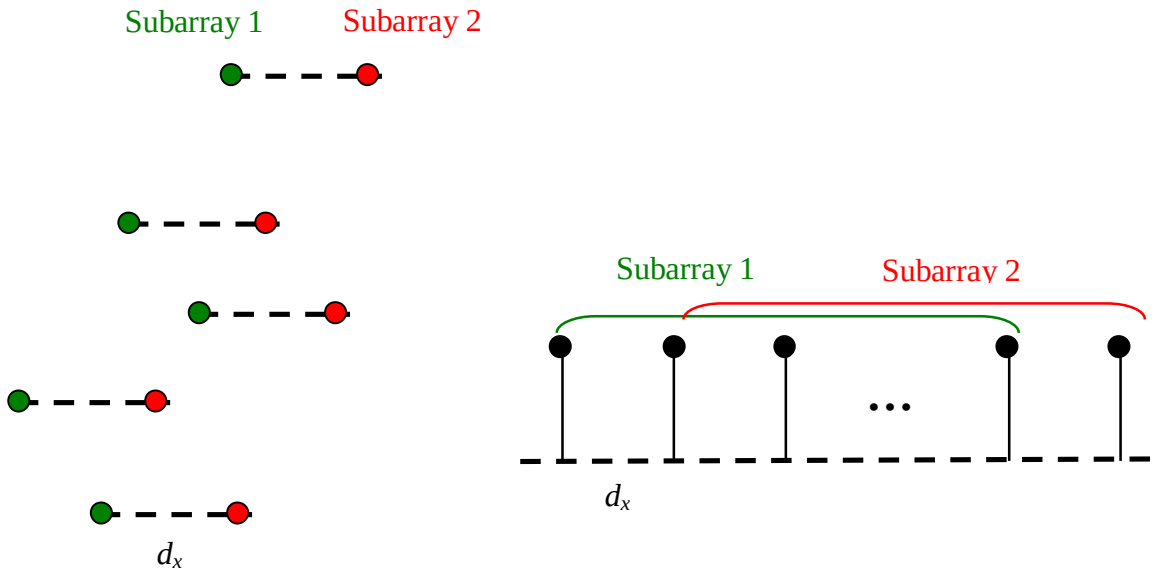

Figure 4: (a) The idea of ESPRIT is to investigate the rotational invariance property of two identical subarrays to estimate the parameter. (b) The number of required sensors can be reduced by overlapping two subarrays with uniform element spacing.

For ULA, the selection matrices $\mathbf{J}_1$ and $\mathbf{J}_2$ defined in (16) can be used to choose the elements of the two subarrays from the entire array.

$$\mathbf{J}_1 = \overbrace{\begin{bmatrix} 1 & 0 & 0 & \cdots & 0 & 0 \\ 0 & 1 & 0 & \cdots & 0 & 0 \\ 0 & 0 & 1 & \cdots & 0 & 0 \\ \vdots & \vdots & \vdots & \ddots & \vdots & \vdots \\ 0 & 0 & 0 & \cdots & 1 & 0 \end{bmatrix}}^{N \text{ columns}}, \quad \mathbf{J}_2 = \overbrace{\begin{bmatrix} 0 & 1 & \cdots & 0 & 0 & 0 \\ \vdots & \vdots & \ddots & \vdots & \vdots & \vdots \\ 0 & 0 & \cdots & 1 & 0 & 0 \\ 0 & 0 & \cdots & 0 & 1 & 0 \\ 0 & 0 & \cdots & 0 & 0 & 1 \end{bmatrix}}^{N \text{ columns}} \Bigg\} N\text{-1 rows} \tag{16}$$

In other words, $\mathbf{J}_1\mathbf{A} \in \mathcal{C}_{(N-1)\times L}$ is the steering matrix of the first $(N-1)$ sensors, while $\mathbf{J}_2\mathbf{A} \in \mathcal{C}_{(N-1)\times L}$ is the steering matrix of the last $(N-1)$ sensors. Since Subarray 2 is a constant shift of the identical Subarray 1, their steering matrices are related by a rotational operator $\mathbf{\Omega}$, i.e.

$$\left(\mathbf{J}_1\mathbf{A}\right)\mathbf{\Omega} = \mathbf{J}_2\mathbf{A}, \quad \text{where } \mathbf{\Omega} = \text{diag}\left\{e^{ju_1}, \cdots, e^{ju_L}\right\}. \tag{17}$$

Accordingly, the signals on these two subarrays are

$$\begin{cases} \mathbf{Y}_1 = \mathbf{J}_1\mathbf{A}\boldsymbol{s} + \mathbf{n}_1 = \mathbf{A}_1\boldsymbol{s} + \mathbf{n}_1 \\ \mathbf{Y}_2 = \mathbf{J}_2\mathbf{A}\boldsymbol{s} + \mathbf{n}_2 = \mathbf{A}_1\boldsymbol{\Omega}\boldsymbol{s} + \mathbf{n}_2 \end{cases}. \tag{18}$$

Define $\mathbf{Z} = \begin{bmatrix} \mathbf{Y}_1 \\ \mathbf{Y}_2 \end{bmatrix}$, $\mathbf{A}_\mathbf{Z} = \begin{bmatrix} \mathbf{A}_1 \\ \mathbf{A}_1\boldsymbol{\Omega} \end{bmatrix}$, and $\mathbf{n}_\mathbf{Z} = \begin{bmatrix} \mathbf{n}_1 \\ \mathbf{n}_2 \end{bmatrix}$, (18) can be represented in a simple matrix form, which is

$$\mathbf{Z} = \mathbf{A}_\mathbf{Z}\mathbf{s} + \mathbf{n}_\mathbf{Z}. \tag{19}$$

Using (10), the parameter estimates $\{\theta_m | m = 1, \cdots, L\}$ can be deduced from the arguments $\{u_m | m = 1, \cdots, L\}$, of the diagonal elements of the rotational operator $\boldsymbol{\Omega}$. The arguments $\{u_m | m = 1, \cdots, L\}$, in turn, can be deduced from the eigenvalues of $\boldsymbol{\Omega}$. Consequently, the DOA parameter can be derived once the eigenvalues of $\boldsymbol{\Omega}$ are obtained, thus avoiding the search of the peaks in the spectral-based estimation methods. Next, we show the procedure of deducing the eigenvalues of $\boldsymbol{\Omega}$.

In a noiseless environment, the range of $\mathbf{A}, \Re\{\mathbf{A}\}$, is equal to the range of $\mathbf{E}_s$, $\Re\{\mathbf{E}_s\}$. In this situation, there exist a unique and nonsingular transform matrix $\mathbf{T}$, such that

$$\mathbf{E}_s = \mathbf{A}\mathbf{T}. \tag{20}$$

Therefore, we obtain that

$$\mathbf{A}_\mathbf{Z}\mathbf{T} = \begin{bmatrix} \mathbf{A}_1\mathbf{T} \\ \mathbf{A}_1\boldsymbol{\Omega}\mathbf{T} \end{bmatrix} = \begin{bmatrix} \mathbf{E}_{\mathbf{S1}} \\ \mathbf{E}_{\mathbf{S2}} \end{bmatrix} = \begin{bmatrix} \mathbf{E}_{\mathbf{S1}} \\ \mathbf{E}_{\mathbf{S1}}\boldsymbol{\Psi} \end{bmatrix}, \tag{21}$$

where

$$\boldsymbol{\Psi} = \mathbf{T}^{-1}\boldsymbol{\Phi}\mathbf{T} \tag{22}$$

is the transformed rotational matrix of the signals, and $\mathbf{E_{S1}}$ and $\mathbf{E_{S2}} \in \mathcal{C}_{(N-1)\times L}$ are the signal eigenvectors of two subarrays. However, in a practical environment, $\Re\{\mathbf{E}_s\} \neq \Re\{\mathbf{A}\}$ and $\Re\{\mathbf{E_{S1}}\} \neq \Re\{\mathbf{E_{S2}}\}$ with probability one. The matrix $\boldsymbol{\Psi}$ can be obtained by solving the equation $\mathbf{E_{S2}} = \mathbf{E_{S1}}\boldsymbol{\Psi}$ based on least squares (LS) criterion, i.e.

$$\boldsymbol{\Psi} = \left(\mathbf{E}_{\mathbf{S1}}^{\dagger}\mathbf{E}_{\mathbf{S1}}\right)^{-1}\mathbf{E}_{\mathbf{S1}}^{\dagger}\mathbf{E}_{\mathbf{S2}}. \tag{23}$$

According to (22), the diagonal elements of $\boldsymbol{\Omega}$ are the eigenvalues of $\boldsymbol{\Psi}$. The parameters $\{\theta_m | m = 1, \cdots, L\}$ can then be estimated using (10), i.e.

$$\hat{\theta}_i = \cos^{-1}\left(\frac{\arg(\varsigma_i)\lambda}{2\pi d_x}\right), \quad i = 1, \cdots, L, \tag{24}$$

where ς_i is the i^{th} eigenvalue of $\boldsymbol{\Psi}$.

Another approach to obtain $\boldsymbol{\Psi}$ based on the total least squares (TLS) criterion, which provides better accuracy than LS criterion, was provided in [13]. Defining $\mathbf{E}_c = \left[\mathbf{E_{S1}} \middle| \mathbf{E_{S2}}\right]$, there exists $\mathbf{F} = \begin{bmatrix}\mathbf{F}_1 \\ \hline \mathbf{F}_2\end{bmatrix}$, such that $\mathbf{EF} = \mathbf{0}$. Given $\boldsymbol{\Psi} = -\mathbf{F}_1\mathbf{F}_2^{-1}$, the steps of the solution based on TLS criterion are summarized below.

Step 1. Calculate the eigen-decomposition of $\mathbf{E}_c$

$$\mathbf{E}_c^{\dagger}\mathbf{E}_c = \mathbf{U}\boldsymbol{\Lambda}\mathbf{U}^{\dagger}. \tag{25}$$

Step 2. Partition $\mathbf{U}$ into four $L \times L$ matrices

$$\mathbf{U} = \left[\begin{array}{c|c}\mathbf{U}_{11} & \mathbf{U}_{12} \\ \hline \mathbf{U}_{21} & \mathbf{U}_{22}\end{array}\right]. \tag{26}$$

Step 3. Compute the eigenvalues $\{\varsigma_i | i = 1, \cdots, L\}$ of $\boldsymbol{\Psi} = -\mathbf{U}_{12}\mathbf{U}_{22}^{-1}$.

Step 4. Calculate the DOA estimates

$$\hat{\theta}_i = \cos^{-1}\left(\frac{\arg(\varsigma_i)\lambda}{2\pi d_x}\right), \quad i = 1,\cdots,L. \tag{27}$$

Although we have taken angle estimation as an example to introduce the ESPRIT algorithm, this method can be generalized to estimate many other parameters such as delay and Doppler frequency, by changing the content of the steering matrix. For instance, the steering matrix in delay estimation is

$$\mathbf{A}_\tau = [\mathbf{a}(\tau_1) \quad \mathbf{a}(\tau_2) \quad \mathbf{a}(\tau_3) \quad \cdots \quad \mathbf{a}(\tau_L)], \tag{28}$$

where

$$\mathbf{a}(\tau_m) = [1 \quad e^{-j2\pi\Delta f\tau_m} \quad \cdots \quad e^{-j2\pi(N-1)\Delta f\tau_m}]^T, \tag{29}$$

and Δf is the separation between frequency samples, and $\{\tau_m | m = 1,\cdots,L\}$ are the delays of L sources.

2.2.2 Unitary ESPRIT Algorithm

The unitary ESPRIT algorithm, which is a variant of ESPRIT algorithm, possesses better estimation accuracy with reduced computational cost by exploiting the unitary property of the rotational operator [47]. Because the forward-backward smoothing is implicitly incorporated in the algorithm, unitary ESPRIT is capable of resolving two coherent sources. The computational cost is dramatically reduced because the complex computations in ESPRIT, including the eigen-decompositions, are replaced by the real-valued computations after the initial transformation. Detailed deduction of unitary ESPRIT algorithm was provided in [47,48]. Next, we summarize their work without showing rigorous proofs.

The expression of the steering vector **a** of the ULA in (10) uses the leftmost element of the array as the phase reference. However, if the center of the ULA is employed as the phase reference instead, the steering vector becomes centrosymmetric. The rearranged steering vectors of the ULA with odd- and even-numbered elements are

$$\begin{aligned} &\text{odd}: \mathbf{a}(\theta) = [e^{-i(\frac{N-1}{2})u}, \quad \cdots \quad e^{-iu}, \quad 1, \quad e^{iu}, \quad \cdots \quad e^{i(\frac{N-1}{2})u}]^T \\ &\text{even}: \mathbf{a}(\theta) = [e^{-i(\frac{N+1}{2})u}, \quad \cdots \quad e^{-i(\frac{1}{2})u}, \quad e^{i(\frac{1}{2})u}, \quad \cdots \quad e^{i(\frac{N+1}{2})u}]^T \end{aligned} . \tag{30}$$

The steering vector is conjugate centrosymmetric when $\mathbf{\Pi}_N \mathbf{a} = \mathbf{a}^\dagger$ holds, where $\mathbf{\Pi}_N$ is the exchange matrix as shown below:

$$\mathbf{\Pi}_N = \begin{bmatrix} 0 & & 1 \\ & \iddots & \\ 1 & & 0 \end{bmatrix} \in \mathcal{R}_{N\times N} . \tag{31}$$

Using the property that inner product of any two conjugate centrosymmetric vectors is real-valued, the complex-valued steering matrix **A** whose columns are conjugate centrosymmetric can be changed into a real-valued matrix by proper transformation. The most widely used matrices that achieve this purpose are [53]

$$\mathbf{Q}_{2n} = \frac{1}{\sqrt{2}} \begin{bmatrix} \mathbf{I}_n & j\mathbf{I}_n \\ \mathbf{\Pi}_n & -j\mathbf{\Pi}_n \end{bmatrix} \text{ when } N = 2n \text{ is even} \tag{32}$$

$$\mathbf{Q}_{2n+1} = \frac{1}{\sqrt{2}} \begin{bmatrix} \mathbf{I}_n & \mathbf{0} & j\mathbf{I}_n \\ \mathbf{0}^T & \sqrt{2} & \mathbf{0}^T \\ \mathbf{\Pi}_n & \mathbf{0} & -j\mathbf{\Pi}_n \end{bmatrix} \text{ when } N = 2n+1 \text{ is odd} . \tag{33}$$

For instance, when *N* is odd, the modified steering vector

$$\begin{aligned} \mathbf{d}(\theta) &= \mathbf{Q}_{N_R}^\dagger \mathbf{a}(\theta) \\ &= \sqrt{2}\left[\cos\left(\frac{N-1}{2}u\right), \cdots, \cos(u), \frac{1}{\sqrt{2}}, -\sin\left(\frac{N-1}{2}u\right), \cdots, -\sin(u) \right] \end{aligned} \tag{34}$$

is real-valued.

Starting from (18), the deductions are as follows.

$$\begin{aligned} & e^{iu}\mathbf{J}_1\mathbf{a} = \mathbf{J}_2\mathbf{a} \\ & \Rightarrow e^{iu}\mathbf{Q}_{N-1}^{\dagger}\mathbf{J}_1\mathbf{Q}_N\mathbf{Q}_N^{\dagger}\mathbf{a} = \mathbf{Q}_{N-1}^{\dagger}\mathbf{J}_2\mathbf{Q}_N\mathbf{Q}_N^{\dagger}\mathbf{a}\,. \\ & \Rightarrow e^{iu}\mathbf{Q}_{N-1}^{\dagger}\mathbf{J}_1\mathbf{Q}_N\mathbf{d} = \mathbf{Q}_{N-1}^{\dagger}\mathbf{J}_2\mathbf{Q}_N\mathbf{d} \end{aligned} \tag{35}$$

Define $\mathbf{K}_1$ and $\mathbf{K}_2$ in (36), (35) can be further simplified to a real-valued equation (37).

$$\begin{aligned} \mathbf{K}_1 &= \mathrm{Re}\left\{\mathbf{Q}_{N-1}^{\dagger}\mathbf{J}_2\mathbf{Q}_N\right\} \\ \mathbf{K}_2 &= \mathrm{Im}\left\{\mathbf{Q}_{N-1}^{\dagger}\mathbf{J}_2\mathbf{Q}_N\right\} \end{aligned} \tag{36}$$

$$\begin{aligned} & \Rightarrow e^{i\frac{u}{2}}\left(\mathbf{K}_1 - i\mathbf{K}_2\right)\mathbf{d} = e^{-i\frac{u}{2}}\left(\mathbf{K}_1 + i\mathbf{K}_2\right)\mathbf{d} \\ & \Rightarrow (e^{i\frac{u}{2}} - e^{-i\frac{u}{2}})\mathbf{K}_1\mathbf{d} = i(e^{i\frac{u}{2}} + e^{-i\frac{u}{2}})\mathbf{K}_2\mathbf{d} \quad . \\ & \Rightarrow \tan\left(\frac{u}{2}\right)\mathbf{K}_1\mathbf{d} = \mathbf{K}_2\mathbf{d} \end{aligned} \tag{37}$$

Assuming $\mathbf{D} = \left[\mathbf{d}_1 \middle| \mathbf{d}_2 \middle| \mathbf{d}_3 \middle| \cdots \mathbf{d}_N\right]$, we can get the critical equation

$$\left(\mathbf{K}_1\mathbf{D}\right)\boldsymbol{\Omega} = \mathbf{K}_2\mathbf{D}, \tag{38}$$

which corresponds to (17) in preceding ESPRIT algorithm. Similarly, the estimates of unitary ESPRIT method can be acquired by solving (39) based on TLS criterion:

$$\left(\mathbf{K}_1\mathbf{E}_s\right)\boldsymbol{\Psi} = \mathbf{K}_2\mathbf{E}_s\,. \tag{39}$$

The variables and important equations of ESPRIT and their corresponding ones in unitary ESPRIT are listed below to help clarify the concepts.

ESPRIT		Unitary ESPRIT
$\mathbf{a}$	$\Leftrightarrow$	$\mathbf{d}$
$\mathbf{A}$	$\Leftrightarrow$	$\mathbf{D}$
$\mathbf{\Omega} = \mathrm{diag}\left\{e^{ju_1}, \cdots, e^{ju_L}\right\}$	$\Leftrightarrow$	$\mathbf{\Omega} = \mathrm{diag}\left\{\tan\left(\frac{u_1}{2}\right), \cdots, \tan\left(\frac{u_L}{2}\right)\right\}$
$\left(\mathbf{J}_1\mathbf{A}\right)\mathbf{\Omega} = \mathbf{J}_2\mathbf{A}$	$\Leftrightarrow$	$\left(\mathbf{K}_1\mathbf{D}\right)\mathbf{\Omega} = \mathbf{K}_2\mathbf{D}$
$\mathbf{E}_s = \mathbf{A}\mathbf{T}$	$\Leftrightarrow$	$\mathbf{E}_s = \mathbf{D}\mathbf{T}$
$\left(\mathbf{J}_1\mathbf{E}_s\right)\mathbf{\Psi} = \mathbf{J}_2\mathbf{E}_s$	$\Leftrightarrow$	$\left(\mathbf{K}_1\mathbf{E}_s\right)\mathbf{\Psi} = \mathbf{K}_2\mathbf{E}_s$
$\mathbf{\Psi} = \mathbf{T}^{-1}\mathbf{\Omega}\mathbf{T}$	$\Leftrightarrow$	$\mathbf{\Psi} = \mathbf{T}^{-1}\mathbf{\Omega}\mathbf{T}$

(40)

The computational complexity is reduced because the eigen-decomposition is performed over a real-valued matrix. Simulation results in [47] also show that the unitary ESPRIT algorithm outperforms the original ESPRIT algorithm.

2.2.3 Multi-Dimensional ESPRIT Algorithm

In previous two subsections, the ESPRIT and unitary ESPRIT algorithm were described in the context of single-parameter estimation. When multiple parameters are involved in the estimation, the steering matrix is a function of multiple parameters, and multiple estimates must be obtained simultaneously. Although the ESPRIT algorithm is computationally efficient, the extension to multi-dimensional estimation is, unfortunately, not so straightforward. The primary problem comes from the pairing of multiple parameters. The closed-form of 2-D unitary ESPRIT algorithm with uniform rectangular array (URA) was proposed in [48] to solve the pairing problem for two-parameter estimation. With the extension to two dimensions, the array can estimate azimuth angle with no ambiguity, and elevation angle with ambiguity. Detailed procedure for closed-

form 2D unitary ESPRIT algorithm was described by the authors in [48]. Next, we summarize their work without providing rigorous mathematical proof.

Two operators, $vec(\bullet)$ and $mat(\bullet)$, are extensively used in the deduction of this algorithm. The operator $vec(\mathbf{A})$ stacks the columns of an $N \times M$ matrix $\mathbf{A}$ to form an $NM \times 1$ vector. The operator $mat(\mathbf{a})$, an inverse function of $vec(\mathbf{A})$, maps the $NM \times 1$ vector back to the original $N \times M$ matrix $\mathbf{A}$. An important property of the operator $vec(\bullet)$ is

$$vec(\mathbf{ABC}) = \left(\mathbf{C}^T \otimes \mathbf{A}\right) vec(\mathbf{B}), \tag{41}$$

where $\otimes$ denotes the Kronecker product.

Assuming the antenna spacings on x and y directions are d_x and d_y, respectively, the steering matrix of a 2-D URA with array size $n_x \times n_y$ is

$$\mathbf{A} = [\mathbf{a}(\theta_1,\phi_1) \quad \mathbf{a}(\theta_2,\phi_2) \quad \mathbf{a}(\theta_3,\phi_3) \quad \cdots \quad \mathbf{a}(\theta_L,\phi_L)], \tag{42}$$

where

$$\mathbf{a}(\theta,\phi) = [1 \quad e^{iu} \quad e^{i2u} \quad \cdots \quad e^{i((n_x-1)u+(n_y-1)v)}]^T, \text{ where } \begin{cases} u = \dfrac{2\pi d_x}{\lambda}\cos\phi\cos\theta \\ v = \dfrac{2\pi d_y}{\lambda}\cos\phi\sin\theta \end{cases}. \tag{43}$$

Using the operator $mat(\bullet)$, the steering vector $\mathbf{a}(\theta,\phi)$ of the URA in (43) can be represented as the product of two vectors $\mathbf{a}_x(u)$ and $\mathbf{a}_y(v)$, as shown below.

$$
\begin{aligned}
mat(\mathbf{a}(\theta,\phi)) &= \begin{bmatrix} 1 & e^{iv} & \cdots & e^{i(n_y-1)v} \\ e^{iu} & e^{i(u+v)} & \cdots & e^{i(u+(n_y-1)v)} \\ \vdots & \vdots & \vdots & \vdots \\ e^{i(n_x-1)u} & e^{i((n_x-1)u+v)} & \cdots & e^{i((n_x-1)u+(n_y-1)v)} \end{bmatrix} \\
&= \begin{bmatrix} 1 \\ e^{iu} \\ \vdots \\ e^{i(n_x-1)u} \end{bmatrix} \begin{bmatrix} 1 & e^{iv} & \cdots & e^{i(n_y-1)v} \end{bmatrix} \\
&= \mathbf{a}_x(u)\mathbf{a}_y^T(v).
\end{aligned} \tag{44}
$$

Through a similar process in the unitary ESPRIT algorithm, $\mathbf{a}_x(u)\mathbf{a}_y^T(v)$ can be transformed into a real-valued form by

$$
\begin{aligned}
&\mathbf{Q}_{n_x}^{\dagger}\mathbf{a}_x(u)\mathbf{a}_y^T(v)\mathbf{Q}_{n_y}^{*} \\
&= \mathbf{d}_x(u)\mathbf{d}_y^T(v) \\
&= \mathbf{D}(u,v).
\end{aligned} \tag{45}
$$

Then, we may choose the subarrays at x and y directions from the URA such that the second subarray is a constant displacement of the first subarray, as illustrated in Figure 5.

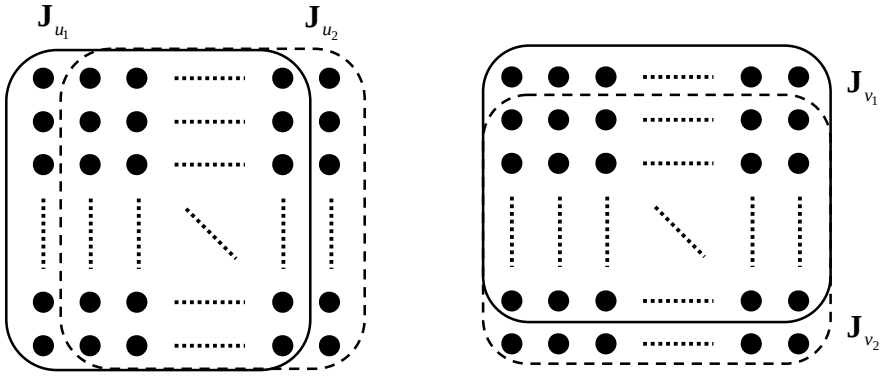

Figure 5: Selection of 2D subarrays. (a) Subarrays for parameter *u* (b) Subarrays for parameter *v*.

Following the same deduction from (35) to (37) in unitary ESPRIT method, we obtain

$$\tan\left\{\frac{u}{2}\right\}\mathbf{K}_1\mathbf{D}(u,v)=\mathbf{K}_2\mathbf{D}(u,v),\ \text{ where }\begin{cases}\mathbf{K}_1=\mathrm{Re}\left\{\mathbf{Q}_{n_x-1}^{\dagger}\mathbf{J}_2\mathbf{Q}_{n_x}\right\}\\ \mathbf{K}_2=\mathrm{Im}\left\{\mathbf{Q}_{n_x-1}^{\dagger}\mathbf{J}_2\mathbf{Q}_{n_x}\right\}\end{cases} \tag{46}$$

$$\tan\left\{\frac{v}{2}\right\}\mathbf{D}(u,v)\mathbf{K}_3^T=\mathbf{D}(u,v)\mathbf{K}_4^T,\ \text{where}\begin{cases}\mathbf{K}_3=\mathrm{Re}\left\{\mathbf{Q}_{n_y-1}^{\dagger}\mathbf{J}_2\mathbf{Q}_{n_y}\right\}\\ \mathbf{K}_4=\mathrm{Im}\left\{\mathbf{Q}_{n_y-1}^{\dagger}\mathbf{J}_2\mathbf{Q}_{n_y}\right\}\end{cases}. \tag{47}$$

Using the property of *vec*(•) described in (41), $\mathbf{D}(u,v)$ in (46) and (47) can be changed to a $n_x n_y \times 1$ vector $\mathbf{d}(u,v)$, and (46) and (47) can be modified into

$$\tan\left\{\frac{u}{2}\right\}\mathbf{K}_{u_1}\mathbf{d}(u,v)=\mathbf{K}_{u_2}\mathbf{d}(u,v),\ \text{ where }\begin{cases}\mathbf{K}_{u_1}=\mathbf{I}_{n_x}\otimes\mathbf{K}_1\\ \mathbf{K}_{u_2}=\mathbf{I}_{n_x}\otimes\mathbf{K}_2\end{cases} \tag{48}$$

$$\tan\left\{\frac{v}{2}\right\}\mathbf{K}_{v_1}\mathbf{d}(u,v)=\mathbf{K}_{v_2}\mathbf{d}(u,v),\ \text{ where }\begin{cases}\mathbf{K}_{v_1}=\mathbf{K}_3\otimes\mathbf{I}_{n_y}\\ \mathbf{K}_{v_2}=\mathbf{K}_4\otimes\mathbf{I}_{n_y}\end{cases}. \tag{49}$$

Previous deduction only include single steering vector for some specific angle (θ,ϕ). Considering all L signal sources, we define

$$\mathbf{D}=\left[\mathbf{d}(u_1,v_1)\middle|\mathbf{d}(u_2,v_2)\middle|\cdots\mathbf{d}(u_L,v_L)\right]. \tag{50}$$

In accordance, we obtain the form of the standard ESPRIT algorithm.

$$(\mathbf{K}_{u_1}\mathbf{D})\mathbf{\Omega}_u=\mathbf{K}_{u_2}\mathbf{D}\quad\text{,where }\mathbf{\Omega}_u=\mathrm{diag}\left\{\tan\left(\frac{u_1}{2}\right),\cdots,\tan\left(\frac{u_L}{2}\right)\right\} \tag{51}$$

$$(\mathbf{K}_{v_1}\mathbf{D})\mathbf{\Omega}_v=\mathbf{K}_{v_2}\mathbf{D}\quad\text{,where }\ \mathbf{\Omega}_u=\mathrm{diag}\left\{\tan\left(\frac{v_1}{2}\right),\cdots,\tan\left(\frac{v_L}{2}\right)\right\}. \tag{52}$$

Using the same procedure in ESPRIT algorithm, the equations can be solved by the TLS criterion:

$$\left(\mathbf{K}_{u_1}\mathbf{E}_s\right)\boldsymbol{\Psi}_u = \mathbf{K}_{u_2}\mathbf{E}_s, \text{ where } \boldsymbol{\Psi}_u = \mathbf{T}^{-1}\boldsymbol{\Omega}_u\mathbf{T} \tag{53}$$

$$\left(\mathbf{K}_{v_1}\mathbf{E}_s\right)\boldsymbol{\Psi}_v = \mathbf{K}_{v_2}\mathbf{E}_s, \text{ where } \boldsymbol{\Psi}_v = \mathbf{T}^{-1}\boldsymbol{\Omega}_v\mathbf{T}. \tag{54}$$

However, after $\boldsymbol{\Psi}_u$ and $\boldsymbol{\Psi}_v$ are solved based on TLS criterion, if the eigen-decompositions of $\boldsymbol{\Psi}_u$ and $\boldsymbol{\Psi}_v$ are used to acquire $\{u_m | m = 1, \cdots, L\}$ and $\{v_m | m = 1, \cdots, L\}$ separately, the pairing of u_m and v_m is difficult. This pairing problem can be easily resolved when unitary ESPRIT is employed because the matrices $\boldsymbol{\Psi}_u$, $\boldsymbol{\Psi}_v$, $\boldsymbol{\Omega}_u$, and $\boldsymbol{\Omega}_v$ are real-valued. The solution combines two real-valued eigen-decompositions into one complex-valued eigen-decomposition. Since $\boldsymbol{\Psi}_u$ and $\boldsymbol{\Psi}_v$ have common eigenvectors $\mathbf{T}$, these two real-valued eigen-decompositions can be combined to be a complex-valued eigen-decomposition. Consequently, u_m and v_m are automatically paired through the complex eigen-decomposition

$$\boldsymbol{\Psi}_u + i\boldsymbol{\Psi}_v = \mathbf{T}^{-1}(\boldsymbol{\Omega}_u + i\boldsymbol{\Omega}_v)\mathbf{T}. \tag{55}$$

Notice that the matrix size of $\mathbf{K}_{u_1}$ and $\mathbf{K}_{u_2}$ is $n_x(n_y - 1) \times n_x n_y$, and the matrix size of $\mathbf{K}_{v_1}$ and $\mathbf{K}_{v_2}$ is $n_y(n_x - 1) \times n_x n_y$. Therefore, the maximum number of sources that URA-ESPRIT can handle is $\min\{n_x(n_y - 1), n_y(n_x - 1)\}$.

Next we describe the extension of two-dimensional to multi-dimensional estimation. Using 3-D antenna array and multi-dimensional ESPRIT algorithm, both azimuth and elevation angles can be estimated without ambiguity. Assume the number of elements on *x*, *y*, and *z* directions are n_x, n_y, and n_z, respectively, and the antenna spacings on *x*, *y*, and *z* directions are d_x, d_y, and d_z, respectively. The steering matrix of the 3-D rectangular array is

$$\mathbf{A} = [\mathbf{a}(\theta_1,\phi_1) \quad \mathbf{a}(\theta_2,\phi_2) \quad \mathbf{a}(\theta_3,\phi_3) \quad \cdots \quad \mathbf{a}(\theta_L,\phi_L)], \tag{56}$$

where

$$\mathbf{a}(\theta,\phi) = [1 \quad e^{iu} \quad e^{i2u} \quad \cdots \quad e^{i((n_x-1)u+(n_y-1)v+(n_z-1)w)}]^T, \text{ where } \begin{cases} u = \dfrac{2\pi d_x}{\lambda}\cos\phi\cos\theta \\ v = \dfrac{2\pi d_y}{\lambda}\cos\phi\sin\theta \\ w = \dfrac{2\pi d_z}{\lambda}\sin\phi \end{cases}. \tag{57}$$

The aforementioned 2-D URA-ESPRIT comprises two applications of unitary ESPRIT algorithm, one for the estimate of *u* on the x-axis, the other for *v* on the y-axis. The parameters *u* and *v* are automatically paired by deriving *u*+*iv* from a complex eigen-decomposition. The procedure of multi-dimensional ESPRIT, which involves multiple times of unitary ESPRIT algorithm, is similar to 2-D URA-ESPRIT except the final solution to the pairing problem; therefore, we omit the mathematical deduction and only show the final critical linear equations that must be solved based on the LS or TLS criterion. Assuming the number of dimensions is *M*, these *M* critical equations are

$$\begin{aligned} &\left(\mathbf{K}_{m_1}\mathbf{E}_s\right)\boldsymbol{\Psi}_u = \mathbf{K}_{m_2}\mathbf{E}_s, \\ &\text{where } \boldsymbol{\Psi}_m = \mathbf{T}^{-1}\boldsymbol{\Omega}_m\mathbf{T}, \qquad m=1,\cdots,M. \end{aligned} \tag{58}$$

When the number of dimensions is more than two, the pairing problem cannot be solved by the complex eigen-decomposition, which allows at most two real-valued parameters. In a noiseless condition, the *M* transformed rotational matrices $\{\boldsymbol{\Psi}_m, m=1,\cdots,M\}$ share the same eigenvectors. However, when the noise is present, their eigenvectors are not equal with probability one. The pairing problem in multi-dimensional ESPRIT algorithm is solved by a linear algebra method called the simultaneous Schur decomposition (SSD) [49]. With SSD, the eigenvalues of multiple

matrices can be jointly estimated under the criterion of minimizing the strictly lower triangular part of the matrices during the upper-triangularization procedure, hence achieving automatic pairing of all parameters. Accordingly, ESPRIT can be extended to theoretically infinite-dimensional parameter estimation.

2.2.4 Various MIMO Parameter Estimation Schemes Based on the ESPRIT Algorithm

Some research groups have employed the ESPRIT algorithm to estimate the MIMO path parameters from the measured data. The authors of [14] estimated sequentially the delays, DOAs and DODs using unitary ESPRIT, while the joint estimation of these parameters is explored in [16]. These two estimation schemes are discussed below and their performances will be compared in Chapter 5.

The path parameters of MIMO channels include the complex gain, delay, Doppler shift, DOA, and DOD. Because of the requirement of channel stability for our measurement system, the Doppler shift is not considered in this dissertation. The frequency response for each pair of antennas is

$$h(f, \mathbf{x}_R, \mathbf{x}_T) = \sum_{k=1}^{L} \alpha_k e^{-j2\pi f \tau_k} e^{j\mathbf{k}_{R_k} \cdot \mathbf{x}_R} e^{j\mathbf{k}_{T_k} \cdot \mathbf{x}_T}, \tag{59}$$

where $\mathbf{x}_R$ and $\mathbf{x}_T$ are the coordinates of the receive and transmit antennas, respectively, and $\mathbf{k}_{R_k}$ and $\mathbf{k}_{T_k}$ are the functions of the DOA and DOD of the k^{th} path. If the channel matrix of the 3D cubicle array is stacked column-by-column into a vector form, the channel frequency response can be represented as

$$\boldsymbol{h} = \mathbf{A}\mathbf{s}, \tag{60}$$

where the signal source is $\mathbf{s}=[\alpha_1 \ \alpha_2 \ \alpha_3 \ \ldots \ \alpha_L]^T$, the steering matrix $\mathbf{A}=[\mathbf{a}_1 \,|\, \mathbf{a}_2 \,|\cdots|\, \mathbf{a}_L]$, and the steering vector of the i^{th} path is

$$\mathbf{a}_i = \mathbf{a}_{T_i} \otimes \mathbf{a}_{R_i} \otimes \mathbf{a}_{\tau_i} . \tag{61}$$

The delay steering vector $\mathbf{a}_{\tau_i}$ has been shown in (29), while $\mathbf{a}_{T_i}$ and $\mathbf{a}_{R_i}$, the steering vectors of i^{th} DOD and DOA, are in the form of (56). Equations (60) and (61) will be used to reconstruct the MIMO channel frequency response of various array geometry in Chapters 4 and 5 according to the estimated parameters. These parameters can be estimated sequentially or jointly. Joint estimation needs higher computational complexity because larger array is involved, but it also provides better accuracy by avoiding the accumulated error that occurs in sequential estimation. Next, we describe these two estimation schemes.

Sequential estimation scheme [14]: Given the number of frequency samples N_f, the number of receive antennas N_R, and the number of transmit antennas N_T, the frequency response $\boldsymbol{h}(f,\mathbf{x}_R,\mathbf{x}_T)$ can be represented as an $(N_f \times N_R \times N_T)$ three-dimensional matrix, which can further be rearranged to a $(N_f \times N_R N_T)$ matrix $\boldsymbol{h}_f$. Since $\boldsymbol{h}_f$ comprises $N_R N_T$ snapshots of an N_f−element frequency array, and it satisfies the rotational invariance property, the ESPRIT algorithm can be applied to estimate the delay. Having obtained the delay estimates, the delay steering matrix $\mathbf{A}_\tau$ in (28) can then be used to recover the spatial array signal $\boldsymbol{h}_{RT}$, using

$$\boldsymbol{h}_{RT} = (\mathbf{A}_\tau^\dagger \mathbf{A}_\tau)^{-1} \mathbf{A}_\tau^\dagger \boldsymbol{h}_f . \tag{62}$$

The m^{th} row of $\boldsymbol{h}_{RT}$, denoted as $\boldsymbol{h}_{RT}^m$, is the spatial array signal contributed from the multipaths with delay τ_m. As a consequence, $\boldsymbol{h}_{RT}^m$, which is an $N_R N_T$-element vector, can

be rearranged to a ($N_R \times N_T$) matrix. After the rearrangement, $\boldsymbol{h}_{RT}^{m}$ becomes an N_R-element array with N_T snapshots, and the ESPRIT algorithm can then be applied to estimate the DOA along with its steering matrix $\mathbf{A}_{R,m}$. Subsequently, the transmit array signal $\boldsymbol{h}_T$ contributed from the multipath with delay τ_m can be recovered by

$$\boldsymbol{h}_{T,m} = \left(\mathbf{A}_{R,m}^{\dagger}\mathbf{A}_{R,m}\right)^{-1}\mathbf{A}_{R,m}^{\dagger}\boldsymbol{h}_{RT}^{m}. \tag{63}$$

Likewise, the n^{th} row of $\boldsymbol{h}_{T,m}$ is the transmit array signal contributed from the multipaths with delay τ_m and DOA $\left(\theta_{R_n},\phi_{R_n}\right)$. The DOD estimation corresponding to the specific delay and DOA can then be performed with ESPRIT. Smoothing in each array dimension using overlapping subarrays is done prior to each application of ESPRIT.

Joint estimation scheme [16]: If the signal $\boldsymbol{h}(f,x_R,x_T)$ is re-organized into a single vector $\boldsymbol{h}_{fRT}$ of size $N_f N_R N_T$, the signal can be represented in the form of (60) and (61). The snapshots are obtained by using the overlapping frequency subarrays and spatial subarrays. It is straightforward to apply the multi-dimensional ESPRIT to jointly estimate all parameters simultaneously.

One severe problem with the joint estimation is the huge correlation matrix size caused by multiple dimensions. For instance, if both the transmit and the receive antenna array sizes are (3×2×2) and the number of frequency samples is 200, the correlation matrix size is as large as 28800, which is intractable with our computer. Sequential estimation, on the other hand, suffers accumulated errors because each separate estimation is based on the results of previous estimation results. An alternative solution is to use the hybrid estimation, in which some parts of the parameters are estimated sequentially and the other parts are estimated jointly.

Equations (59) to (61) will be used to reconstruct the channel frequency response according to the estimated parameters. In these equations, the propagation waves are assumed to be plane waves for the convenience of analysis, as shown in Figure 6(a). Based on the plane wave model, the DOAs (or DODs) of each path are the same for all receive (or transmit) antennas. It is a claim of this thesis that the plane wave model causes capacity underestimation when the LOS is present and the distance of the communication link is short. In this case, a more accurate spherical wave model, as shown in Figure 6(b), should be employed for the LOS component. In Chapter 5, the spherical wave model will be used in the channel construction for the LOS component when it is available. The capacity underestimation phenomenon caused by improper plane wave model will be discussed in detail in Chapter 6.

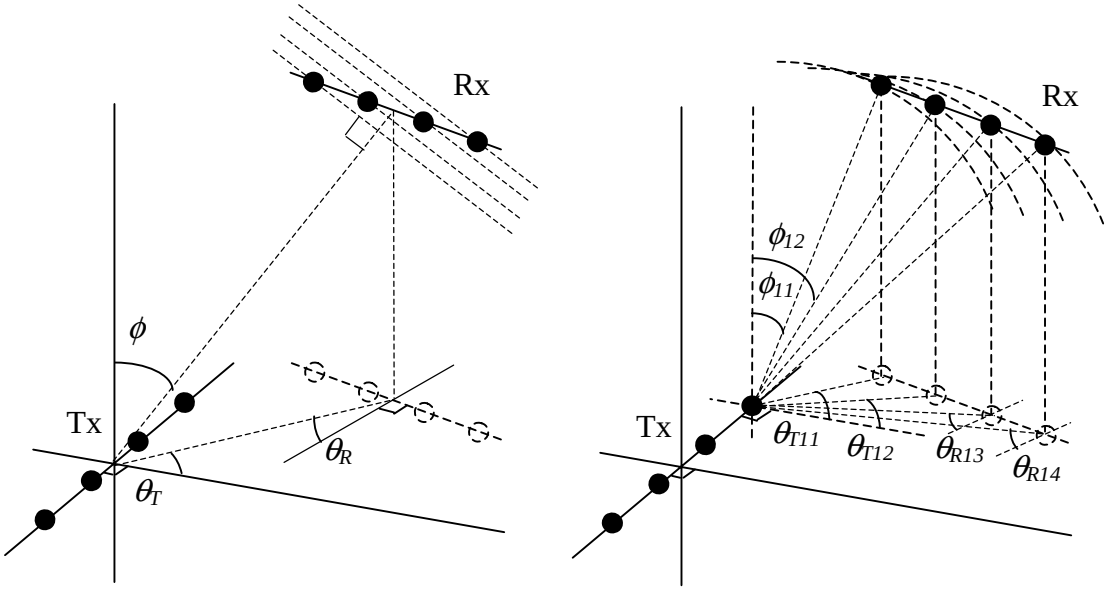

(a) Plane wave model (b) Spherical wave model

Figure 6: Illustration of (a) the plane wave model and (b) the spherical wave model. Tx and Rx arrays are assumed to be parallel with the horizontal (x-y) plane. In the plane wave model, the DOAs are the same for all elements in Rx, while in spherical wave model, the DOA of each element in Rx is different from the others.

2.2.5 Spatial Smoothing Technique

In previous discussion about the estimation algorithms, we assume the signal sources are uncorrelated. However, in some applications such as multipath channel parameter estimation, the paths originate from the same signal source and accordingly their signals are partially or fully correlated. In this situation, the rank of the correlation matrix of the signal, $\mathbf{R}_{ss}$, is less than the number of the paths. To be specific, if m out of L signal sources are coherent, the rank of the correlation matrix is equal to $L-m+1$. The spatial smoothing technique, which was proposed by Evans et al. [54] and further investigated by Shan [55,56], can decorrelate the signal sources by averaging the correlation matrix of identical subarrays. As shown in Figure 7, $(N-n+1)$ overlapping identical subarrays with size n can be extracted from the N-element ULA.

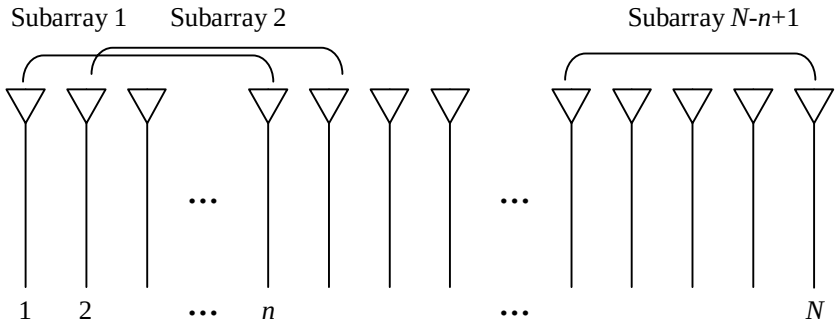

Figure 7: The spatial smoothing technique: the correlation matrix is the average of the correlation matrices of all subarrays.

The correlation matrix can be represented as

$$\overline{\mathbf{R}}_{yy} = \frac{1}{N-n+1} \sum_{k=1}^{N-n+1} \mathbf{R}_{yy}^{(k)}, \tag{64}$$

where $\mathbf{R}_{yy}^{(k)}$ is the correlation matrix of the k^{th} subarray. With m identical subarrays, up to m coherent signal sources are allowed in the parameter estimation [56].

The spatial smoothing technology can be used to not only decorrelate the signals but also increase the number of snapshots for the calculation of correlation matrix [57]. In [57], they estimate the multipath parameters from the impulse response in urban areas. Snapshots were constructed from spatial subarrays instead of from a long observation period because long observation period is not feasible from the impulse response.

2.3 Number-of-Sources Detection Algorithms

The ESPRIT algorithm discussed in previous section assumes that the number of signal sources is a known value. However, this number is usually unknown and must be detected before the estimation can be performed. There exist a great many number-of-sources detection methods. Table 1 shows how several of these methods may be categorized. Next, we will review these methods and indicate their pros and cons. Subsequently, the Data Estimation Error (DEE) and MDL methods, which will be compared with our detection algorithms in Chapter 4, are described in detail.

As shown in Table 1, the number-of-sources detection methods, or the enumeration techniques, can be divided into two main categories: those that treat this problem as a pure detection problem, and those that treat it as a combined detection-estimation problem.

Table 1. Categories of number detection methods.

	Detection		Combined Detection-Estimation	
	Subjective	Objective	Subjective	Objective
Information theoretic criterion	[60]	[17,18,19,56,61]		[58,59,69,70]
Eigenvector		[65]		
Data-Based		[66,67]	[57]	[64]
Threshold	[68]			
Root-finding			[62]	

Compared to the pure detection methods, the combined detection-estimation methods provide better performance, but they also have high computational complexity. This is especially true when maximum likelihood (ML) estimation [58,59] is used, which requires a multi-dimensional search. Therefore, the combined detection-estimation approach is not suitable for real-time applications. According to the different mathematical criteria used in the methods, Categories I and II can be further classified into four and three groups, respectively. Next, we briefly introduce the various methods of each group.

Category I: Pure Detection

- Information theoretic criterion: Statistical hypothesis (SH) [60], Akaike's information criterion (AIC) [17,19], and minimum description length (MDL) [18,19] are the three most popular methods that detect the number of sources based on information theoretic criteria. The methods in this group detect the number by counting the multiplicity of the smallest eigenvalues of the correlation matrix. SH determines the number according to the log-likelihood function followed by a subjective threshold. MDL and AIC eliminate the requirement of this threshold by adding a "degrees of freedom" term after the log-likelihood function. Xu [61]

modified the degrees of freedom to make MDL and AIC suitable for the applications when forward-backward smoothing is applied. There are many ideal assumptions in the deduction of the criterion, which have made it fail in many practical environments, such as under-water [62], sea-surface [63], and multipath measurements in urban area [57] and indoor office [64]. The assumptions include that the noise must have a sphere-like distribution and be uncorrelated between any two sensors, and the number of snapshots is large enough to obtain an accurate correlation matrix.

- Eigenvector-based: Instead of using eigenvalues, the rank of the matrix composed of the eigenvectors can be used for the determination of number of sources. In [65], Di and Tian examine the rank of the matrix formed by appended subarrays, which are derived from the correlation matrix and eigenvectors. The rank increases with the increase of number of subarrays and stabilizes when the rank is equal to the number of sources. Like the information criterion, this method also assumes that the noises of the sensors are mutually uncorrelated, and the noise variance is a known value, the latter of which is usually unavailable in practice. One feature of this method is that it can handle both non-coherent as well as fully coherent signals. It is interesting to notice that the collection of the subarrays is similar to the spatial smoothing, another way to deal with coherent signal sources by summing the correlation matrices of many similar subarrays containing the same signal subspace.

- Data-based: Similar to previous methods, Di [66] provides another way to detect the number of sources by stabilizing the rank. Instead of the eigenvectors, they use the correlation matrix of the received data of the sensors. Its performance and

drawback are similar to eigenvector-based method. Krim and Cozzens [67] proposed a data-based enumeration technique, which also uses rank stabilization to detect the number. However, Krim and Cozzens used a different approach, which applies MDL on the prediction errors of a linear model. One potential problem is that the calculation of the error needs a singular value decomposition (SVD) of the accumulated data matrix. The data matrix becomes very large when the number of snapshots or subarrays is large. In that case, the pre-whitening process required in this method also requires intensive calculation.

- Threshold: Chen [68] showed a method that detects the number by setting an upper bound on the values of the eigenvalues. Because this bound is determined by an adjustable parameter, its performance is better than MDL at low SNR and better than AIC at high SNR. However, the decision of the value of this parameter depends on *a priori* information, such as the probability of false alarm, probability density function (PDF) of eigenvalues, SNR level, etc. In many applications some of the information is not available, in which case the parameter must be subjectively selected based on empirical decision.

Category II: Combined Detection-Estimation

- Information theoretic criterion: Wax and Ziskind [58] proposed a method that simultaneously solves the detection of number of sources and multiple sources localization problems. The detection is based on MDL algorithm, while the localization is optimized by ML estimation. With this approach fully coherent signals can also be handled. Wax improved the performance via the ML estimator derived by Bohme [59]. Wax further proposed a solution that is applicable to

arbitrary array geometry and the condition when unknown noise with arbitrary covariance matrix is present [69]. Another approach derived the number and parameters based on Bayesian predictive densities (BPD) and marginal Bayesian estimator [70]. A common drawback of these methods is the knowledge of the array manifold is required. In many cases this information is not available, or there exist errors in the estimated array manifold, which will distort the detection and estimation results.

- Data-based: Kuchar [57] presented a method that determines the number of sources by selecting the one that minimizes the data estimation error (DEE), the difference between the received data and the reconstructed data, which is derived from the estimates obtained by ESPRIT algorithm [13]. The drawback of this method is the DEE decreases with the increase of assumed number of sources because of the increase of degrees of freedom. Therefore, like the SH method, this method also needs a subjective decision on the selection of local minimum of DEE.

- Root-finding: Silverstein [71] showed that if the assumed number of sources is correct in ESPRIT, the roots must be on the unit circle, and the roots caused by overestimation tend to deviate from the circle. No specific criterion is provided to determine the number of sources. Kotanchek [62] made use of a similar property in another estimation method, generalized eigenvalues utilizing signal subspace eigenvectors (GEESE), to detect the number according to the deviation of the roots from the unit circle. However, a subjective threshold must be decided in initial detection, and some other follow-up steps are necessary to track if the initial detection is appropriate.

2.3.1 Minimum Description Length Algorithm

From (13), assuming the noise is AWGN with variance σ^2, the correlation matrix of the array signal is

$$\mathbf{R}_{yy} = \mathbf{A}\mathbf{R}_{ss}\mathbf{A}^{\dagger} + \sigma^2\mathbf{I}. \tag{65}$$

Given L signal sources and an array with N elements, the L largest eigenvalues of $\mathbf{R}_{yy}$ are corresponding to the signal subspace, and the smallest N-L eigenvalues are identical and corresponding to the noise subspace. The relationship of the eigenvalues is

$$\zeta_1 \geq \zeta_2 \geq \cdots \zeta_L > \zeta_{L+1} = \zeta_{L+2} \cdots = \zeta_N . \tag{66}$$

Therefore, the number of sources can be obtained by counting the number of smallest identical eigenvalues. However, in practice the observation time or the number of snapshots of the array signal to calculate the $\mathbf{R}_{yy}$ is limited, and the eigenvalues of the estimated $\mathbf{R}_{yy}$ are not identical. Therefore, counting the multiplicity of the smallest eigenvalues is not a practical solution.

The MDL information criterion for model selection was introduced in [18] and first applied to determine the number of sources in the array signal processing in [19]. The model selection problem can be described as searching for the best model that fits the data based on P observations of the data $\mathbf{Y} = [\mathbf{Y}(1) \quad \mathbf{Y}(2) \quad \cdots \quad \mathbf{Y}(P)]$ and the given probability density function of $f(\mathbf{Y}|\boldsymbol{\Theta})$, where $\boldsymbol{\Theta}$ is a vector containing all of the parameters in the model. According to the MDL algorithm, the model is selected to minimize the MDL criterion, which is defined as

$$MDL = -\log f\left(\mathbf{Y}\middle|\hat{\boldsymbol{\Theta}}\right) + \tfrac{1}{2}\gamma \log(P), \tag{67}$$

where $\hat{\boldsymbol{\Theta}}$ is the estimate of the parameters $\boldsymbol{\Theta}$, and γ is the number of parameters in $\boldsymbol{\Theta}$ that can be freely adjusted.

For array signal processing, assuming N snapshots of the received array signals are i.i.d. complex Gaussian random vectors with zero mean, the estimated correlation matrix is derived by

$$\hat{\mathbf{R}}_{yy} = \frac{1}{P}\sum_{i=1}^{P}\mathbf{Y}(i)\mathbf{Y}(i)^{\dagger}. \tag{68}$$

Assuming the number of signal sources is k, the estimated correlation matrix can be represented as

$$\hat{\mathbf{R}}_{yy}^{(k)} = \mathbf{U}^{(k)}\left[\Lambda - \sigma^2\mathbf{I}\right]\mathbf{U}^{(k)\dagger} + \sigma^2\mathbf{I}, \tag{69}$$

where $\mathbf{U}^{(k)} = [\mathbf{u}_1\ \mathbf{u}_2\ \cdots\ \mathbf{u}_k]$. It follows that the parameters in the model are

$$\boldsymbol{\Theta}^{(k)} = \left(\zeta_1, \zeta_2, \cdots, \zeta_k, \sigma^2, \mathbf{u}_1, \mathbf{u}_2, \cdots, \mathbf{u}_k\right). \tag{70}$$

In (70), $\boldsymbol{\Theta}^{(k)}$ has k+1+2Nk parameters, but the number of independently adjustable parameters $\gamma = k(2N–k+1)$ after the reduction of the dependent parameters due to the properties of unit-norm and mutual orthogonality of the eigenvectors.

The probability density function is

$$\begin{aligned} &f\left(\mathbf{Y}(1), \cdots, \mathbf{Y}(P)\middle|\Theta^{(k)}\right) \\ &= \prod_{i=1}^{P}\frac{1}{\pi^N \det\mathbf{R}_{yy}^{(k)}}\exp\left[-\mathbf{Y}(i)^{\dagger}\left(\mathbf{R}_{yy}^{(k)}\right)^{-1}\mathbf{Y}(i)\right]. \end{aligned} \tag{71}$$

Replacing $f(\mathbf{Y}|\boldsymbol{\Theta})$ in the MDL criterion with (71), we obtain

$$MDL(k) = -\log\left(\frac{\prod_{i=k+1}^{N}\hat{\zeta}_i^{1/(N-k)}}{\frac{1}{N-k}\sum_{i=k+1}^{N}\hat{\zeta}_i}\right)^{(N-k)P} + \tfrac{1}{2}k(2N-k+1)\log P, \tag{72}$$

where $\left\{\hat{\zeta}_i \middle| i = 1, \cdots, N\right\}$ are the eigenvalues of $\hat{\mathbf{R}}_{yy}$. The detected number of sources is

$$\hat{L} = \arg\min_k MDL(k). \tag{73}$$

2.3.2 Detection Estimation Error (DEE) Detection Algorithm

The detection of number of sources based on the detection estimation error is introduced in [57] for multipath estimation in urban areas. The DEE is a combined detection-estimation method, where the employed estimation algorithm in [57] is the ESPRIT algorithm. Assuming the number of signal is *k*, the ESPRIT algorithm can be employed to estimate the parameters. In turn, the estimated steering matrix $\hat{\mathbf{A}}$ can be deduced from the estimated parameters, and the signal sources $\hat{\mathbf{s}}$ can be recovered by

$$\hat{\mathbf{s}} = (\hat{\mathbf{A}}^{\dagger}\hat{\mathbf{A}})^{-1}\hat{\mathbf{A}}^{\dagger}\mathbf{Y}. \tag{74}$$

The array signal is then reconstructed by

$$\hat{\mathbf{Y}} = \hat{\mathbf{A}}\hat{\mathbf{s}}. \tag{75}$$

The detection estimation error assuming the number of sources is *k* is defined as

$$DEE(k) = \frac{\left\|\hat{\mathbf{Y}} - \mathbf{Y}\right\|_2}{\left\|\mathbf{Y}\right\|_2}, \tag{76}$$

where $\left\| \bullet \right\|_2$ stands for $\mathbf{L}_2$-norm. The *DEEs* of all possible values of *k* are calculated using the same procedure, and the detected number of sources is determined by searching some local minimum of *DEE*(*k*). Because larger number of *k* provides more degrees of freedom in modeling the noise, the global minimum of *DEE* usually occurs at the maximum allowed number of *k*; therefore, the global minimum cannot be used to determine the number of sources. Consequently, the selection of the local minimum of *DEE* is

subjective. In Chapter 4, we will propose a modified version, which is based on the residual estimation error (REE) and which detects the number of sources using the global minimum, thus eliminating the requirement of the subjective selection in the DEE method.

2.4 Various Configurations of MIMO Channel Measurement Systems

MIMO channel measurement systems are comprised of two parts: (1) the channel sounding system, which is used to measure the frequency response or impulse response of the channel, and (2) configurations of multiple antennas at both ends. The channel sounding system part is nothing different from what is employed in traditional SISO sounding system. Therefore, in this section we only review the channel sounding system briefly with more focus on introducing various antenna configurations.

The impulse response can be measured either on the time domain or the frequency domain [72]. For the time-domain measurement, the transmitted signal waveforms are either the pseudo random (PN) spread spectrum signal or periodical short pulse. When the transmitted signal is PN spread spectrum signal, some post processing such as sliding correlator and modulator must be implemented to retrieve the impulse response. The direct pulse transmission method is usually used to measure the power-delay profile instead of the impulse response because the receiver is noncoherent and the phase information is not available. Another disadvantage of the direct pulse transmission method is the short coverage area because of low duty cycle of the short pulse.

The network analyzer is the crucial equipment in the frequency-domain measurement system. The transmitted signal is generated by a synthesized sweeper, which sweeps from the lowest to the highest frequency. Accordingly, the frequency response of the channel is obtained directly and no post processing is required. However, because of the sweeping, the frequency-domain measurement system requires longer acquisition time than the time-domain measurement. Considering the advantage of simple frequency response acquisition, we choose the frequency-domain measurement scheme as the infrastructure of our channel sounding system.

So far three kinds of antenna configurations have been employed for MIMO channel measurement: *real antenna array* [14,28], *virtual antenna array* [73,74], and *highly directional antenna* [75]. This section compares these three configurations and provides a justification for the choice of the virtual antenna array for this dissertation.

In the *real antenna array* configuration, multiple antennas are placed at both ends of the link. This method has the advantage of fast measurement since all the antenna elements can transmit or receive the signals simultaneously; therefore, the stationary environment is not necessary, which makes the measurement of the Doppler effect possible. The primary drawbacks of this method are the mutual coupling effect among the antenna elements and the prohibitive cost of the large number of antennas and microwave transmitters and receivers. The mutual coupling effect changes the antenna patterns of close antenna elements, thus extra calibration is required to move the effect in parameter estimation [41]. In addition, the antenna spacing of the real arrays is usually fixed, which makes it difficult to investigate the effects of various array geometries and element spacing on the performance of MIMO channels.

The *virtual antenna array* configuration, on the other hand, completely eliminates the mutual coupling effect and significantly reduces the cost since only a single antenna is utilized at each end of the link. In this scenario, the array is emulated by moving the antenna to pre-preprogrammed positions; in consequence, the array geometry and element spacing can be arbitrary. However, due to the sequential measurement at each antenna position, virtual antenna array needs a long period of time to finish the measurement, and the stationarity of the environment must be maintained during the entire measurement. Because of the requirement of stationarity, the measurement is usually conducted after midnight, and no moving objects or people are allowed during the measurement, implying that the investigation of the Doppler effect is not realizable with this approach.

The *highly directional antenna* is the third approach to estimate the angular parameters, including the DOA and DOD. With this configuration, the angular estimates are obtained by mechanically rotating the highly directional antennas (with beamwidth less than 5°) at both ends to measure the power distribution of each DOA-DOD pair. The advantage of this method is that no sophisticated angle estimation algorithm is required. The main disadvantages of this approach are that the angular resolution is limited by the beamwidth of the directional antenna, and the elevation angles of the paths are usually ignored. Like the virtual antenna array, the measurement with the highly directional antenna also needs to be taken within the channel coherence time; therefore, the Doppler effect cannot be determined with this approach. Moreover, since the MIMO channel matrix is not measured, some properties like the channel capacity cannot be obtained directly with this method.

Considering the prohibitive cost and inflexibility of the real antenna array, and the limitation in the parameter estimation of the directional antenna approach, we finally adopted the virtual antenna array as the basic infrastructure for our MIMO channel measurement testbed.

2.5 Chapter Summary

This chapter provides necessary background for the research of this dissertation. First, we introduced the fundamentals of the MIMO technology and the channel capacity of OL-MIMO with or without interference. Various parameter estimation algorithms for the acquisition of the angular information of multipath were surveyed. Specifically, the ESPRIT algorithm, which is adopted in this research because of its advantages of robustness against model errors and low computational complexity, was described in details. A survey of the algorithms for the detection of number-of-sources, which is a prerequisite in many parameter estimation methods, was provided. At last, we demonstrated current MIMO measurement antenna configurations and compared their pros and cons.

Chapter 3

MIMO Channel Measurement System

In previous chapter, we have introduced background relating to the MIMO technology, channel characterization, parameter estimation, detection of number of sources, and various antenna configurations for MIMO channel sounding system. In this chapter, we will describe our MIMO channel sounding system in detail and demonstrate the measurement procedure as well as the post-measurement calibration. The use of the virtual antenna array to acquire MIMO channel matrices will be validated by comparing the measurement results obtained by virtual and real antenna arrays. This measurement system was integrated as part of the dissertation effort. The measured MIMO channel matrices obtained by the system described in this chapter will be used in the following chapters for parameter estimation, validation of propagation channel model, MIMO channel capacity evaluation, and performance comparison of some technologies, such as beam selection and antenna selection schemes.

3.1 Overview of Our Measurement System

As illustrated in Figure 8, our MIMO channel measurement system is composed of two parts: (1) the Agilent's HP 85301B stepped-frequency antenna pattern measurement system, which, because of its coherent reference signal, can measure the channel frequency response directly, and (2) the actuator positioning system, which

creates the virtual antenna array by moving the antenna to arbitrary pre-programmed locations. A remote computer is used to control and integrate the HP85301B and the actuator subsystems through the general-purpose interface bus (GPIB) and RS232 serial port, respectively. In the next two subsections, we will introduce these two primary subsystems in detail.

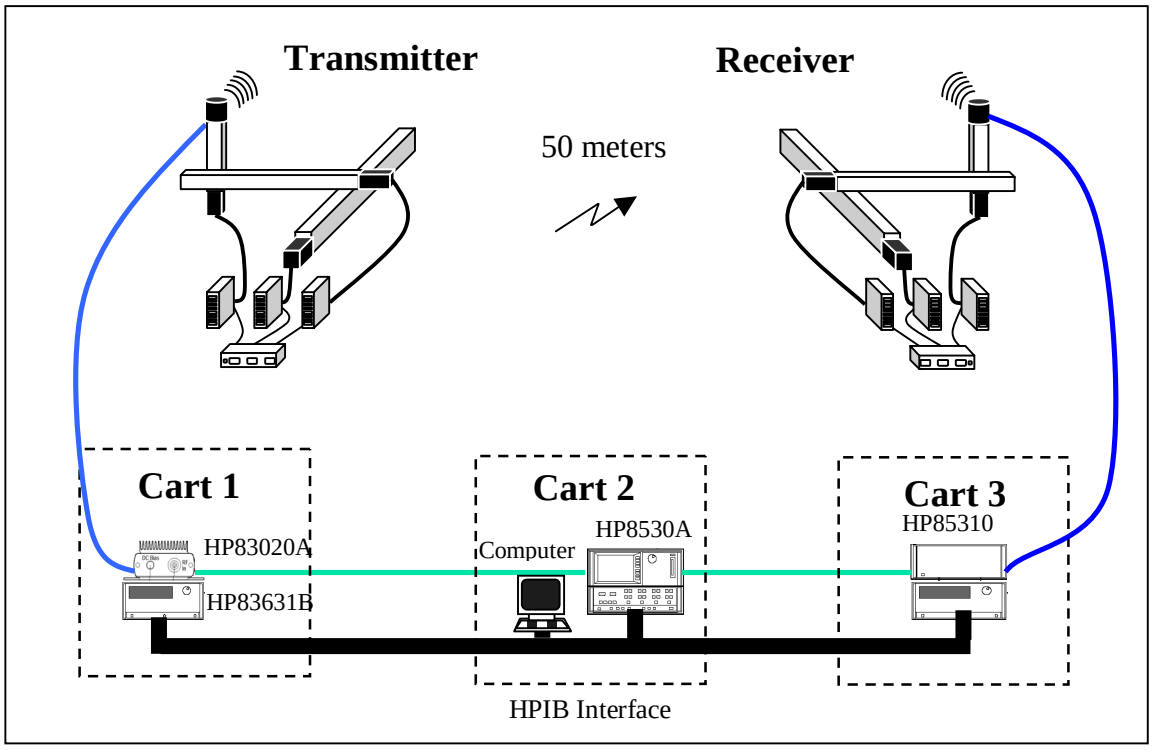

Figure 8: Overview of our MIMO measurement system. The measurement system is based on virtual antenna array scenario and composed of two parts. The lower part is the HP85301B antenna pattern measurement system, and the upper part is the 3D actuator system.

3.1.1 HP85301B Stepped-Frequency Antenna Pattern Measurement System

HP85301B measurement system can be divided into two separate parts: the transmit site and the receive site. The transmit site consists of the RF transmit source

(HP83631B), RF power amplifiers (83020A), transmit antenna, and the reference link that is used to provide the reference phase to the receive site. The receive site includes the receive antenna, the microwave receiver (8530A), local oscillator (LO) source (83621B), and RF downconverter (HP85310A). Originally designed to measure the wideband antenna pattern, HP85301B has been employed in some anechoic chambers. This channel measurement system allows us to measure the frequency response of the channel from 2-18 GHz with signal dynamic range of 89 dB. The functionality and specification of the crucial equipment are described below.

- *HP83631B synthesized sweeper:* HP83631B is a broadband frequency synthesizer that operates from 0.045 to 26.5 GHz. The HP83631B is utilized as the RF signal source generator in the transmitter site. In the measurement, the synthesized sweeper must warm up for at least one hour to ensure that the electrical characteristics are stabilized.
- *HP83020A RF amplifier:* Because of the limited output power of the RF signal source, HP83020A RF amplifier must be used to increase the RF output power to increase the system dynamic range, and compensate the power loss caused by the connectors, cables, signal routing components, and some obstructive objects in the measurement environment like walls and floors. HP83020A provides a gain of 30dB with maximum output power of 1 Watt.
- *HP85310A distributed frequency downconverter*: The three major components of the HP 85310A are the HP 85309A LO/IF distribution unit, the HP85320A test mixer, and the HP 85320B reference mixer. The HP 85310A downconverts the

RF signal to the intermediate frequency (IF) band (20MHz) and then sends the IF signal to the microwave receiver HP8530A.

- *HP8530A microwave receiver*: Driven by the 32-bit Motorola 68020 microprocessor, HP8530A is a microwave receiver that has been designed specifically for antenna pattern measurement. The HP 8530A receives the 20 MHz IF test and reference signals, which are downconverted from the microwave band by HP85310A. HP8530A can measure signals of -113 dBm from 2 to 18 GHz. The excellent sensitivity and embedded averaging function improves the SNR of the system, allowing us to measure weak signals with greater accuracy. During the frequency domain measurement, the test signal source is swept from a lower to a higher frequency, and the measured amplitude and phase data are transferred to the computer. This subsystem is remotely controlled from the computer with GPIB interface.
- *RF Antennas*: The model EM-6865 omni-directional wideband antennas are employed in both the transmit and receive sites. This antenna is a vertically polarized biconical antenna operating from 2 to 18 GHz. The antenna gain at 5.8 GHz is 3.6 dBi. The antenna pattern, which was measured in the anechoic chamber of the Georgia Institute of Technology, is shown in Figure 9(a). The measured antenna pattern at 5.8 GHz is shown in Figure 9(b), where the radial axes is in units of dB. We also use another antenna, Seavey 9845-800, which provides flatter frequency response but narrower bandwidth. This antenna is also biconical and vertically polarized, operating from 4 to 6 GHz with antenna gain 5 dBi.

- *Cables*: The aforementioned instruments are interconnected with cables. Depending on the frequency band of the signal, two different cables are utilized: one is the RF cables, while the other is the IF cables. The RF cables convey the RF signal source at the transmit site, and received RF signal and the LO signal for two mixers at the receive site. The IF cables, on the other hand, transfer the downconverted IF signal and the signals that synchronize the operation of all equipment. Since the purpose of the measurement system is to capture the complex gains of channels, the phase stability is especially important for the RF antenna cables because they move with the actuator system during the measurement. For this reason, the RF antenna cables of our measurement system are high precision RF cables with phase difference less than 1° [76].

A list of the equipment specifications of HP85301B components is provided in Table 2.

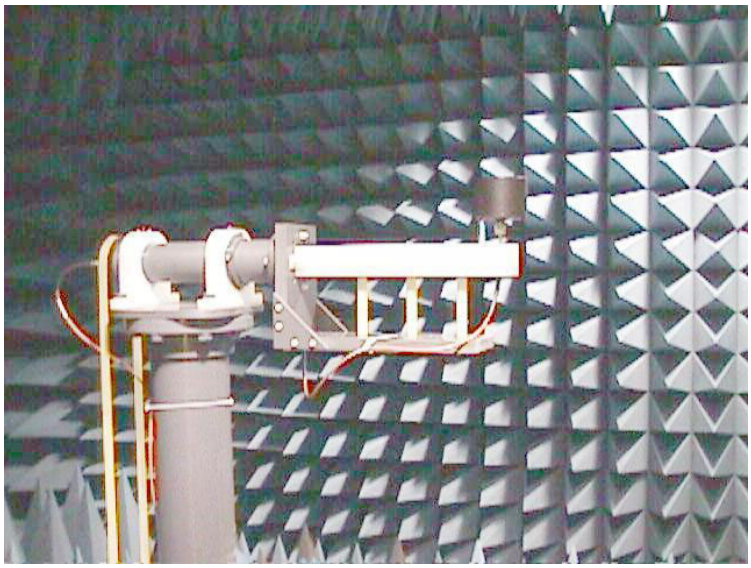

(a)

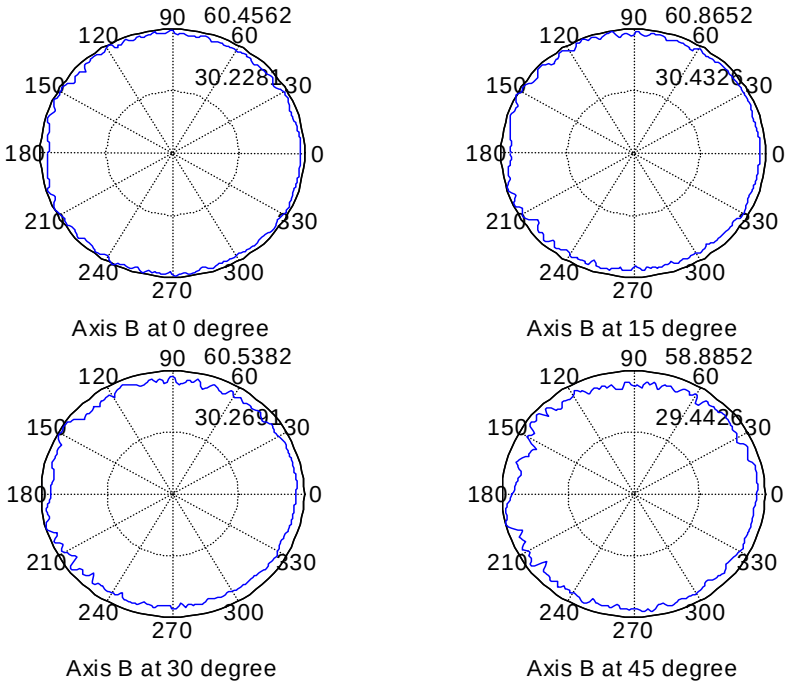

Figure 9: (a) Antenna pattern measurement conducted in the anechoic chamber of the Georgia Institute of Technology. (b) Measured antenna pattern at 5.8 GHz. The antenna is nearly omni-directional.

Table 2:The specifications of the equipment.

Component	Equipment	Functions & Specs
Transmit source	HP83631B synthesized sweeper	Frequency range : 0.045 – 26.5GHz Max. output power : < 20 GHz, +13 dBm : 20-26.5 GHz, +10 dBm Resolution : 1 Hz
Amplifier	HP87422 power supply and HP83020 power amplifier	Frequency range : 2 –26.5 GHz Gain : 30 dB Max. output power : 30 dBm
LO source	HP83621B synthesized sweeper	Frequency range : 0.045 – 20GHz Max. output power : +13 dBm Resolution : 1 Hz
RF downconverter	HP85320A/B Mixers	Downconvert RF signal to IF band Sensitivity : -113 dBm Dynamic range : 89 dB
	HP85309A LO/IF distribution unit	1. Receive LO source and provide it to the mixers 2. Receive IF signals and send it to the microwave receiver
Microwave receiver	HP 8530A microwave receiver (HP85101C Display/Processor + HP85102R IF/Detector)	1. Synchronize and control the RF transmitter and the RF receiver 2. Receive and display the IF signal 3. Send the data to computer
Antenna (for Tx & Rx)	EM 6865 omni-directional wideband antenna	Type : Biconical Frequency range : 2-18 GHz Polarization : Vertical Gain : 2.6 dB at 5.5GHz 3.5 dB at 17.0 GHz Max. power : 5W VSWR : <2:1 Output impedance: : 50Ω Interface : Type “N” female Weight : 1 lbs
	9845-800 omni-directional wideband antenna	Type : Biconical Frequency range : 4-6 GHz Polarization : Vertical Gain : 5 dBi at 5.8GHz Max. power : 10W VSWR : <2:1 Output impedance: : 50Ω Interface : SMA female Weight : 0.5 lbs

3.1.2 3D Actuator Systems

Driven by three brushless motors, the actuators can translate the antenna through a volume of approximately 20″ × 20″ × 3″ with the minimum position step less than 0.0004″. The 3″ in the Z-direction ensures that the angles of the paths arriving at nearly all elevations can be identified. The structure of the 3D actuator system and the size of each actuator is illustrated in Figure 10. For convenience, a mobile platform is also prepared to move both actuator systems to various locations, as shown in Figure 11. Figure 12 demonstrates a picture of the entire measurement system in the Residential Laboratory of the Georgia Institute of Technology. The antennas are mounted on plastic telescoping masts such that the antenna can be positioned at heights ranging from 4 to 5 feet from the floor.

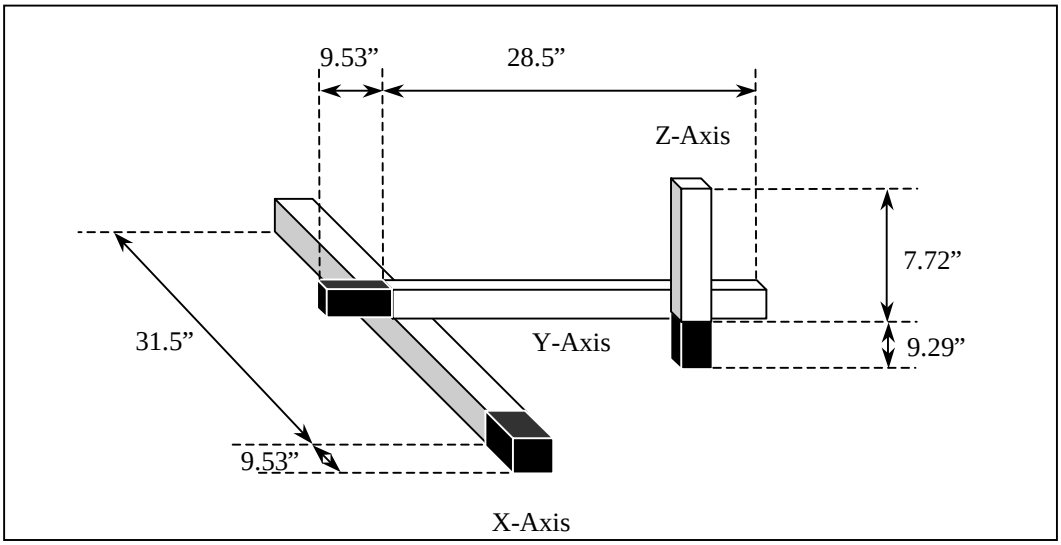

Figure 10: 3D Actuator system. Each actuator is driven by a brushless motor.

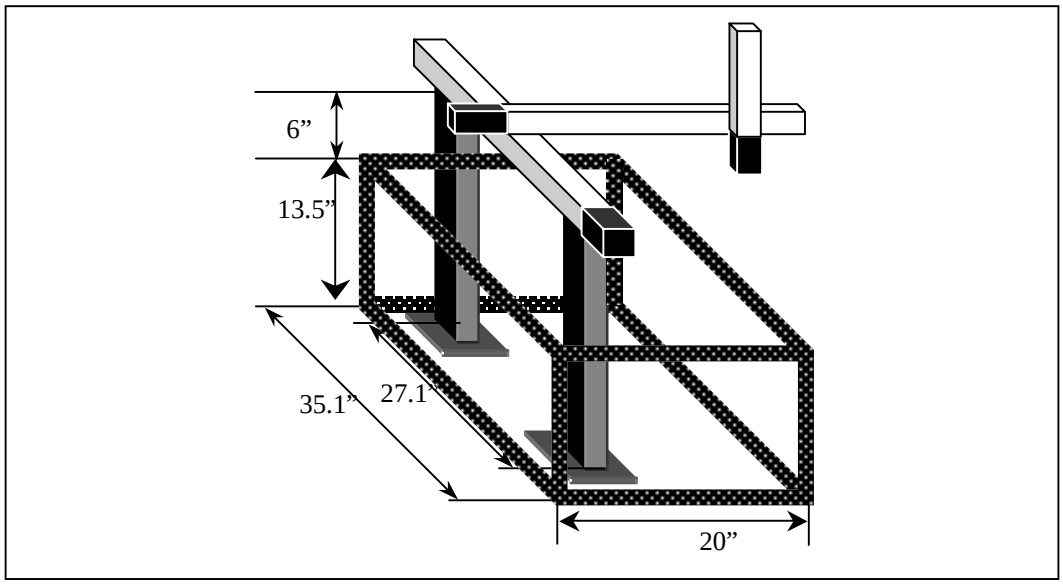

Figure 11: The 3D actuator system is placed upon a mobile platform for the convenience of changing transmit and receive locations.

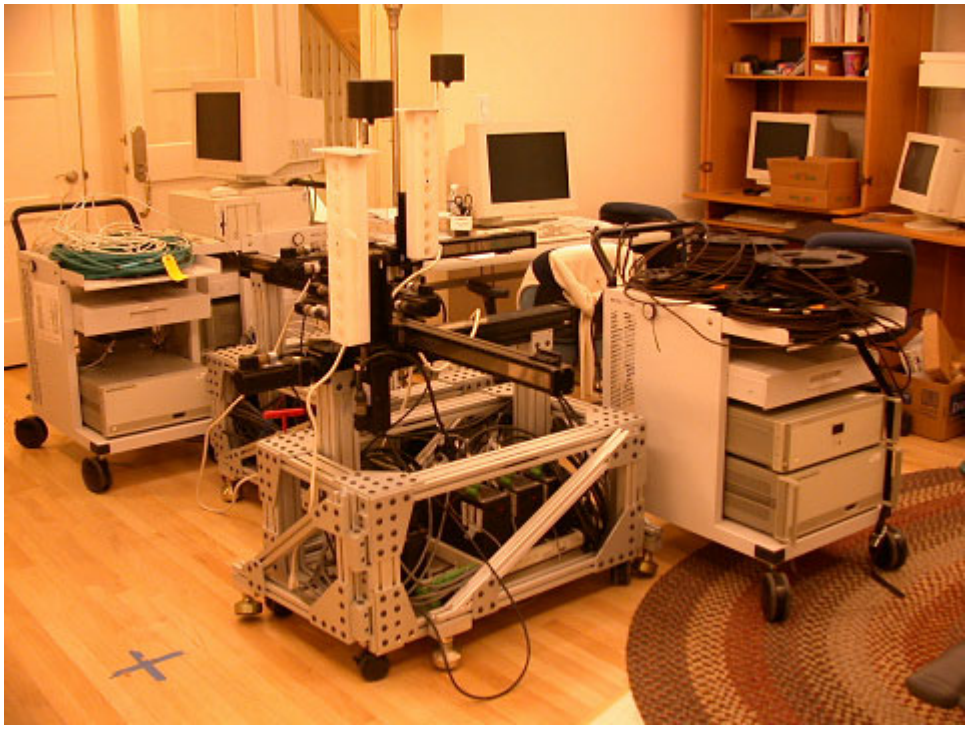

Figure 12: 3D MIMO measurement system in the Residential Laboratory. The HP measurement system is placed in three carts, and the antennas are placed on plastic telescoping masts attached on the actuator systems.

3.2 Measurement Procedure and Back-to-Back Calibration

The overview with detailed interconnection of HP 85301B antenna pattern measurement system is illustrated in Figure 13. The multi-channel controller (HP85330), switch control unit (HP 85332A) and the solid-state pin switches are also included in the overview. With the HP85330A, switch control units, and the switches, one may measure MIMO channels with up to four real antennas at both ends, but they are not required when the measurement is conducted with virtual antenna array. In this dissertation, HP85330A, switch control units, and the switches are only used in the measurement in Section 3.4 to validate the virtual antenna array. The measurement and calibration procedure is not affected whether or not the HP 85330A and switch control units are included.

In the measurement, the RF signal source HP85301B sweeps from the lowest to the highest frequency. The received raw data is the ratio of the testing signal over the reference signal, i.e.

$$H_{raw}(f) = S_{test}(f) / S_{ref}(f), \tag{77}$$

where

$$\begin{aligned} S_{test}(f) &= S(f) \cdot H_{test}(f) \\ S_{ref}(f) &= S(f) \cdot H_{ref}(f) \end{aligned}. \tag{78}$$

The $S(f)$ represents the transmitted RF signal, and $H_{test}(f)$ and $H_{ref}(f)$ are the frequency responses of the components in the testing and reference signal traces, respectively. As shown in Figure 13, the components in testing trace comprise cables A1, A2, A3, B3, B4, RF amplifier, coupler, wireless channel, HP 85320A mixer, transmit and receive antennas. The reference trace is comprised of cables A1, A2, E1, C3, RF

amplifier, coupler, 30dB attenuator, and HP 85320B mixer. After the division in (77), the responses of common components, including cables A1, A2, RF amplifier, and the coupler, are eliminated. However, the $H_{raw}(f)$ still contains the responses of cables A3, B3, B4, E1, C3, 30dB attenuator, both mixers, and both antennas.

Figure 14 shows an example of the frequency response and impulse response of the measured raw data. In the measurement, the center frequency is 5.8 GHz and the bandwidth is 500 MHz. The distance between the transmitter and the receiver is about 2.56 meters, and the LOS component is available. Although the reference signal provides the phase reference for the testing signal, the measured raw data include not only the desired channel frequency response, $H_{channel}(f)$, but also the responses of the other instruments. This explains why the delay of LOS path is around 680 *ns*, as seen in Figure 14(b), which is supposed to be 8.5 ns for a distance of 2.56 meters. In order to extract the desired channel frequency response, the responses of the other instruments must be removed from the raw data. This procedure is called calibration.

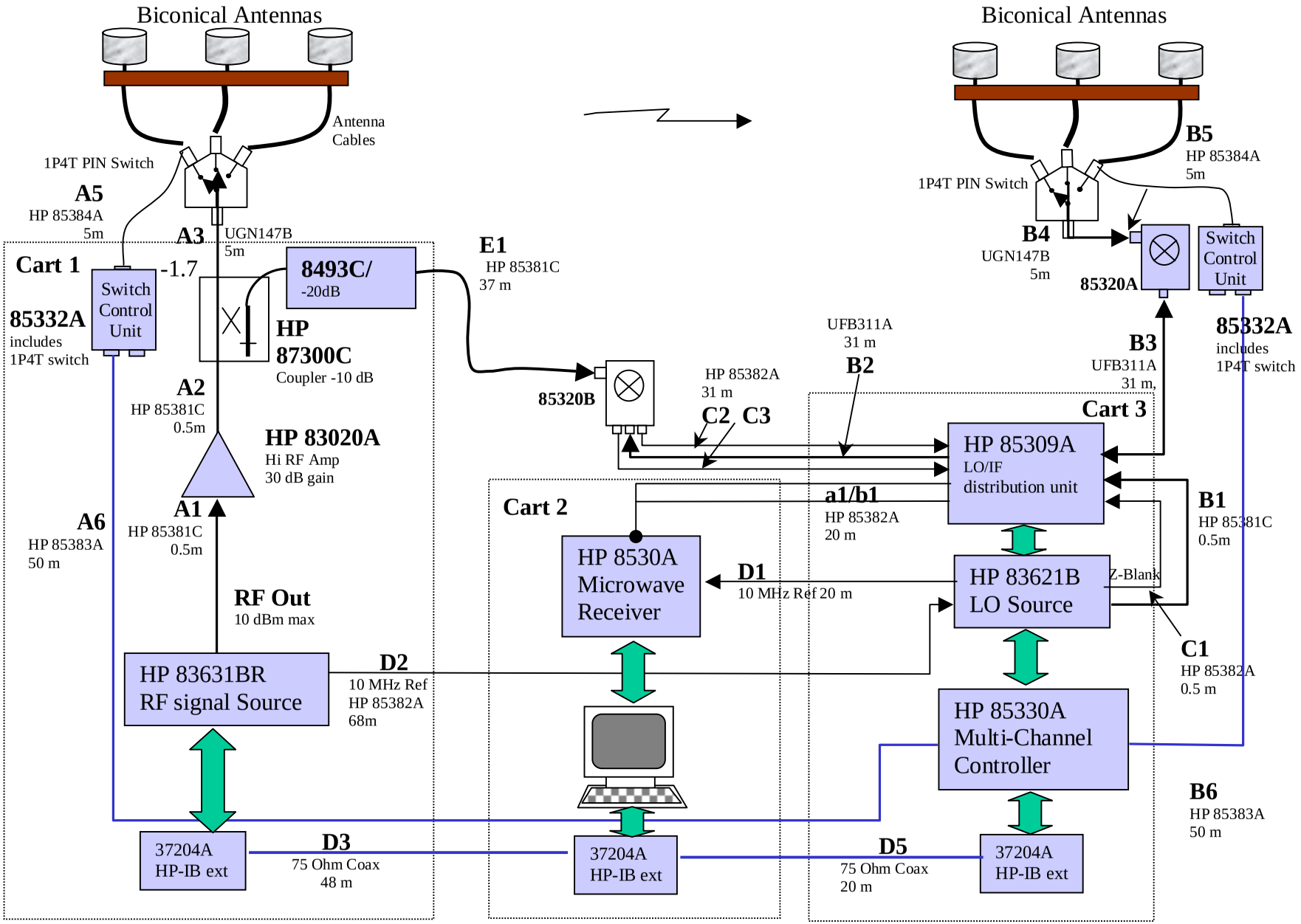

Figure 13: HP 85301B measurement system overview.

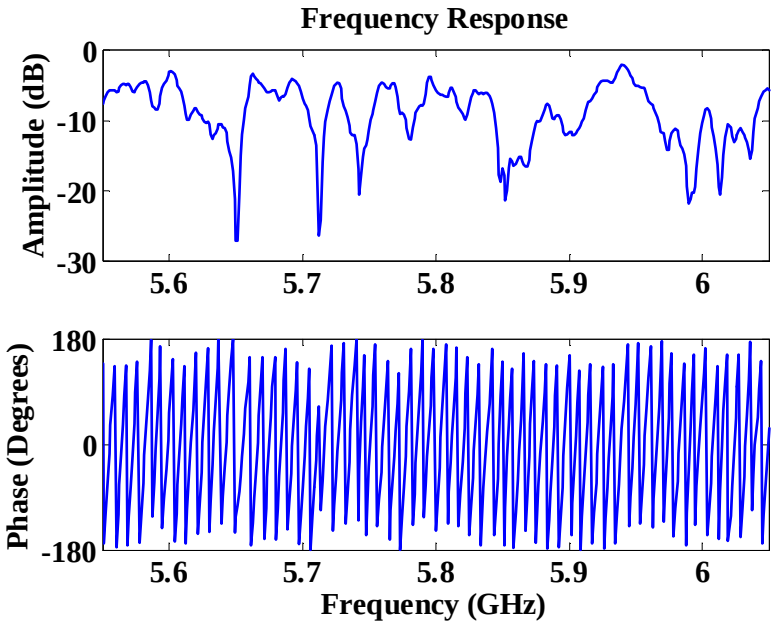

(a)

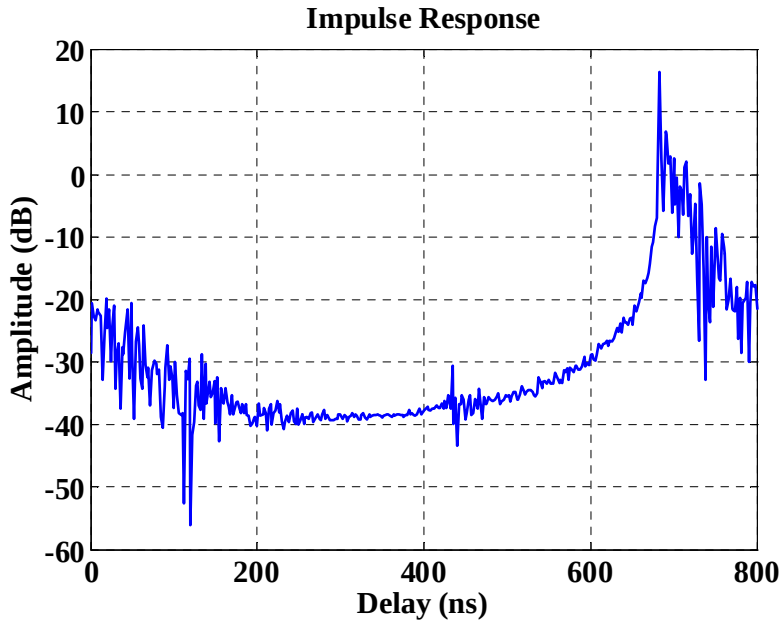

(b)

Figure 14: Measured raw data on (a) the frequency domain and (b) the time domain before the calibration is performed.

Back-to-back calibration, which is used in our measurement, is the most common and simple way to remove unwanted responses of the other equipment. In the back-to-back calibration, wireless channel and two antennas are replaced by a calibration

connector in the testing signal trace. The transfer function of the calibration connector, which is already known and provided by the manufacturer, is saved in the HP8530A. During the measurement, the transfer function of this connector is automatically removed by the HP8530A, and the content of the measured data, denoted as $H_{system}(f)$, contains the responses of cables A3, B3, B4, E1, C3, 30dB attenuator, and both mixers.

The desired channel frequency response is derived by dividing $H_{raw}(f)$ by $H_{system}(f)$, i.e.

$$H_{desired}(f) = \frac{H_{raw}(f)}{H_{system}(f)}. \tag{79}$$

In fact, $H_{desired}(f)$ contains not only the frequency response of the channel but also the responses of two antennas. In order to remove the response of the antennas, the antenna pattern must be measured in the anechoic chamber. However, the measurement procedure for the antenna pattern is impractical because the bandwidth of 500 MHz is too wide and the frequency response varies with DOA. Therefore, in the following chapters, we assume that the antenna is omni-directional and the transfer function has a constant antenna gain. In many cases the antenna gain has no effect because the channel matrix is normalized before further analysis. The calibrated impulse response is shown in Figure 15. After the calibration, the system response is removed, and the delay of LOS path occurs at 8 *ns*. The error of 0.5 *ns* is because the temporal resolution of the impulse response is 2 *ns*, which can be improved by applying the high-resolution estimation algorithm to the measured data.

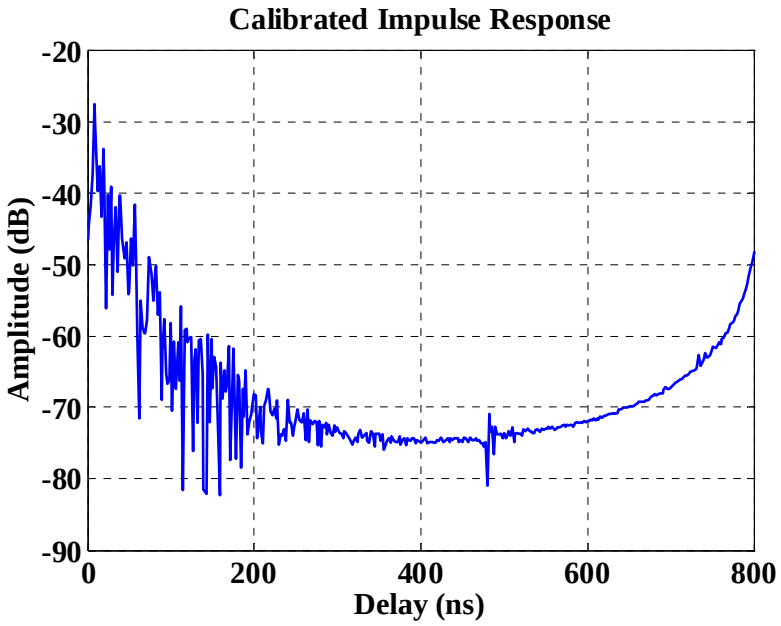

(b)

Figure 15: The channel impulse response after back-to-back calibration.

3.3 Channel Stability Test

As mentioned in Section 2.5, the main problems of measurement systems based upon virtual antenna arrays are long measurement time and the requirement of stationary environment during the measurement. Therefore, the stability of the channel must be assessed before the formal measurements are conducted for further analysis. In this section, we present the measurement taken in the SARL at the Georgia Institute of Technology to test the stability of the channels.

Figure 16 shows the floor plan of the SARL. In the measurement, the locations of the transmitter and receiver are at T3 and R4, respectively. As a consequence, the LOS component is not available. The transmitter is a single antenna, and the receiver is a 4-element uniform linear array (ULA) with antenna spacing 2.48 cm (equal to 0.48 wavelength for 5.8 GHz signal). The measured data is the wideband frequency response

with 401 frequency samples over a bandwidth of 500 MHz centered at 5.8 GHz. In other words, in each measurement, we obtain a (1,4) SIMO channel with 401 frequency samples at each antenna position. The same measurement is conducted for 60 times during a period of 5 hours, which is the longest time required for the parameter estimation measurements in Chapter 5. The abundant frequency samples are used for the calculation of correlation coefficient between the measurements.

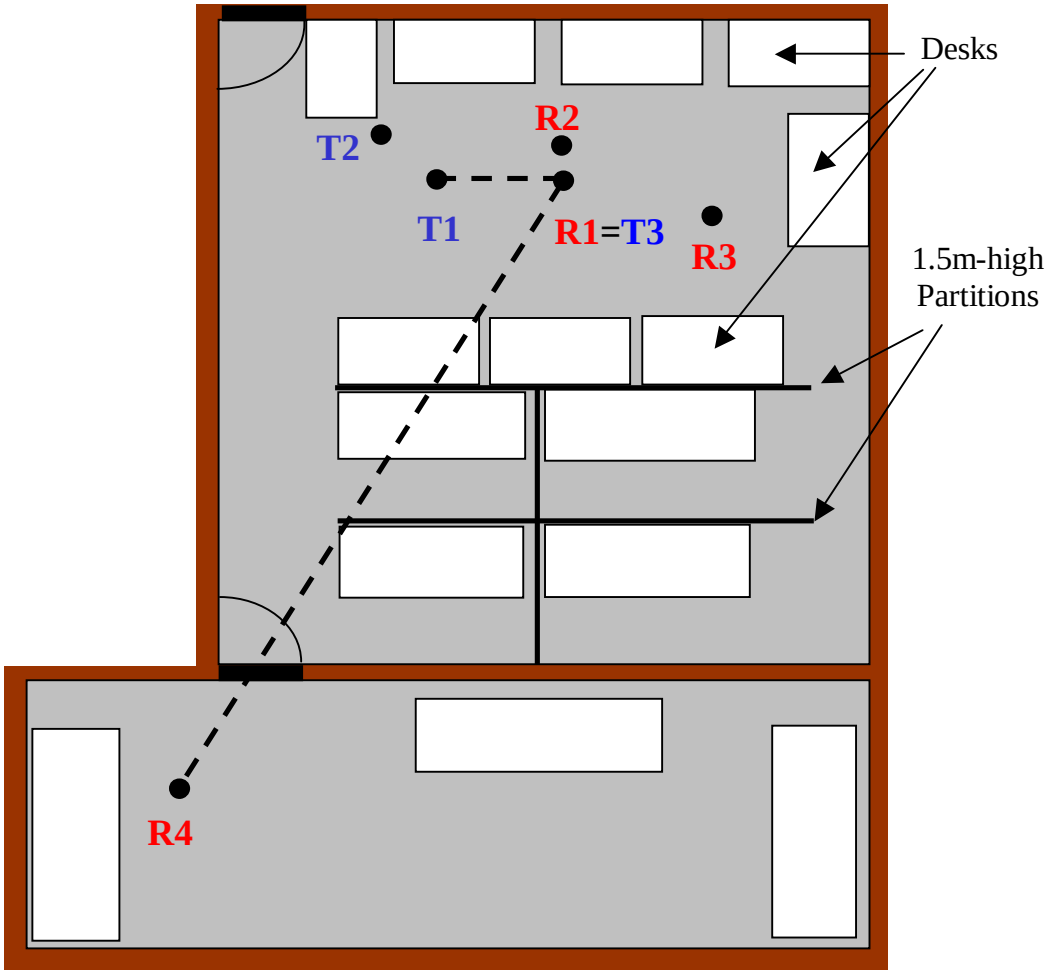

Figure 16: Floor plan of the Smart Antenna Research Laboratory (SARL) at the Georgia Institute of Technology.

If the channel is perfectly stationary, the results of these 60 measurements are supposed to be identical, and the correlation coefficient of the later 59 measurements with

the first measurement is equal to 1 for each receive antenna position. In practice, these measurements cannot be identical because of some disturbance caused by, for example, the spinning computer fan and the operating air conditioner. The stability test results are shown in Figure 17. The correlation coefficients are larger than 0.995, indicating high repeatability of our measurements. This measurement results tell us that the virtual antenna array is feasible in the indoor environment.

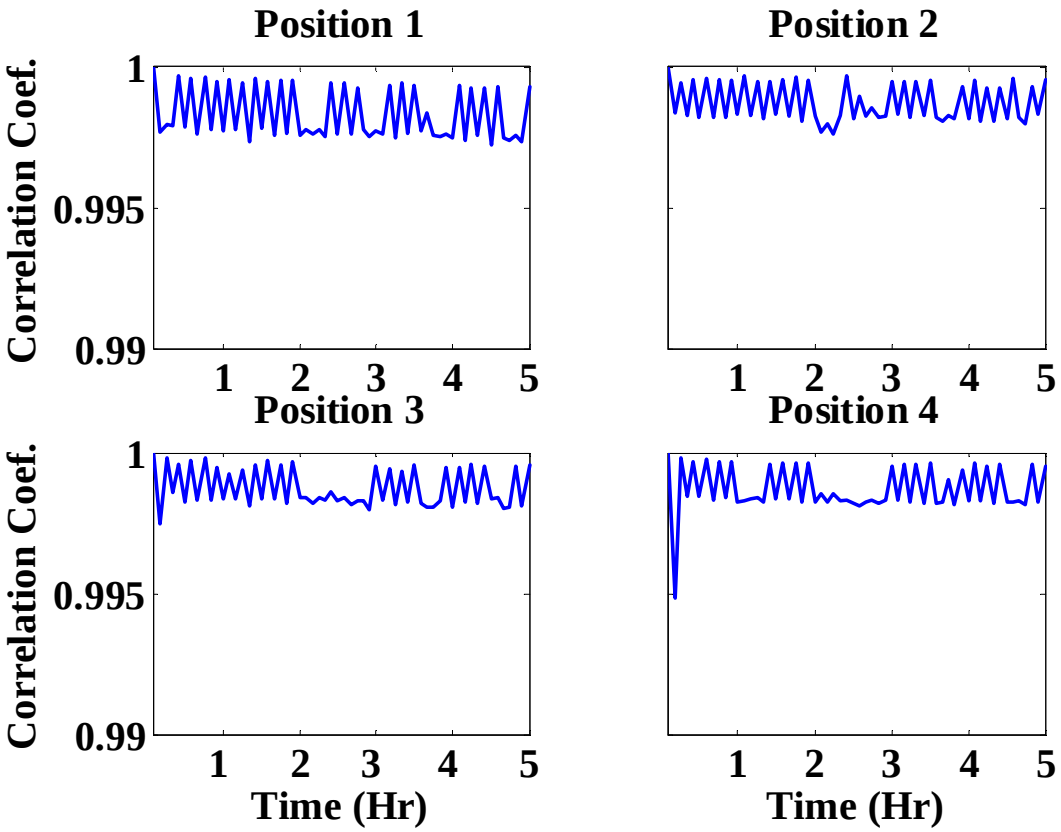

Figure 17: Channel stability test results: Correlation coefficient of the 60 measurements in a duration of 5 hours for four receive antenna locations. The correlation coefficients are larger than 0.995, indicating high repeatability of our measurement results.

The next question is: Is the performance of virtual antenna array, which is immune to the mutual coupling effect, close to the performance of real antenna array? Next, we will verify the performance of virtual antenna array in terms of MIMO channel capacity.

3.4 Validation of Virtual Antenna Array

In this dissertation, we use extensively the measured capacities to evaluate the performance of MIMO channels. Since our measurement system is based on virtual antenna array scenario, which is immune to the mutual coupling effect, one might be suspicious about whether the performance of virtual antenna arrays is close to the real MIMO systems with real antenna arrays. To answer this question, we compare the performance of real antenna array and virtual antenna array in this section. The measurement was conducted in SARL. The real antenna array is accomplished by adding a multi-channel controller HP85330 to the measurement system. The transmit antennas are connected to the transmit source alternately by the solid-switch controlled by HP85330. Likewise, the receive antennas are alternately connected to the microwave receivers. In the measurement, both the transmitter and receiver are (3×5) URAs. For the virtual antenna array, the (3×5) URA is emulated by moving single antenna to each location at both sites. As for the real antenna array, the URA is formulated by moving the 3-element real antenna array to 5 locations along the y-axis. The measured frequency response comprises 51 frequency samples over a bandwidth of 500 MHz centered at 5.8 GHz; therefore, we may extract totally 5×5×51=1275 realizations of narrowband (3,3) MIMO channel matrices. These matrices can then be used to obtain the CDF of MIMO channel capacity. In the experiment, each measurement of (3,3) MIMO channel matrix takes about 7 *ms* with the real antenna arrays, while the virtual antenna arrays need about 16 minutes to finish the entire measurement. Because of the limitation of antenna size, only the element spacings of 2 λ and 3 λ are considered.

(a)

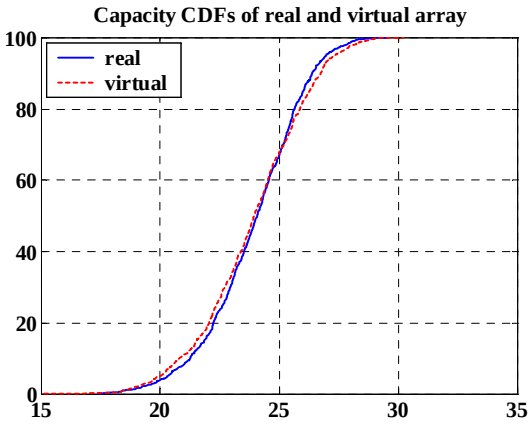

(b)

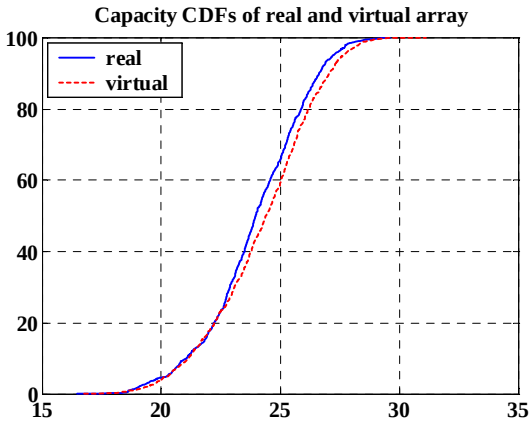

(c)

Figure 18: Comparison of a real and a virtual antenna array. The LOS component is available. The array geometry is shown in (a), and the antenna spacings are (b) 2 λ and (c) 3 λ.

First, we consider the channels with LOS. The transmitter and receiver locations are at T1 and R1 respectively in Figure 16. Figure 18(a) illustrates the array geometry and relative position of the Tx and Rx, which are on the endfire sides of each other. Figures 18(b) and (c) shows CDFs of the measured capacity with the spacings of 2λ and 3λ, respectively. In both cases, the performance of real and virtual antenna arrays are very close. The difference is less than 1 bit/sec/Hz.

Figure 19 shows the measurement results when the transmit and the receive arrays are orthogonal to each other. In this case, the performances of virtual and real antenna array are also very close.

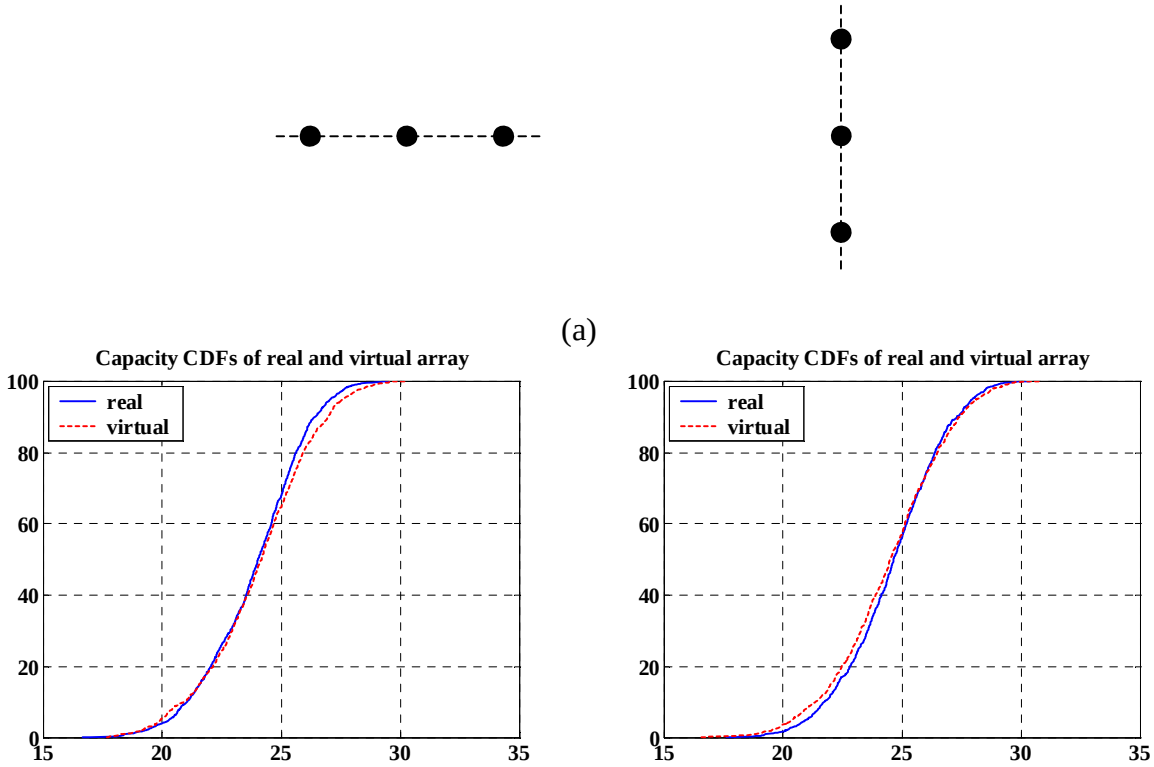

Figure 19: Comparison of real and virtual antenna array. The LOS component is available. The array geometry is shown in (a), and the antenna spacings are (b) 2 λ and (c) 3 λ.

When the arrays are on the broadside of each other, as shown in Figure 20(a), the difference is larger than when the antenna spacing is 2λ, but the discrepancy is still less than 1 bit/sec/Hz.

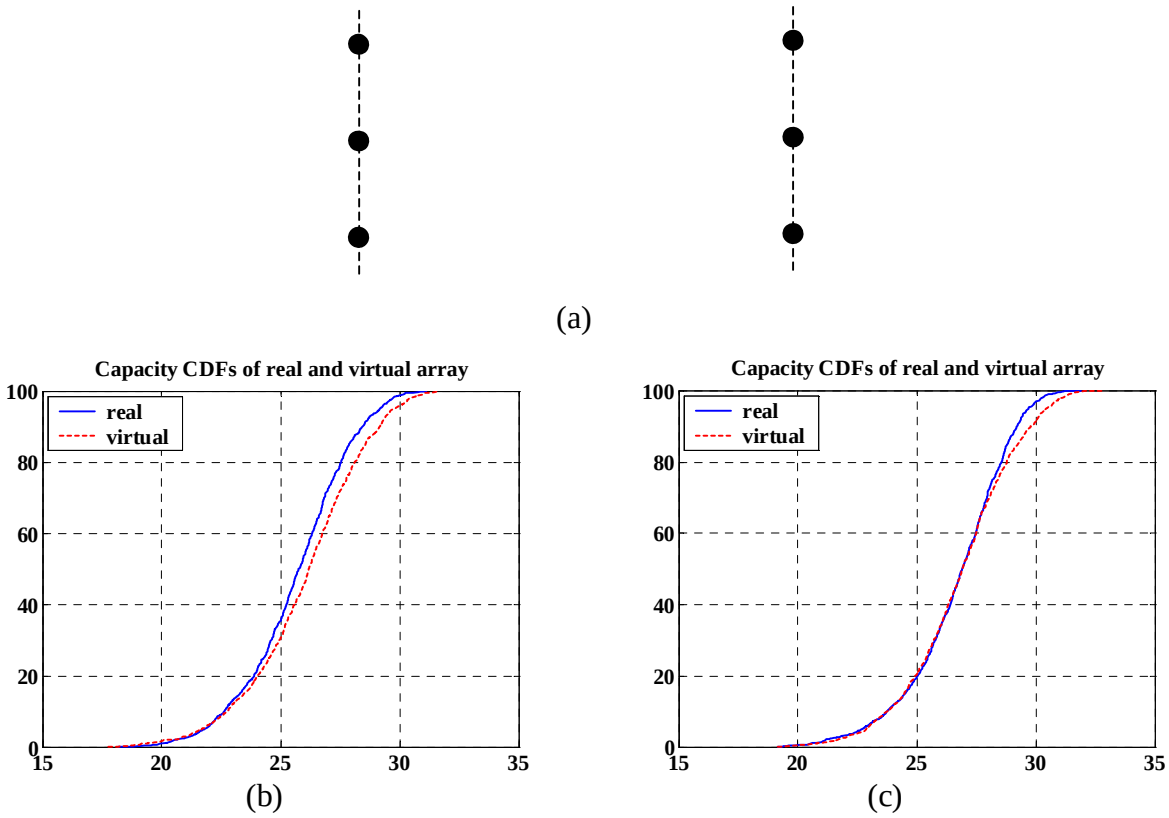

Figure 20: Comparison of real and virtual antenna array. The LOS component is available. The array geometry is shown in (a), and the antenna spacings are (b) 2 λ and (c) 3 λ.

Next, we consider the channels where the LOS component is obstructed. The locations of transmit and receive arrays are at T3 and R4 of Figure 16. Because the capacity without LOS is less sensitive to the orientation of the arrays, we consider only the case where the transmit and receive arrays are on the broadside of each other. The measurement results in Figure 21 indicate that the difference of real and virtual antenna array is still less than 1 bit/sec/Hz. These results tell us that the conclusions based on the measurements with the virtual antenna array are valid and can be used to evaluate the performance of real MIMO systems.

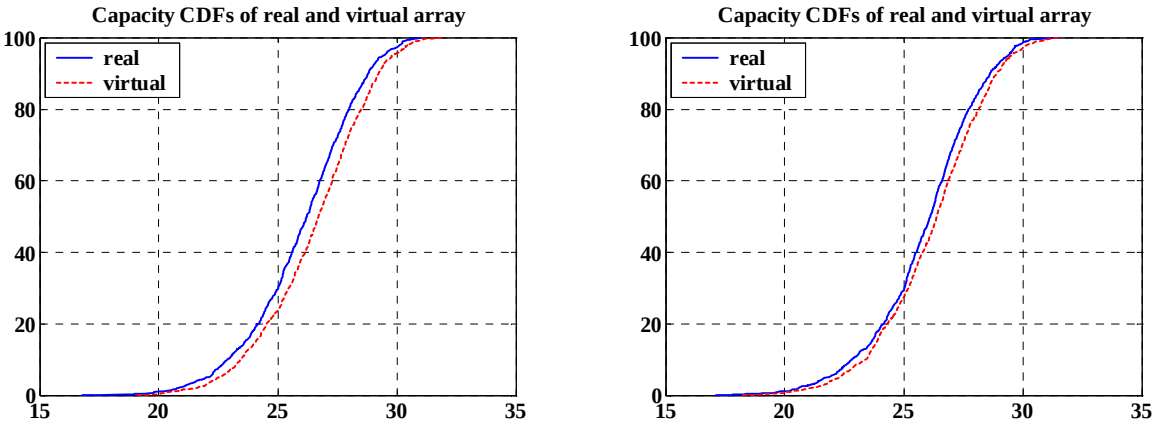

(a) (b)

Figure 21: Comparison of real and virtual antenna array. The LOS component is not available. The antenna spacings are (a) 2 λ and (b) 3 λ.

3.5 Chapter Summary

In this chapter, we introduced our MIMO channel sounding system, which is based on the virtual antenna array infrastructure. The measurement procedure, including the acquisition of raw data and the following back-to-back calibration to remove the unwanted system response, was described in detail. Two preliminary experiments were conducted in the SARL to test the channel stability and determine the difference between the virtual and real antenna arrays. The measurement results demonstrated very high repeatability, indicating that the indoor channel is stationary and suitable for the virtual antenna array. Moreover, the difference of the measured MIMO channel capacities using the virtual and the real antenna array is negligible. Therefore, the measured data obtained by our measurement system is reliable and appropriate to evaluate the properties and performance of MIMO channels.

Chapter 4

Detection of Number of Sources

In Chapter 3, we introduced our 3D MIMO channel sounding system and the measurement procedure. In the next chapter we address how the measured data are used to estimate MIMO channel parameters, including the complex gain, delay, DOA, and DOD. However, before we can estimate these path parameters, we need to determine the number of paths. This is an example of the general "detection of number of sources" problem, where a path is treated like a source. The number of sources is assumed to be known in many path parameter estimation algorithms, such as the MUSIC and ESPRIT algorithms. However, this value is usually unknown in reality and needs to be detected before the parameter estimation is performed. In this chapter, we propose two detection algorithms. One is based on the residual estimation error (REE), and the other is based on the variance of the transformed rotational submatrix (VTRS). These two algorithms have shown to be more robust than some traditional methods, thus are more suitable for our application.

4.1 REE Number Detection Method

4.1.1 Description of the REE Method

In this section, we propose a new method for the detection of the number of paths according to the residual estimation error. Like the DEE detection algorithm described in Section 2.4.2, the REE algorithm falls into the data-based group of the combined detection-estimation category defined in Section 2.4. As mentioned in Chapter 2, the DEE detection algorithm determines the number of sources by searching for the local minimum of the data estimation error [57]. However, there are multiple local minima, and the selection of local minimum is subjective. The REE algorithm eliminates the requirement of this subjective decision by using part of the sensor data to recover the signal and by using the complementary part of the data to calculate the residual error of the estimate. Through this approach, the number is determined by the global minimum of REE. The concept is similar to the cross-validation method [77,78], which is commonly applied to neural networks to select the model and classifier. Next we describe the details of the REE method.

The general signal model for multiple source localization is

$$\mathbf{Y} = \mathbf{A}\boldsymbol{s} + \boldsymbol{n}, \tag{80}$$

where $\mathbf{Y}$ and $\boldsymbol{n}$, both $\in \mathbf{C}_{N\times 1}$, are the received signal and noise of N sensors, respectively, $\boldsymbol{s} \in \mathbf{C}_{L\times 1}$ are the signal sources, and $\mathbf{A} \in \mathbf{C}_{N\times L}$ is the steering matrix. N and L denote the number of sensors and the number of sources, respectively. $\mathbf{A} = [\mathbf{a}_1\, \mathbf{a}_2\, \ldots\, \mathbf{a}_L]$, where $\mathbf{a}_i$ is the steering vector corresponding to the i^{th} signal source.

As shown in Figure 22, the vector of received array signals $\mathbf{Y}$ can be partitioned into two complementary subarrays, $\mathbf{Y}_1$ and $\overline{\mathbf{Y}_1}$. $\mathbf{A}_1$ and $\overline{\mathbf{A}_1}$, the corresponding steering matrices of $\mathbf{Y}_1$ and $\overline{\mathbf{Y}_1}$, are complementary subblocks of $\mathbf{A}$.

Using the MUSIC or ESPRIT algorithms, the parameter of interest can be estimated based on some assumed number of signals *k*. Like the cross-validation method, which trains the neural network by a subset of samples and uses the other samples to evaluate the accuracy of the trained network, we recover the source signal source $\hat{\boldsymbol{s}}$ by the subset $\mathbf{Y}_1$ and $\widehat{\mathbf{A}}_1$, and reconstruct the array signals of the other subset $\widehat{\overline{\mathbf{Y}}}_1$. The recovery of $\hat{\boldsymbol{s}}$ and the reconstruction of $\widehat{\overline{\mathbf{Y}}}_1$ are derived by

$$\hat{\boldsymbol{s}} = (\widehat{\mathbf{A}}_1^{\dagger}\widehat{\mathbf{A}}_1)^{-1}\widehat{\mathbf{A}}_1^{\dagger}\mathbf{Y}_1, \tag{81}$$

and

$$\widehat{\overline{\mathbf{Y}}}_1 = \widehat{\overline{\mathbf{A}}}_1\hat{\boldsymbol{s}}, \tag{82}$$

respectively, where $\widehat{\mathbf{A}}_1$ and $\widehat{\overline{\mathbf{A}}}_1$ are the estimates of the steering matrices $\mathbf{A}_1$ and $\overline{\mathbf{A}_1}$ based on the estimated parameters. All the subsets of $\mathbf{Y}$ can be used to recover the signal, but one should be careful in selecting the size of the subset in order to obtain an accurate recovery of $\hat{\boldsymbol{s}}$. Given the subsets of $\mathbf{Y}$, the residual estimation error (REE), assuming the number of sources is *k*, is defined as

$$REE(k) = \sum_{i=1}^{M} \frac{\left\| \widehat{\overline{\mathbf{Y}_i}} - \overline{\mathbf{Y}_i} \right\|_2}{\left\| \overline{\mathbf{Y}_i} \right\|_2}, \tag{83}$$

where *M* is the number of subsets. The number of sources can be determined by searching for the *k* that minimizes the REE.

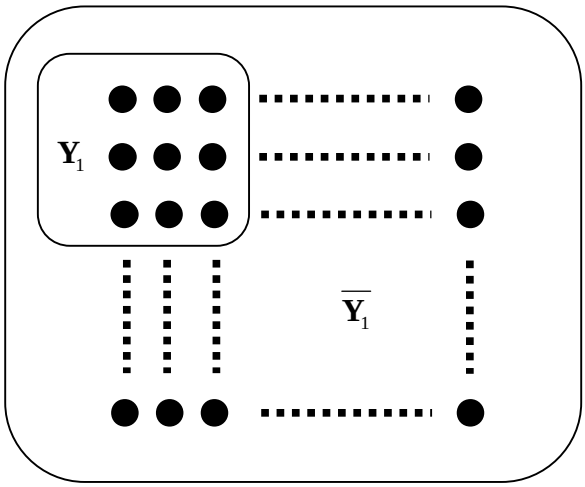

Figure 22: The partition of the arrays in REE method. $\mathbf{Y}$ is the of the received array signals; $\mathbf{Y}_1$ is part of $\mathbf{Y}$ and used to recover the signal $\boldsymbol{s}$; $\overline{\mathbf{Y}_1}$ is used to calculate the error of the reconstructed signal.

This method also works in noisy environments. The reason is that when the number is overestimated, the additional degrees of freedom which attempt to model the noise samples of $\mathbf{Y}_1$ in (81) are not suitable for the noise samples in its complementary set $\overline{\mathbf{Y}_1}$ and will increase the error in the reconstruction of $\overline{\mathbf{Y}_1}$ using (82) .

4.1.2 Simulation Result

Next, we compare the performance of DEE and REE using simulation. In the simulation, the array is a uniform linear array, and the DOAs of four uncorrelated signals are 5°, 30°, 40°, and 60°, respectively. The SNR is 20 dB. As shown in Figure 23, the minimum of the REE detection function corresponds to the correct number of sources, while the DEE fails because the minimum occurs when the number is 15.

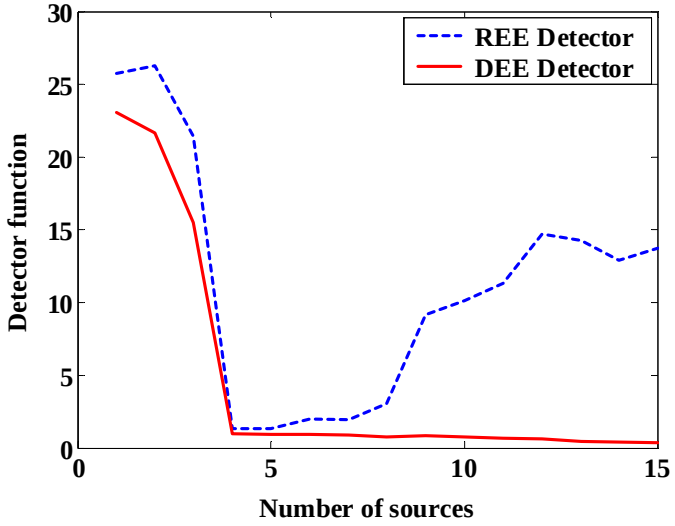

Figure 23: The comparison of DEE and REE. The REE successfully detects the number of sources, while the DEE overestimates the number of sources.

Although REE algorithm appears to be a robust method, its computational complexity is high, especially for the arrays with large array size. In the following section, we propose a robust detection method with low computational complexity.

4.2 VTRS Number Detection Method

4.2.1 Description of the VTRS Method

In this section, we describe the second detection algorithm, which belongs to the eigenvector-based group in Category I defined in Section 2.4. This method exploits the property of the variance of the transformed rotational submatrix (VTRS). The rotational matrix is critical to the ESPRIT estimator; therefore, when ESPRIT is being used for parameter estimation, the VTRS method requires only a small additional amount of computation. Like ESPRIT, the VTRS number detector is computationally efficient and applicable to arbitrary subarray geometries. The only requirement is that the two

subarrays must be identical. Other than that, the sensors in each subarray are not required to be identical. Also like ESPRIT, the VTRS number detector is robust to non-identical sensor gains and imperfect sensor locations. Moreover, since the VTRS method belongs to pure detection category, it also has the feature of low computational complexity.

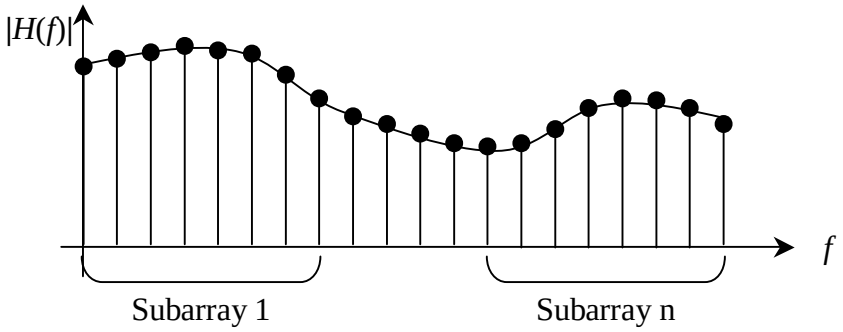

Figure 24: Sensor gain variations of the array elements on the frequency domain. The eigenspace of Subarray 1 is different from that of Subarray n. After the smoothing, the derived eigenspace is distorted.

The VTRS number detection algorithm is robust against two kinds of measurement distortions when the smoothing technique is necessary. Smoothing is a technique that derives the correlation matrix through the combination of the correlation matrices of all subarrays. As mentioned in Section 2.3.5, the purposes of smoothing are twofold: (1) decorrelate the coherent signal sources and (2) increase the number of snapshots.

The first kind of measurement distortion results from gain variations of the array elements. For example, in delay estimation the array elements are the frequency samples. If the frequency response of the antenna is not constant, as shown in Figure 24, the eigenvectors obtained from the correlation matrix of one subarray are different from those of the other subarrays. In consequence, the derived eigenspace is distorted after smoothing is applied. The VTRS algorithm is less sensitive to the distortion because it

determines the number of sources by exploiting the relationship between the eigenspaces of two subarrays instead of using the entire eigenspace. This kind of distortion also happens in angle estimation when the antenna element gains are different, and in Doppler shift estimation when the sensor has a time-varying response.

The second kind of measurement distortion is caused by variations in the spacing of the array elements. Antenna location disturbance, caused by external force or mechanical fault, is the primary reason for the varying element spacing. As shown in the Figure 25, the original element spacing is *d*, but the second and third antennas are shifted by Δ_1 and Δ_2, respectively. Because of the variations in the element spacing, the eigenspaces of the subarrays are also different, and the derived eigenspace is distorted after smoothing.

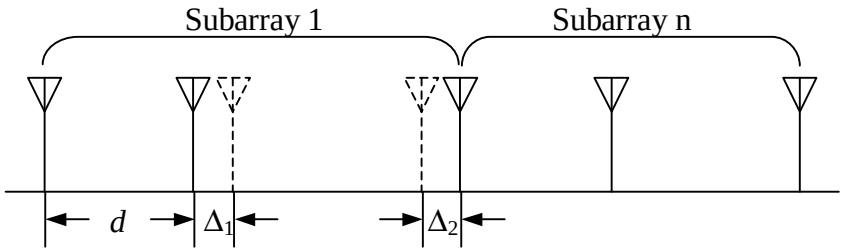

Figure 25: Varying antenna spacing of the array elements on the spatial domain. Eigenspace distortion also results from the varying eigenspace of the subarrays.

The correlation matrix of the received signal is

$$\mathbf{R} = \mathbf{A}\mathbf{R}_{ss}\mathbf{A}^{\dagger} + \mathbf{R}_{\mathbf{n}}, \tag{84}$$

where $\mathbf{R}_{ss}$ is the signal correlation matrix, $\mathbf{R}_{\mathbf{n}}$ is the noise covariance matrix. The ESPRIT algorithm exploits the rotational invariance property between two identical subarrays to derive the estimates. Accordingly, the subarray geometry can be arbitrary, and the sensors of each subarray can have different gains. Here, we assume the first subarray is derived from the first *N*-1 sensors, and the second subarray is composed of the final *N*-1

sensors. The results, of course, also apply to the case where the two subarrays are not overlapped.

The steering matrices of the first and second subarrays are $\mathbf{A_x}$ and $\mathbf{A_y}$, respectively. Accordingly,

$$\mathbf{A_z} = \begin{bmatrix} \mathbf{A_x} \\ \mathbf{A_y} \end{bmatrix} = \begin{bmatrix} \mathbf{A_x} \\ \mathbf{A_x \Phi} \end{bmatrix}, \tag{85}$$

where $\mathbf{\Phi} = diag\left\{ e^{j\beta_2} \quad e^{j\beta_2} \quad \cdots \quad e^{j\beta_L} \right\}$ is the rotational matrix. The definition of β depends on the parameter of interest. The eigenvectors of $\mathbf{R}$ are

$$\mathbf{E} = \begin{bmatrix} \mathbf{e_1} & \mathbf{e_2} & \cdots & \mathbf{e}_N \end{bmatrix} = \begin{bmatrix} \mathbf{E_s} & \mathbf{E_n} \end{bmatrix}, \tag{86}$$

where

$$\mathbf{E_s} = \begin{bmatrix} \mathbf{e_1} & \mathbf{e_2} & \cdots & \mathbf{e}_L \end{bmatrix}, \tag{87}$$

and

$$\mathbf{E_n} = \begin{bmatrix} \mathbf{e}_{L+1} & \mathbf{e}_{L+2} & \cdots & \mathbf{e}_N \end{bmatrix}. \tag{88}$$

The columns of $\mathbf{E_s}$, which are the eigenvectors corresponding to the L largest eigenvalues, span the signal subspace, while the columns of $\mathbf{E_n}$ span the noise subspace. Since both $\mathbf{E_s}$ and $\mathbf{A}$ span the same subspace, there exists a non-singular matrix $\mathbf{T}$, such that

$$\mathbf{E_s} = \mathbf{AT}. \tag{89}$$

Applying (89) to (85), we obtain

$$\mathbf{A_z T} = \begin{bmatrix} \mathbf{A_x T} \\ \mathbf{A_y T} \end{bmatrix} = \begin{bmatrix} \mathbf{A_x T} \\ \mathbf{A_x \Phi T} \end{bmatrix} = \begin{bmatrix} \mathbf{E_{sx}} \\ \mathbf{E_{sy}} \end{bmatrix} = \begin{bmatrix} \mathbf{E_{sx}} \\ \mathbf{E_{sx} \Psi_s} \end{bmatrix}, \tag{90}$$

where $\mathbf{\Psi_s} = \mathbf{T^{-1} \Phi T}$ is the transformed rotational matrix of the signals, $\mathbf{E_{sx}}$ and $\mathbf{E_{sy}} \in \mathbf{C}_{(N-1)\times L}$ are the signal eigenvectors of two subarrays. Suppose $\mathbf{E_x}$ and $\mathbf{E_y} \in \mathbf{C}_{(N-1)\times N}$ are the first N-1 rows and last N-1 rows of $\mathbf{E}$, respectively, and assume the noise is not present.

Notice that the eigenvectors $\mathbf{E_n}$ are still nonzero in a noiseless condition even though the eigenvalues are zero. Then

$$\mathbf{E_y} = \begin{bmatrix} \mathbf{E_{sy}} & \mathbf{E_{ny}} \end{bmatrix} = \begin{bmatrix} \mathbf{E_{sx}} & \mathbf{E_{nx}} \end{bmatrix} \begin{bmatrix} \mathbf{\Psi_s} & \mathbf{\Gamma}_1 \\ \mathbf{0} & \mathbf{\Gamma}_2 \end{bmatrix} = \mathbf{E_x \Psi}, \tag{91}$$

where $\mathbf{\Gamma}_1 \in \mathbf{C}_{L\times(N\text{-}L)}$, $\mathbf{\Gamma}_2 \in \mathbf{C}_{(N\text{-}L\text{-}1)\times(N\text{-}L)}$, $\mathbf{E_x} = \begin{bmatrix} \mathbf{E_{sx}} & \mathbf{E_{nx}} \end{bmatrix}$, and

$$\mathbf{\Psi} = \begin{bmatrix} \mathbf{\Psi_s} & \mathbf{\Gamma}_1 \\ \mathbf{0} & \mathbf{\Gamma}_2 \end{bmatrix}. \tag{92}$$

It is the zero submatrix of $\mathbf{\Psi}$ that is the basis of the VTRS algorithm.

Define $\mathbf{\Delta}_k$ as a submatrix of $\mathbf{\Psi}$:

$$\mathbf{\Delta}_k = \begin{bmatrix} \psi_{k+1,1} & \psi_{k+1,2} & \cdots & \psi_{k+1,k} \\ \psi_{k+2,1} & \psi_{k+2,2} & \cdots & \psi_{k+2,k} \\ \vdots & \vdots & \ddots & \vdots \\ \psi_{N-1,1} & \psi_{N-1,2} & \cdots & \psi_{N-1,k} \end{bmatrix}. \tag{93}$$

When $k = L$, $\mathbf{\Delta}_k$, submatrix of the transformed rotational matrix $\mathbf{\Psi}$, is $\mathbf{0}$. When $k \neq L$, $\mathbf{\Delta}_k$ contains nonzero components. Therefore, we may select the number that minimizes the variance $\rho(k)$ of the components of $\mathbf{\Delta}_k$ as the detected number of sources when the noise is present, i.e.

$$\hat{L} = \min_k \rho(k) = \frac{\|\mathbf{\Delta}_k\|^2}{(N-k-1)k}, \qquad k = 1,\ 2,\ \cdots,\ N\text{-}2, \tag{94}$$

where $\|\cdot\|$ is the Frobenius norm. When the noise is present, the estimate of $\mathbf{\Psi}$ can be solved based on least square (LS) or total least square (TLS) criterion. Notice that $\|\mathbf{\Delta}_{k+1}\|^2$ can be derived from $\|\mathbf{\Delta}_k\|^2$ and reduce the computational cost by using

$$\|\mathbf{\Delta}_{k+1}\|^2 = \|\mathbf{\Delta}_k\|^2 - \|\text{first row of } \mathbf{\Delta}_k\|^2 + \|\text{last column of } \mathbf{\Delta}_{k+1}\|^2. \tag{95}$$

The computational cost can be further reduced by replacing $\mathbf{E_x}$ and $\mathbf{E_y}$ by the first L_T columns of $\mathbf{E_x}$ and $\mathbf{E_y}$ provided the threshold L_T is larger than L.

As ESPRIT can be generalized to multi-dimensional ESPRIT [49], the VTRS method can be easily generalized to multi-dimensional detection by summing the calculated variances of each dimension. Given the number of dimensions M, the number of sources is detected by

$$\hat{L} = \min_k \sum_{D=1}^{M} \rho_D(k) . \tag{96}$$

The steps of the VTRS method are summarized below.

Step 1: Calculate the correlation matrix **R**.

Step 2: Derive the eigenvectors **E** of **R**.

Step 3: Solve $\mathbf{E_y} = \mathbf{E_x}\mathbf{\Psi}$ based on LS or TLS criterion.

Step 4: Calculate (94) or (96) efficiently by (95) and obtain the detected number of sources.

Since *Steps 1* and *2* are originally required for parameter estimation, the additional time used for the VTRS detector is for *Steps 3* and *4*. However, if the first $\hat{L}\times\hat{L}$ submatrix of estimated $\mathbf{\Psi}$ in *Step* 3 is used as the estimate of $\mathbf{\Psi_s}$, then only *Step 4* is dedicated to the detector, which turns out to be a one-step detector.

The performance of the VTRS algorithm can be further enhanced using the following method. In (92), $\mathbf{\Psi}$ is derived from the entire set of eigenvectors. However, using a reduced number of eigenvectors can produce reduced transformed rotational matrix, which also contains the zero submatrix provided that the number of eigenvectors is larger than the real number of signals. This reduced matrix can also be used to detect

the number of signals based on VTRS criterion. Therefore, using multiple reduced rotational matrices, we can obtain multiple detection results. The final decision can be derived based on the majority of all detectors.

4.2.2 Simulation Results

Three sets of simulations are provided to demonstrate the performance of the VTRS detector. In Set 1, we compare VTRS and MDL in a benign scenario, specifically, using the signals with close delays when the frequency response of the antenna is flat. Set 2 shows the robustness of VTRS detector by using a sensor with a non-flat frequency response. Set 3 demonstrates the robustness of VTRS against non-uniform element spacing.

Simulation 1: Flat frequency response

In this simulation set, the antenna has a flat frequency response. The delays can be estimated from the frequency response [50]. In delay estimation, only one antenna is used, and the snapshots are extracted from the frequency samples by smoothing technology. Three multipath signals impinge the antenna at delays 3.3*ns*, 7.4*ns*, and 11.8*ns*. The frequency separation between adjacent samples of the frequency response is 25 MHz. The smoothing subarray size is 20, i.e. there are 20 frequency samples in each subarray. In the simulation there are totally 120 samples in the entire frequency response, so 101 snapshots can be obtained. In Figure 26, we compare MDL and VTRS in terms of detection error rate. The detection error rate is an average over 500 trials of simulations. We observe that the two methods yield similar trends in the error rate detection, while VTRS outperforms MDL slightly at high SNR.

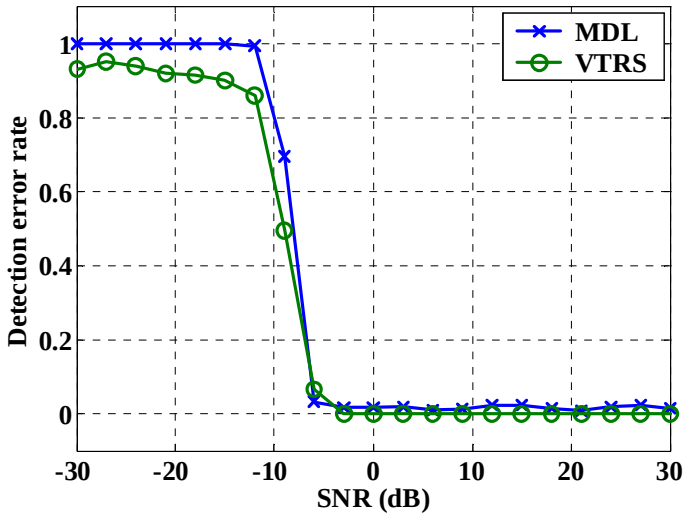

Figure 26: Results of Simulation Set 1: The performance of MDL and VTRS with 3 sources and flat frequency response.

Simulation 2: Non-flat frequency response

We next consider the performances of MDL and VTRS methods when the frequency response of the antenna is not flat, which is usually true, especially when the bandwidth is wide. In this case, the signal subspaces of all smoothing subarrays are no longer identical. As shown in Figure 27(a), the non-flat frequency response is generated by

$$G(n) = 1 + 0.3\sin(0.0025\pi n) + 0.03\sin(0.8\pi n),$$

where n =1, 2, …, 120 is the index of 120 frequency samples.

As expected, MDL fails at low and high SNR. The MDL fails at higher SNR because it is more sensitive to the signal subspace distortion. On the other hand, the VTRS shows the robustness in this condition at high SNR. Although the signal subspace is distorted due to the non-flat frequency response, the rotational matrix between two subarrays still provides accurate information for either detection or estimation.

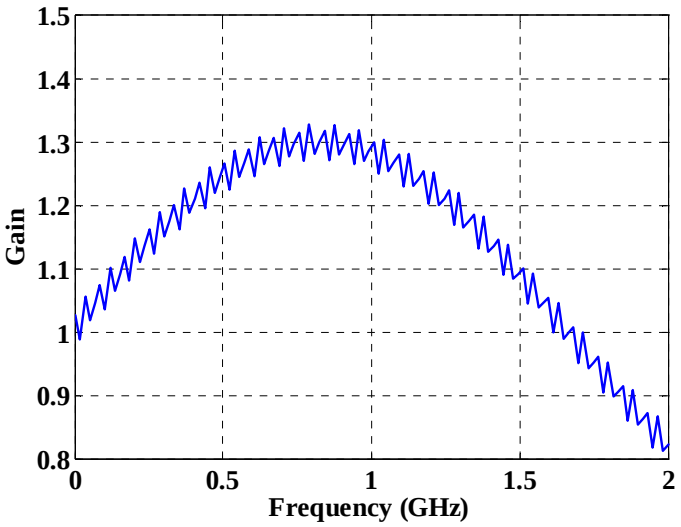

(a) Non-flat frequency response

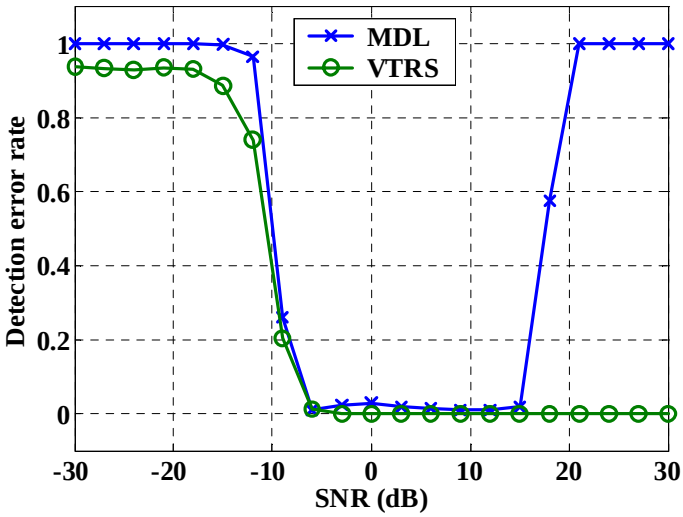

(b) Performance of MDL and VTRS

Figure 27: Results of Simulation Set 2: (a) Non-flat frequency response. (b) Performance of MDL and VTRS.

Simulation 3: *Non-uniform element spacing*

In this simulation, three narrowband signal sources centered at 5.8 GHz impinge the antenna array from the angles 5.5°, 13.2°, and 37.4°, respectively. The nominal array is a 16-element ULA with element spacing 0.5λ, and the subarray size is 8. We assume that the antenna locations are disturbed because of some external force. The disturbance

of each antenna location is a normal distributed random variable with zero mean, and the deviation is 5% of the element spacing. The simulation result is similar to that of non-flat frequency response. As shown in Figure 28, the MDL algorithm is sensitive to the disturbance even though the deviation is only 5%. Although not shown here, we observed that the SNR range where MDL successfully detects the number of sources decreases with the increase of location deviation.

Although Doppler shift is not included in the simulations, it is reasonable to deduce that the robustness is also a feature of Doppler shift estimation when the sensor response changes gradually with time.

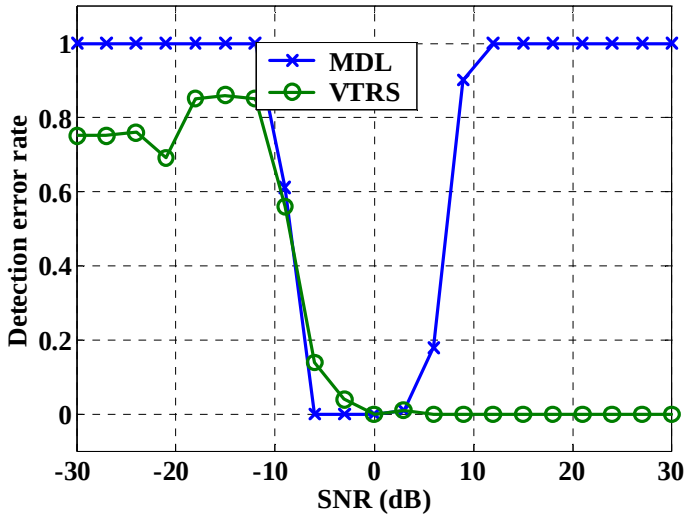

Figure 28: Results of Simulation Set 3: The relative performances of MDL and VTRS for imperfect antenna locations.

4.2.3 Validation Using Measured Data

Although some algorithms may work perfectly in simulation, their performances can be significantly reduced or even completely fail when they are applied to real channels. More or less, there exist some difference between the simulation and the real

world since it is impossible to include all factors in the simulation. Therefore, it is important to validate the algorithms using measured data to realize the robustness of the algorithms before applying them to practical applications. In this section, we compare the performances of VTRS and MDL detectors using the measured data obtained from the experiments in SARL at the Georgia Institute of Technology. The measurement was conducted with our 3D MIMO measurement testbed. Details of the testbed, the settings of the measurement, the parameter estimation, and the reconstruction of the channel matrix, may be found in Chapter 2. The measured data is the MIMO channel matrix, where both the transmitter and the receiver are 4×4×3 rectangular arrays with antenna spacing 0.48λ. The LOS is available between the transmitter and the receiver. The frequency response of the link between each pair of transmit-receive antennas comprises 401 frequency samples over a span of 500 MHz. With the measured data, one can estimate the parameters of multipath, including complex gain, delay, DOA, and DOD. A straightforward way to realize the accuracy of the estimation is to reconstruct the channel matrix based on the estimated parameters and compare the difference in capacities of the reconstructed and the measured channel matrix.

In the estimation, the delays are first obtained by the unitary ESPRIT algorithm, and the DOA and DOD are jointly estimated at each delay time. The subarray sizes of transmit and receive antenna arrays are 2×2×2. Therefore, the maximum number of sources that can be estimated by multi-dimensional ESPRIT algorithm is $2^5\times(2-1)-1=31$. Figure 29 shows the eigenvalue distribution and the detector metrics of VTRS and MDL for the joint estimation of DOA and DOD at delay time 8.87 *ns*, which is the time when the LOS path arrives at the receiver. As shown in Figure 29, the first eigenvalue, which

corresponds to the LOS path, is at least 30 dB larger than the other eigenvalues. The LOS path is supposed to be the only path at this delay. However, the MDL metric decreases monotonically with the number of sources and the detected number of sources is the maximum value 31. For the VTRS detector, the metric arises abruptly when the number of sources is increased from 1 to 2, and continues to increase gradually with more sources. Therefore, the VTRS detector successfully indicates the correct number of paths.

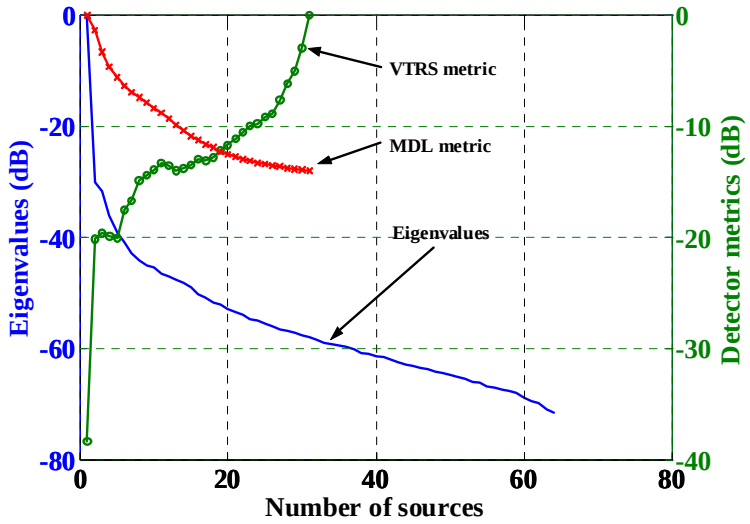

Figure 29: The eigenvalue distribution and detector metrics in the joint estimation of DOA and DOD at delay time 8.87 *ns*.

Next, we compare the directly measured and the reconstructed complex channel impulse responses using MDL and VTRS detectors. We note that channel frequency response phase is particularly sensitive to the path parameters delay, DOA and DOD. Figure 30 shows the normalized mean squared error $\varepsilon(f)$ of the magnitude of the reconstructed impulse responses, i.e.

$$\varepsilon(f) = E\left\{ \frac{\left|Y(f) - \hat{Y}(f)\right|^2}{\frac{1}{B}\int_{f_c - B/2}^{f_c + B/2} \left|Y(f)\right|^2 df} \right\}, \tag{97}$$

where $Y(f)$ and $\hat{Y}(f)$ are the complex frequency responses of the measured and reconstructed channels, respectively. B and f_c denote the bandwidth and the center frequency. The abundant transmit/receive antenna pairs provide the outcomes for the calculation of the expectation value. As shown in Figure 30, the mean squared error of MDL is larger than the error of VTRS. The estimation error resulted from the inaccurate detection of number of signals will lead to wrong conclusions in further analyses, such as the estimation of channel capacity and the derivation of the statistics of DOA and DOD. The VTRS detector demonstrates the advantages of robustness and accuracy over the MDL detector in the practical application.

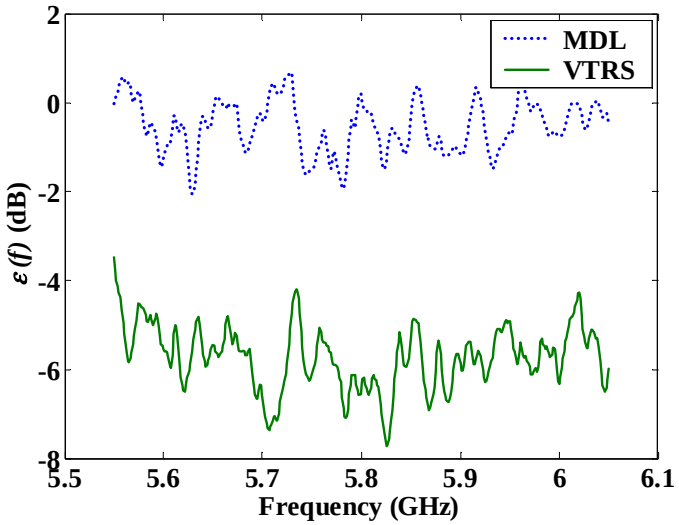

Figure 30: The mean square error of the amplitude of the reconstructed channel frequency responses.

4.3 Chapter Summary

We presented two novel number-of-sources detection methods, REE and VTRS algorithms. A subjective threshold is not required for both methods. The VTRS number detector has the features of high accuracy, robustness, and applicability to arbitrary arrays

and arbitrary noise covariance matrices. It also has the advantage of low computational complexity, which makes the VTRS detector a good candidate for practical applications that need real-time or adaptive high-resolution estimation. Simulation results showed that this new detection scheme is very robust against the subspace distortion resulting from non-identical sensor gains and imperfect antenna locations when the spatial smoothing is applied. Estimation results based on a measured wireless channel in the indoor environment have validated the robustness advantage of VTRS detector over the MDL detector.

Chapter 5

Parameter Estimation Results

In Chapter 2, we introduced the sequential estimation and joint estimation schemes based on the ESPRIT algorithm. The parameters of interest for MIMO channels include the complex gain, delay, DOA, and DOD of each path of propagation. In this chapter, we will compare the performances of variants of these schemes when they are applied to MIMO channel parameter estimation. These versions include the sequential estimation, delay estimation followed by the joint DOA-DOD estimation, inverse Fast Fourier Transform (IFFT) followed by sequential estimation, and IFFT followed by joint estimation of DOA and DOD. Because the joint delay-DOA-DOD estimation involves intensive computations, this scenario is not considered in the dissertation.

5.1 Experiment Environments And Settings

The experiments for the parameter estimation were carried out in the SARL. In each measurement, two separate measurements were conducted; one for the path parameter estimation, and the other for direct capacity measurement. In the path parameter estimation measurement, the arrays at both ends are (4×4×3) uniform cubicle arrays. The measured data is the frequency response containing 401 frequency samples over 5.55 – 6.05 GHz. After transferring to the time domain using the IFFT, the temporal resolution of the impulse response is 2 *ns*, and the entire observation time is 800 *n*s.

Spatial smoothing is achieved by averaging the correlation matrices derived from the subarrays. The subarray sizes used in all estimation methods are (3×2×2) and (3×2×2), for DOA and DOD, respectively. The antenna spacing varies for different experiments and will be mentioned in the description of each experiment. The measurement settings for the path parameter estimation are summarized in Table 3.

Table 3: Settings for path parameter estimation.

Place:	Smart Antenna Laboratory
Frequency:	5.55 – 6.05 GHz
Frequency samples:	401 pts
Transmitter array:	(4×4×3) Cubical array
Receiver array:	(4×4×3) Cubical array
Antenna spacing:	0.25 or 0.48λ

As for the direct capacity measurement, the Tx array is a 5-element ULA, while the Rx array is a (5×5) URA, as shown in Figure 31. The measurements are taken with five different element spacing (0.25, 0.5, 1, 2, 3λ) at each location. To obtain independent outcomes for the flat-fading capacity CDF, the frequency spacing is set to 10 MHz. Our calculations show that with a 10 MHz separation, the correlation coefficient between adjacent frequency samples is less than 0.4. Accordingly, there are 51 samples over 500 MHz bandwidth. To get spatial samples of capacity, subarrays with different array shapes and spacings are extracted from the 5-element ULA and (5×5) URA, as shown in Figure 31. With this arrangement, we may extract a total of 1632 outcomes of MIMO channel matrices when the (Tx, Rx) subarray setting is the (4,2×2) ULA-URA combination, and 1020 outcomes when the setting is (4,4) ULA-ULA for capacity CDF calculation. When the array arrangement is ULA-ULA, the Tx and Rx could be either orthogonal or parallel;

accordingly, we may measure the channel capacities of three different array geometries, i.e. parallel ULAs, orthogonal ULAs, and ULA-URA.

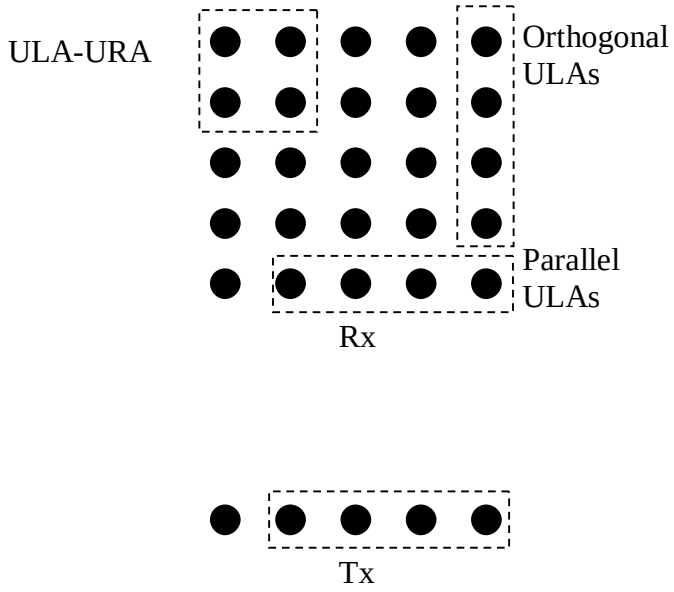

Figure 31: Extraction of three different subarrays: (1) Parallel ULAs, (2) Orthogonal ULAs, and (3) ULA-URA.

The experiment settings for the capacity measurement are summarized in Table 4.

Table 4: Settings for direct capacity measurement

Place:	Smart Antenna Laboratory
Frequency:	5.55 – 6.05 GHz
Frequency samples:	51 pts
Transmitter array:	5-element ULA
Receiver array:	(5×5) URA
Transmitter spacing:	0.25, 0.5, 1, 2, and 3 λ
Receiver spacing:	0.25, 0.5, 1, 2, and 3 λ

The settings for the various estimation schemes are described below.

- *Sequential estimation of delay, DOA, and DOD*: In this scheme, the delay, DOA, and DOD are estimated using unitary ESPRIT in sequence. For the delay estimation, the frequency array size is 401, and each pair of antennas provides a

snapshot of the frequency array response. The number of delays is determined by setting a threshold of 30 dB at the eigenvalues. In the DOA and DOD estimation, the numbers of paths are determined by the VTRS detection algorithm. The allowed maximum numbers of paths in delay, DOA, and DOD estimations are 400, 6, and 6, respectively.

- *Delay estimation with joint DOA and DOD estimation*: In this scheme, the delay estimation is performed, and the DOA and DOD are estimated jointly. The number of sources in the delay estimation is also determined using a threshold of 30 dB at the eigenvalues, while the number of sources for joint DOA-DOD estimation is obtained by the VTRS algorithm. The maximum number of sources for joint DOA-DOD estimation is 72. This method will be denoted as Delay-DOADOD in the following discussion for convenience.
- *IFFT with sequential DOA and DOD estimation*: This estimation scheme is the same as sequential estimation except that the delay estimation is replaced by transferring the measured data to the time domain using IFFT. When the LOS is available, we consider only the duration from 0 to 100 *ns*, and the sequential DOA and DOD estimation is performed at each time sample (every 2 *ns*) in the duration. When the LOS component is obstructed, which results in longer delay spread, the duration is extended to 150 *ns*. This method is denoted as IFFT-DOA-DOD.
- *IFFT with joint DOA and DOD estimation*: This scheme is the same as previous method, but the sequential angular estimation is replaced by joint estimation. This method is denoted as IFFT-DOADOD.

5.2 Measurement Results

Next, we demonstrate the estimation results and compare the estimation accuracy of these four methods. Once the parameter estimates are obtained, the (5,5×5) channels are reconstructed using (59) to (61), and the channel capacities of the reconstructed channels are compared with the capacities of the directly measured channels. The spherical wave model is used in the channel construction for the LOS component when it is available. The floor plan of the SARL (Figure 16) is shown again for convenience.

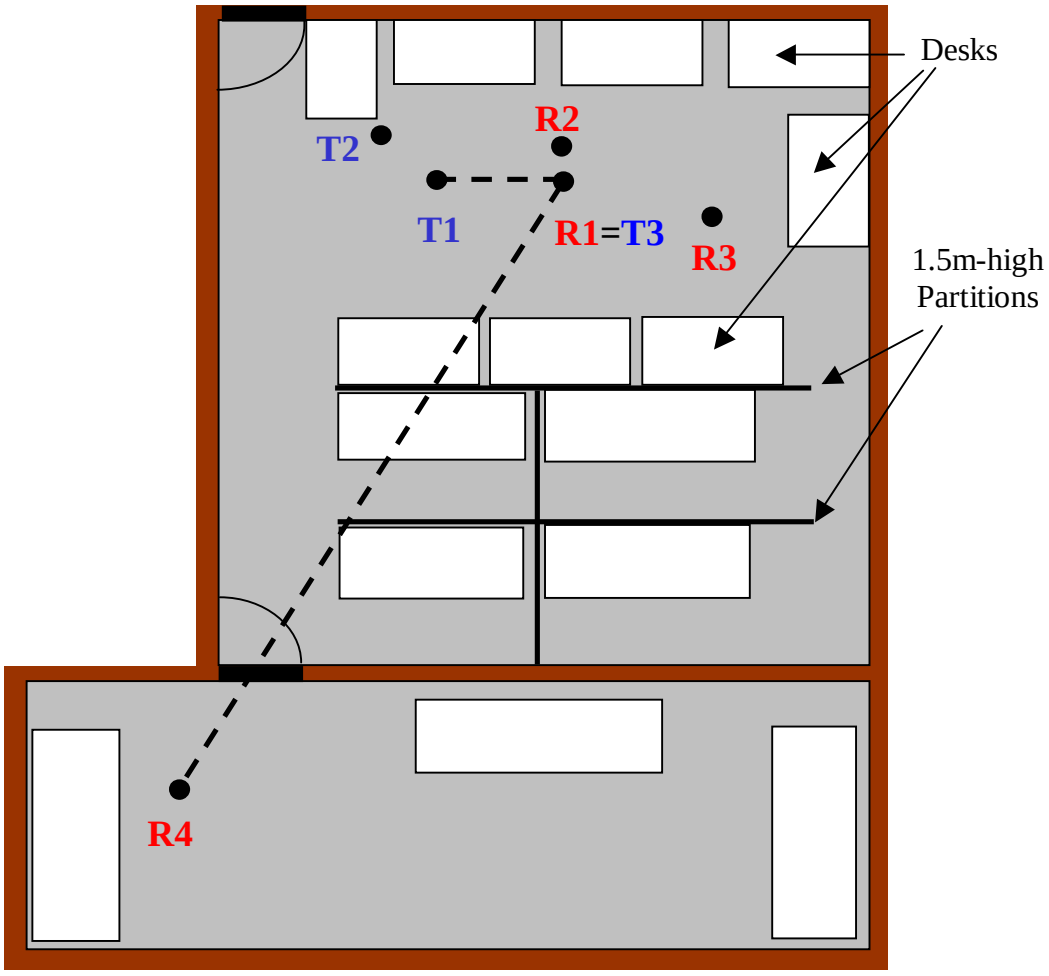

Figure 32: Floor plan of the Smart Antenna Research Laboratory (SARL) at the Georgia Institute of Technology.

Experiments with LOS:

In the first experiment with LOS, the transmit and receive locations are at T1 and R1 respectively in Figure 16. Accordingly, the LOS is available. The antenna spacings of the arrays at both sites are 0.48λ. Figure 33 depicts the power-angle distribution of DOA and DOD, derived by Delay-DOADOD scheme. Only the estimated paths with power larger than maximum power minus 30 dB are shown, and the power is then normalized by the minimum power. Therefore, the power of LOS is 30 dB in the figure after the normalization. The elevation angles of DOA and DOD are concentrated around 90° because the Tx and Rx are about the same height in the system.

The CDFs of the measured MIMO capacities with three different array geometries are shown in Figure 34(a), (c), and (e). The SNR is assumed to be 30 dB in all cases. To begin with, we observe that the capacities for the directly measured channel increase with increasing element spacing, with the biggest increase occurring between 0.25λ and 0.5λ. When Tx and Rx are orthogonal ULAs, the capacity tends to saturate at 0.5λ. On the other hand, when Tx and Rx are parallel, the capacity improvement is still obvious (about 4 bit/sec/Hz) while the spacing is changed from 2λ to 3λ. The performance of ULA-URA combinations is in between. This tells us that the performance of MIMO systems is sensitive to not only the antenna spacing but also the array shapes. The reconstructed channel capacities using the estimates obtained by Delay-DOADOD scenario are shown in Figure 34(b), (d), and (f). Comparing the left and right columns of Figure 34, we found that the reconstructed capacities successfully reflect the different performances of three different array geometries.

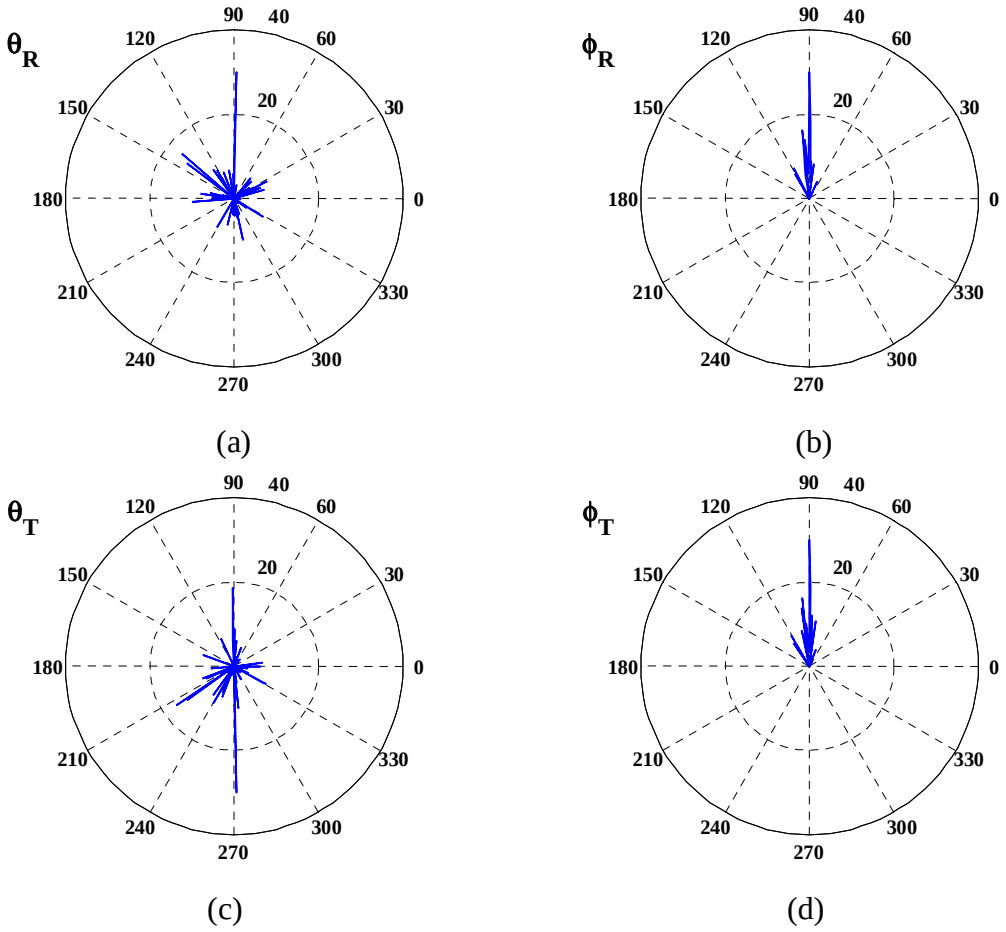

Figure 33: Power-angle distribution of (a) DOA azimuth angle (b) DOA elevation angle (c) DOD azimuth angle, and (d) DOD elevation angle.

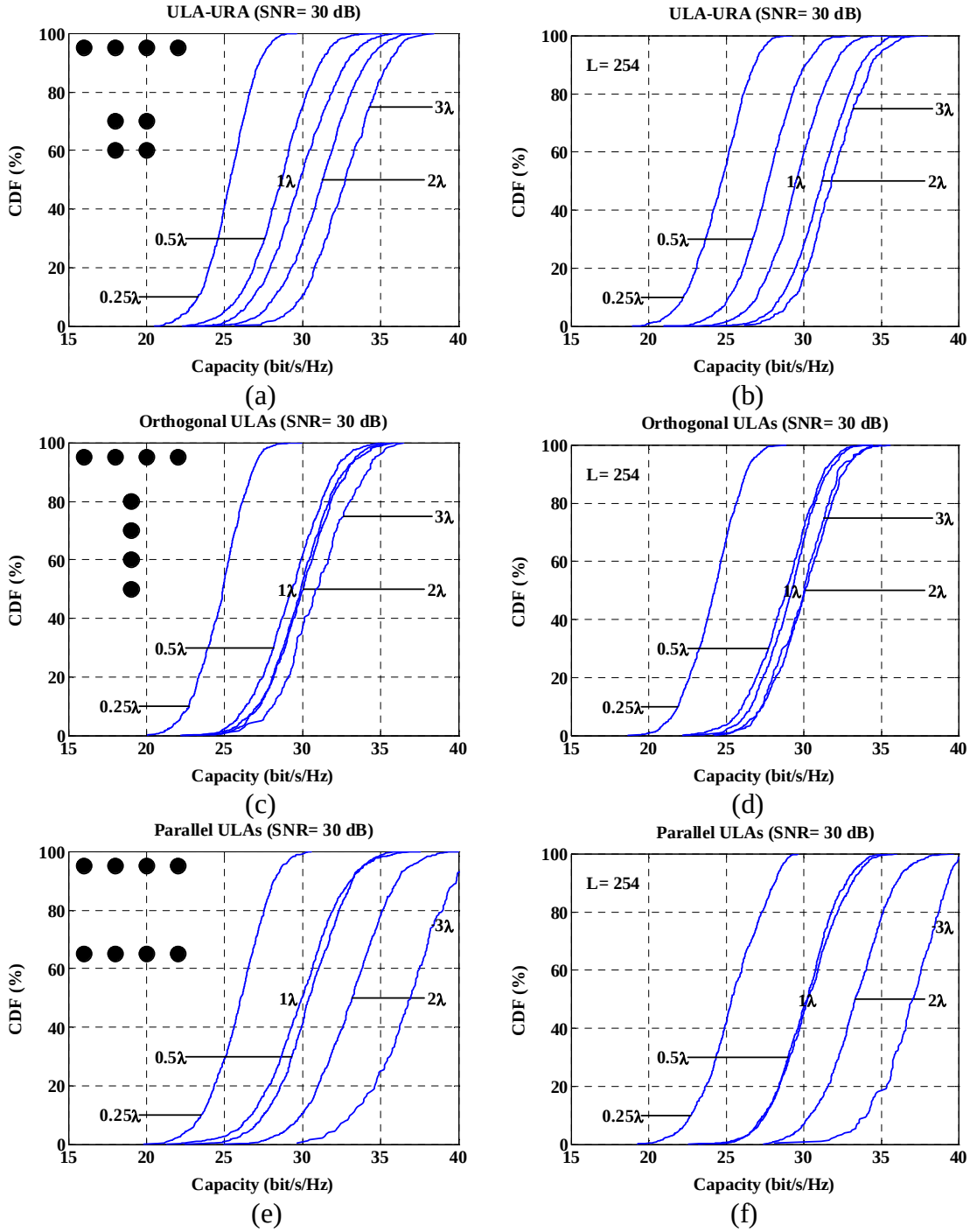

Figure 34: Directly measured and reconstructed capacities using Delay-DOADOD estimation scenario. The directly measured capacities are shown in the left column (a) (c) (e), while the reconstructed capacities are shown in the right column (b) (d) (f). The array geometries of Tx and Rx are plotted in the figures in the left column.

The difference between the mean of the measured capacity and the mean of the reconstructed capacity is shown in Figure 35. This difference is an average over the

estimation errors of three different array shapes. The detected number of paths in sequential, Delay-DOADOD, IFFT-DOA-DOD, and IFFT-DOADOD are 176, 180, 347, and 422, respectively. In this experiment, the Delay-DOADOD scheme, which maintains the estimation error under 0.8 bit/s/Hz, has the best performance. The error is enlarged when the IFFT is used to replace the delay estimation, especially when sequential angle estimation is employed instead of joint estimation. The main problem of sequential estimation is the accumulated error in each step of estimation and lower resolution caused by fewer number of snapshots.

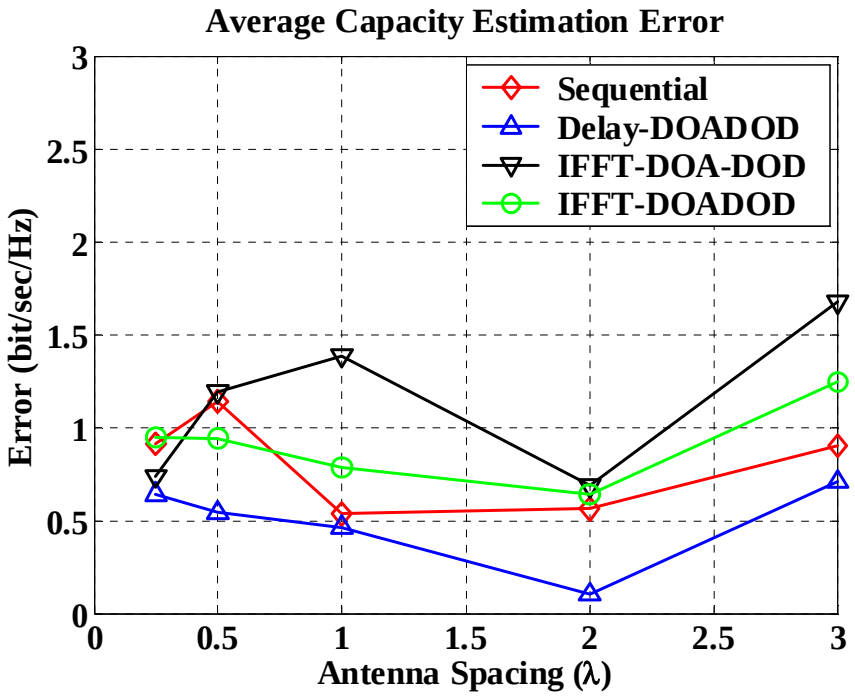

Figure 35: Average capacity estimation error of four estimation scenarios in Experiment 1 with LOS (T1,R1). Delay-DOADOD appears to have the best fit in this experiment.

In the second experiment, the transmitter is located at T2, and the receiver is placed at R2. The antenna spacing is reduced to 0.25λ. Smaller antenna spacing results in smaller array size; therefore, the angular resolution is reduced, but the plane wave assumption, which is assumed in the deduction of the ESPRIT algorithm, becomes more

appropriate. As shown in Figure 36, the maximum error of sequential, Delay-DOADOD, IFFT-DOA-DOD, and IFFT-DOADOD are 2.1, 1.5, 2.3, and 1.8 bits/sec/Hz, respectively. Again, the Delay-DOADOD has lowest maximum estimation error.

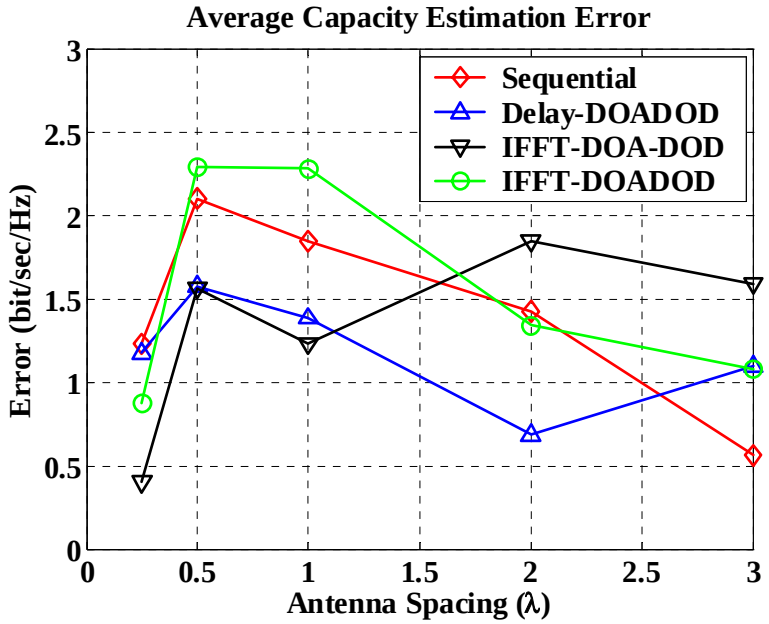

Figure 36: Average capacity estimation error of four estimation scenarios in Experiment 2 with LOS (T2,R2). The performances of all four scenarios are comparable in this experiment, but the Delay-DOADOD still has the smallest maximum error.

In the third experiment, the transmitter and receiver locations of previous experiment are switched, but the antenna spacing is still 0.25λ[*]. In this case, the Delay-DOADOD apparently outperforms the other scenarios; the average estimation error is maintained less than 1 bit/sec/Hz. The IFFT-DOA-DOD produces worst estimation, and the maximum error is as large as 3.2 bits/sec/Hz at the element spacing of 1 λ.

[*] However, two experiments were conducted in different nights; therefore, the locations of surrounding objects were different.

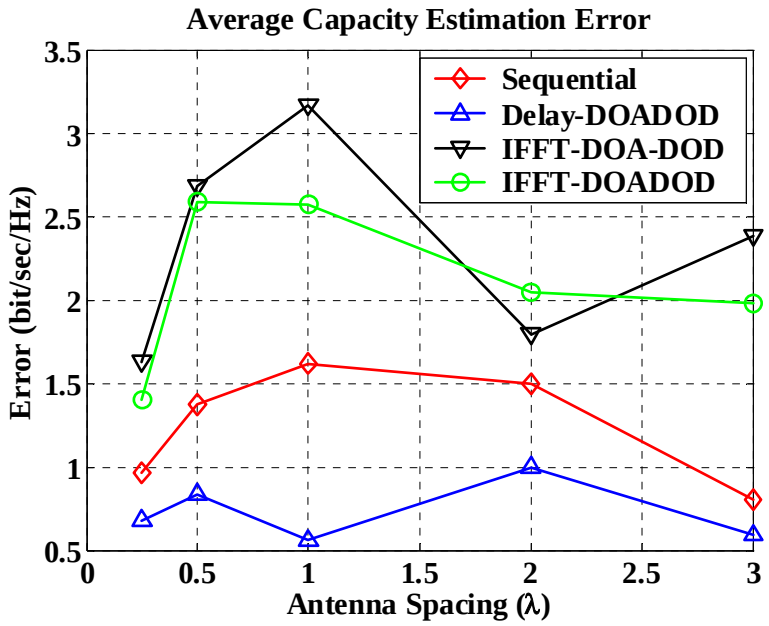

Figure 37: Average capacity estimation error of four estimation scenarios in Experiment 3 with LOS (R2,T2). Delay-DOADOD appears to have the best fit in this experiment.

The final experiment with LOS was conducted at (T2,R3). The antenna spacing is also 0.25λ. As shown in Figure 38, the accumulated error in sequential angle estimation is significant in the IFFT-DOA-DOD scheme, and the result is reflected in the capacity estimation error. The capacity estimation error of this scenario is larger than 4 bits/sec/Hz when the spacing is larger than 0.5λ. The other three scenarios maintain the error to be less than 1 bit/sec/Hz, and the Delay-DOADOD still appears to have the best fit in this case.

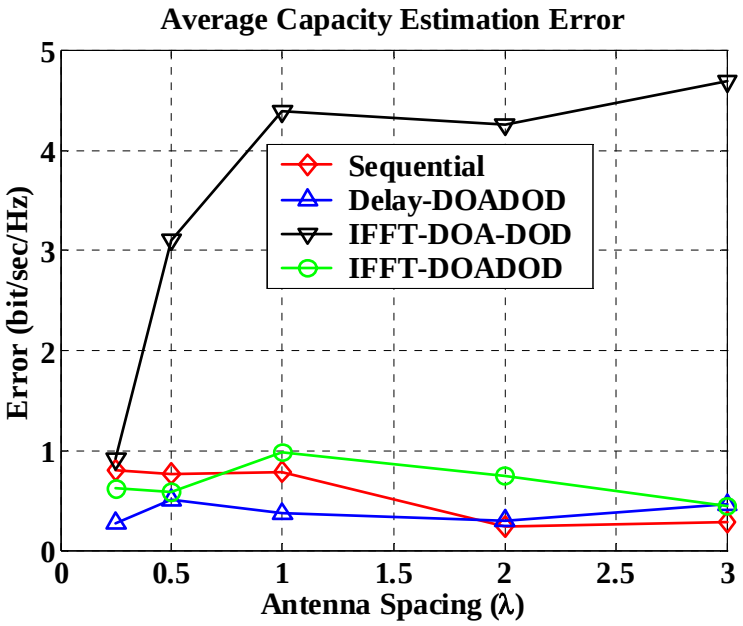

Figure 38: Average capacity estimation error of four estimation scenarios in Experiment 4 with LOS (T2,R3). The Delay-DOADOD scenario appears to have the best fit in this experiment, while the estimation using the IFFT-DOA-DOD is significantly deviated from the measured capacity.

Experiments without LOS:

Next we consider the channel where the LOS component is blocked. The transmitter and the receiver are located at T3 and R4, respectively. In the first experiment, the antenna spacing for parameter estimation is 0.48λ. The power angle profile obtained using the Delay-DOADOD scheme is shown in Figure 39. Both the azimuth and elevation angular spreads become wider compared to the channels with LOS, and the number of multipaths is increased. The detected number of paths in sequential, Delay-DOADOD, IFFT-DOA-DOD, and IFFT-DOADOD are 459, 676, 489, and 743, respectively. The detected number of paths is smaller when the sequential angle estimation is employed mainly because of the restriction of maximum number of signals as mentioned in Section 5.1.

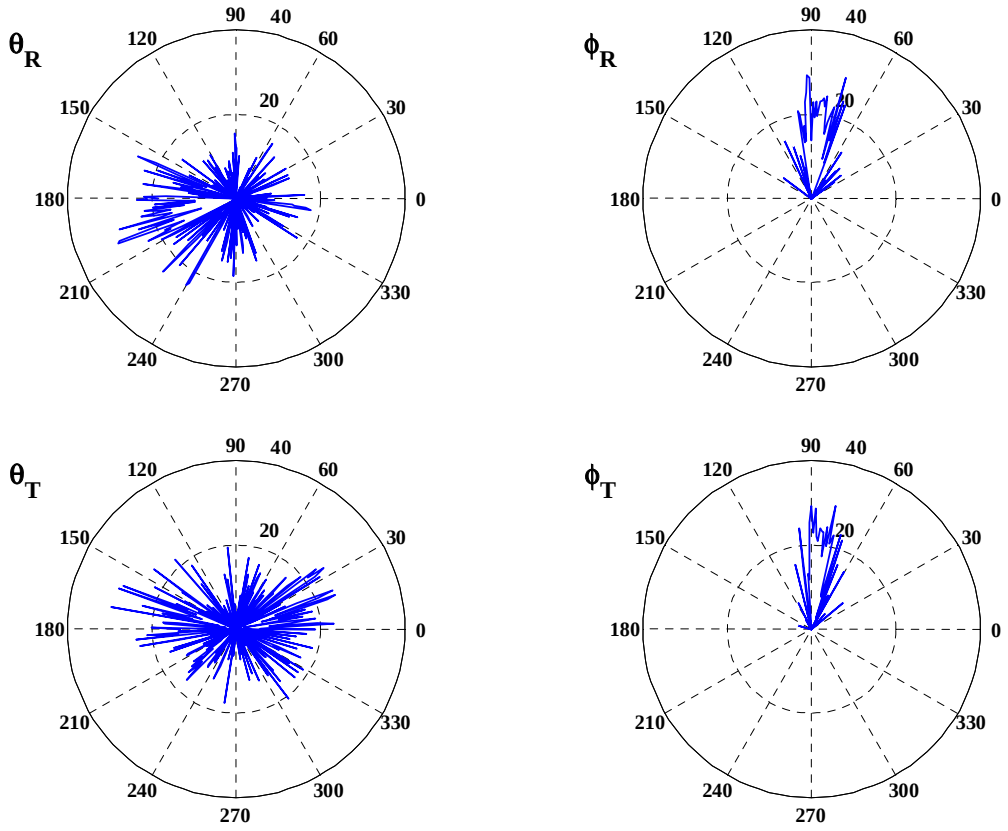

Figure 39: Power-angle distribution of (a) DOA azimuth angle (b) DOA elevation angle (c) DOD azimuth angle, and (d) DOD elevation angle.

The average capacity estimation error is shown in Figure 40. In this case, the sequential estimation produces smallest maximum error, which is equal to 1.8 bit/sec/Hz, but the performance of Delay-DOADOD is comparable. The performance is worse when the IFFT are used to replace the delay estimation.

In the second experiment, the antenna spacing is reduced to 0.25λ for path parameter estimation measurement. Although sequential estimation has good performance in previous experiment, it causes significant error in this case; the maximum error is as large as 5 bits/sec/Hz. The performances of other three scenarios are comparable, and the maximum error of the Delay-DOADOD scenario is kept under 1 bit/sec/Hz.

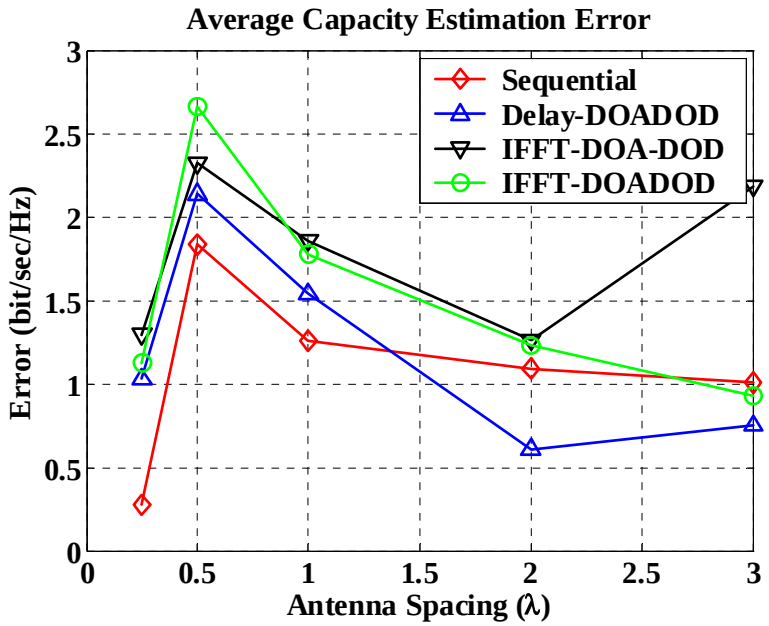

Figure 40: Average capacity estimation error of four estimation scenarios in Experiment 1 without LOS (T3,R4). The performances of all scenarios are comparable. The sequential estimation has smallest maximum estimation error.

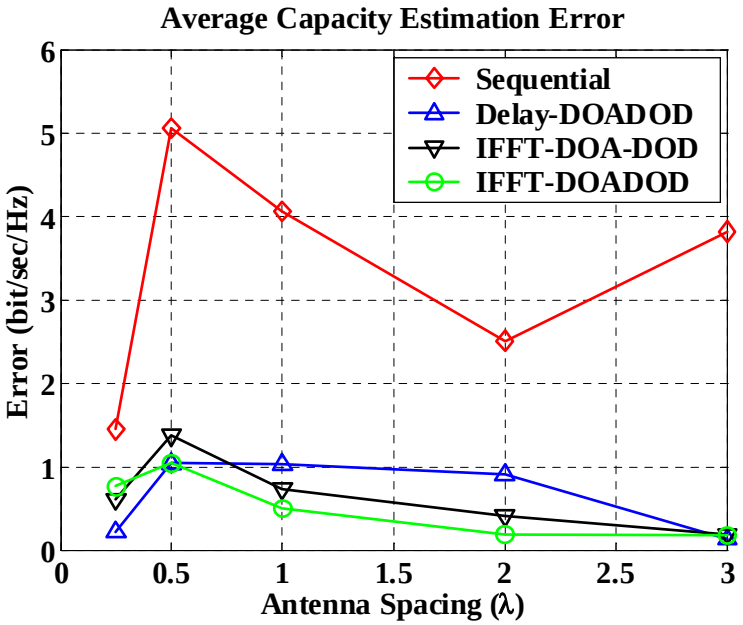

Figure 41: Average capacity estimation error of four estimation scenarios in Experiment 2 without LOS (T3,R4). The antenna spacing for parameter estimation measurement is 0.25λ. Sequential estimation causes significant error in this case.

Overall, the Delay-DOADOD scenario provides the most reliable performance in terms of predicting the MIMO channel capacity of channels with or without LOS component.

5.3 Chapter Summary

In this chapter, we described the experiments for the path parameter estimation as well as for the capacity measurement. We compared the performances of four different estimation methods in terms of the capacity estimation error, which is defined as the difference between the measured and reconstructed capacities. Both the channels with and without LOS were included in the experiments. The results showed that the separate delay estimation followed by joint angle estimation produces most reliable performance. Significant estimation error is observed when the IFFT or sequential angle estimation is involved in some experiments.

Chapter 6

Spherical Wave Model for Short-Range MIMO

6.1 Introduction

MIMO is an extremely spectrum-efficient technology that uses several antennas at both ends of the communication link [1,2]. However, it has been revealed that some factors such as the richness of the multipath, the correlation of the entries of the channel matrix, and the keyhole effect might degrade MIMO system performance significantly in a real environment [4,79]. Presence of a strong line of sight (LOS) component is sometimes viewed as a degradation in the context of MIMO because a strong LOS is usually thought to result in a unity rank channel, and a unity rank channel is incapable of supporting multiple parallel data streams.

This chapter makes several claims: (1) that a LOS MIMO channel can be full rank and yield the highest possible capacity, (2) that the spherical wave model is required to properly analyze short-range MIMO, and (3) that large antenna spacing can have a very significant and positive impact at short range. These claims are interrelated. The full rank as well as the impact of spacing will not be evident in the analysis without modeling the LOS with spherical waves. Furthermore, the full rank will not be reached at some typical wireless local area network ranges without larger than usual antenna spacing.

The work was motivated by a discrepancy involving measured data. In [64], we attempted to estimate the path parameters of the MIMO channel for the purpose of

reconstructing the matrix of MIMO channel gains for arbitrary array geometries. The path parameters included the angles of departure and arrival at the transmitter and receiver arrays, respectively. It was found that the capacity of the reconstructed MIMO channels was less than the directly measured capacity especially for large antenna spacing. In this chapter we show that in the short-range scenarios of [64], a major reason for the discrepancy is incorrect modeling of the line-of-sight (LOS) component. Specifically, we find that computing the phases of the channel gains based on the precise distances between transmit and receive antennas is necessary to alleviate the discrepancy. Use of the spherical wave model for the LOS gives "richness" to even a free-space MIMO channel.

This observation was made in [80], where particular geometries were sought that could yield channel matrices with full rank. In [81] this phenomenon was investigated by simulating the free space and two-path channels, but only two orientations of the arrays were considered. They validated the phenomenon over measured channels in a parking lot with fixed antenna spacing (half a wavelength). Also using the spherical wave model, in [82] it was shown that the capacity was sensitive to element spacing in free-space and Rician fading channels with various K-factors. It was concluded that the sensitivity of the capacity to the element spacing is significantly reduced when the K-factor is less than 10 dB [82].

In contrast to these previous works, we analyze the performance of arrays with various orientations and elevation angles in the free space channel and in a square room with up to 20 reflections. In addition, we specify a distance threshold to determine whether the plane wave model can be used without causing significant errors.

Furthermore, this paper uses a measured indoor channel to show how the more precise LOS model narrows the gap between capacities of measured and reconstructed MIMO channels, especially for larger element spacing. Moreover, because the LOS path is much stronger than the multipath, and because LOS alone can provide substantial capacity, we conclude that special care should be taken when modeling the LOS in short-range MIMO links, even when there is plenty of multipath.

Other authors have considered the effect of element spacing on MIMO capacity. Increased capacity with increased element spacing in NLOS channels has been observed in simulation of stochastic geometric models with angularly clustered multipath [30,32,83], and in ray tracing [31]. The improvement in these cases is attributed to the reduction in correlation of the multipath fading across antennas. [30,31]. Others have analyzed short-range LOS MIMO links using ray tracing and concluded that capacity is either insensitive to spacing [84] or that half-wavelength spacing yields full capacity [29]. In [84], the plane wave model is specified and in [29], the LOS model is not specified. In the context of these previous works, we first note that the LOS component is unfaded, therefore the spacing effects reported here are not because of decorrelation of fading. Secondly, as shown here, the conclusions about spacing that follow from the spherical wave model are different from those of [84] and [29]. Finally, in contrast to [80], we consider the statistics of free-space short-range MIMO capacities for array geometries and random relative orientations that might be encountered in WLAN applications. The results suggest that larger element spacing could be very beneficial for indoor WLANs using MIMO.

The chapter is organized as follows. In Section 6.2, free space channels are considered, and the discrepancy between the plane and spherical wave models is demonstrated for variations in direction-of-arrival (DOA), direction-of-departure (DOD), antenna spacing, and distance between transmit array (Tx) and receive array (Rx). In Section 6.3, we use ray-tracing to simulate the multipath phenomenon in a square room. The performances of these models are compared based on a Monte-Carlo approach. In Section 6.4, we briefly describe our MIMO measurement system and show the measurement results to validate the importance of the spherical wave model in the MIMO channel modeling. The chapter summary is provided in Section 6.5.

6.2 Free Space Channel

The plane and spherical wave models for a (4,4) MIMO system are illustrated in Figure 6. The plane wave model assumes that the incident signal is a plane wave, which means the DOD, (θ_T, ϕ_T) (DOA, (θ_R, ϕ_R)), is the same for all the elements in the Tx (Rx). θ_T and θ_R are the azimuth angles of DOD and DOD, respectively, while ϕ_T and ϕ_R denote the elevation angles. We assume that both the transmit and receive arrays are parallel with the horizontal plane, therefore ϕ_R=180°- ϕ_T. However, when the distance between Tx and Rx is short, or the array size is large, the waves are more appropriately considered as spherical. When spherical waves are used, the DODs and DOAs are different for each pair of transmit and receive antennas; therefore, the DODs and DOAs are represented as (θ_{Tij},ϕ_{Tij}) and (θ_{Rij},ϕ_{Rij}), where *i* and *j* are the indices of the transmit and receive antennas. Assuming each antenna of an array is in the far field of the antennas of the other array,

and that the antenna elements are isotropic, the channel response h between any two antennas is calculated according to the formula:

$$h \propto \frac{e^{-j\frac{2\pi D}{\lambda}}}{D}, \tag{98}$$

where λ is the wavelength of the carrier and D is the distance between the transmit and receive antenna pair. In this section, we assume the LOS is the only path in the channel. Using the plane wave model in free space, the rank of the channel matrix is one no matter how the DOA, DOD, the antenna spacing, and the array geometries are changed. The OL-MIMO capacity formula (2) can be simplified to $C = \log_2 \left|1 + SNR \times n_R\right|$, which results in the minimum capacity. This minimum capacity of the (4,4) MIMO system is 8.65 bits/s/Hz for a SNR of 20 dB. On the other hand, the maximum capacity is $\min(n_T, n_R) \log_2 \left|1 + \frac{SNR \times n_R}{\min(n_T, n_R)}\right|$; this occurs when the channel matrix is orthogonal with equal eigenvalues. For the (4,4) case, this maximum capacity is 26.63 bits/s/Hz for SNR = 20 dB. In the following subsections, we show that the maximum capacity can be reached in free space over distances typically found in WLAN applications using the more precise spherical wave model.

6.2.1 The Azimuth Angle of DOA and DOD

Let both arrays be in the same horizontal plane ($\phi_T = \phi_R = 90°$), and let the distance between the midpoints of Tx and Rx, denoted as the T-R distance, be 100λ. The MIMO capacities calculated using the spherical wave model are shown in Figure 42 for various azimuth angles of DOA, DOD, and for two values of antenna spacing.

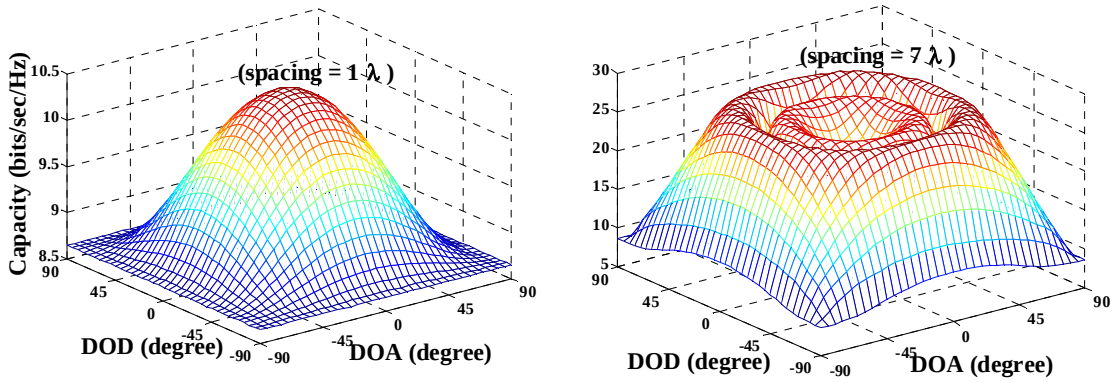

(a) 1λ (b) 7λ

Figure 42: Change of MIMO capacity with DOA and DOD. The distance between transmitter and receiver is 100 λ, and the SNR is 20 dB. The antenna spacings are (a) 1λ and (b) 7λ. In (a), the maximum capacity corresponds to (θ_T, θ_R)=(0°, 0°). In (b), the maximum capacity achieves the capacity of a full-rank channel matrix (26.63 bits/s/Hz).

First, we observe that this capacity varies with DOA and DOD. With the spherical wave model, the low capacity values are achieved when at least one of θ_T and θ_R are -90° or 90°. On the other hand, for 1λ we find that the maximum capacity occurs when the arrays are broadside to each other, or when $\theta_T = \theta_R = 0°$. Also, capacity increases with antenna spacing. The maximum capacity at spacing equal to 1 λ is almost 10.1 bits/s/Hz, which is 1.5 bits/s/Hz larger than that of the plane wave model. When the spacing approaches 5λ (not shown in the figure), the capacity achieves that of a full rank channel matrix, 26.63 bits/s/Hz, which is 18 bits/s/Hz larger than the capacity of plane wave model. When the spacing is less than 5λ, the maximum capacity corresponds to the angles (θ_T, θ_R)=(0°, 0°). When the spacing exceeds 5λ, the maximum is no longer at (0°,0°), as shown in Figure 42(b), but the ripples still reach the maximum capacity. The distribution of the capacity is symmetric about the point (θ_T, θ_R)=(0°, 0°).

A distance threshold that determines when the spherical wave model should be used can be determined empirically. We identify the threshold distance R_{th}, below which

the capacity of spherical wave model is greater than 1.5 times the plane wave model for a given array size. In other words, the capacity underestimation error is 50% at this distance when plane wave model is used, and this error increases dramatically when the T-R distance is shorter than R_{th}. From the above discussion we have realized that the maximum discrepancy between plane and spherical wave models usually corresponds to the arrays being broadside to each other. Therefore, this is the geometry considered next. As shown in Figure 43, for the array sizes 3λ, 6λ, and 9λ, the corresponding threshold distances are 36λ, 144λ, and 324λ, respectively, in the simulation when the number of antennas is 4. The relationship that fits this data is $R_{th} = 4L^2$, where L is the array size in units of wavelength. Given the formula $R_{th} = \alpha L^2$, the value of α ranges from 3.75 to 4.4 for the number of antennas ranging between 3 and 16. Therefore, $4L^2$ is a reasonable threshold distance.

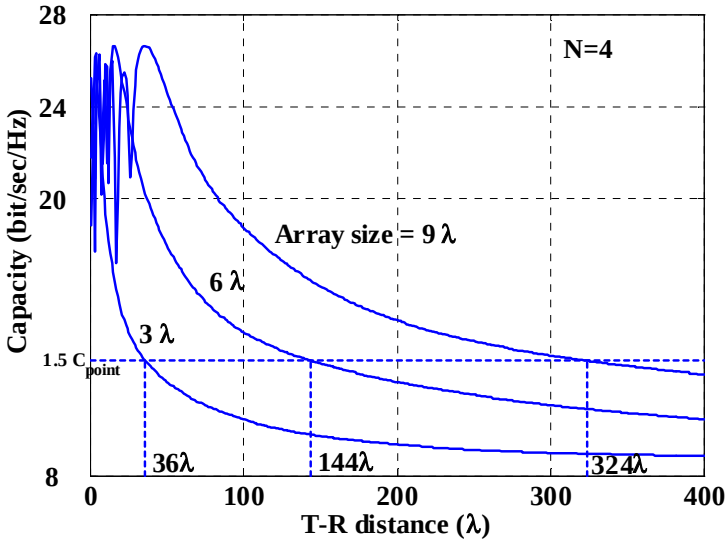

Figure 43: Capacity versus array size and T-R distance. The threshold distances that determine the appropriateness of plane wave model is approximately equal to $4L^2$ where L is the array size in units of wavelength.

It is interesting to note that this threshold distance to distinguish the plane and spherical wave models is similar to the threshold $R = 2L^2$, which marks the boundary

between the Fresnel and the Fraunhofer (Far field) zone, where L denotes the antenna size in this case [21]. This threshold is determined under the constraint that the maximum phase deviation of the received signal between any two points of the antenna is less than $\pi/8$ [21].

The formula for the threshold distance, $R_{th} = 4L^2$, may be generalized by considering a conventional beamforming perspective. The basic idea is that the channel rank will exceed unity when any pair of elements in one of the arrays can be *resolved* by the other array. The resolving capability of an array relates to the beamwidth of its antenna pattern with all-unity weights. The beamwidth of a uniformly weighted array is the same as that of a uniformly illuminated continuous aperture of the same size [41]. Therefore, the resolving capability of an array depends only on its aperture size and not on how many antenna elements fill the aperture.

The normalized broadside radiation pattern of a line source of length L (in units of wavelength) is [41]

$$f(\Theta) = \frac{\sin(L\pi \sin\Theta)}{L\pi \sin\Theta}. \tag{99}$$

Assuming the transmit array size is L_T, the half-power beamwidth of the transmit array is

$$\Theta_{3dB} \approx \frac{0.886}{L_T}. \tag{100}$$

The T-R distance R such that the receive array with array size L_R is entirely within the 3dB beamwidth satisfies

$$\begin{aligned} & L_R \le 2R\sin\tfrac{\Theta_{3dB}}{2} \approx R\Theta_{3dB} \approx \frac{0.886R}{L_T} \\ & \Rightarrow R \ge 1.13 L_R L_T. \end{aligned} \tag{101}$$

This distance, denoted as R_{3dB}, is less than the empirical threshold distance R_{th}. This tells us that the half-power beamwidth is too large to determine the threshold distance because the underestimation of the channel capacity is over 100% at R_{3dB}.

The beamwidth can be adjusted such that the threshold is equal to $4L^2$. In order to meet the specified threshold, $L_R = \frac{0.25R}{L_T}$ must be satisfied. The corresponding power attenuation derived by (99) is approximately equal to 0.225 dB, i.e.

$$\Theta_{th} = \frac{0.25}{L_T} \approx \Theta_{0.225dB}. \tag{102}$$

Therefore, the threshold distance R_{th} is that distance such that the receive array subtends the angle $\Theta_{0.225dB}$, which is the 0.225dB-down beamwidth of the transmit array. The formula can be generalized to the situation when the transmit and receive array sizes are not equal, i.e.

$$R_{th} \approx R_{0.225dB} = 4L_T L_R. \tag{103}$$

This formula can be further generalized to apply to arrays that are broadside to each other. We observe that, a beam from a uniformly illuminated aperture of length L (wavelengths), scanned to an angle θ_T from boresight (i.e. from the broadside direction), has a 3dB beamwidth $0.886/(L_T \cos\theta_T)$ [41]. This is equivalent to substituting L_T in (100) with the effective aperture size presented to the θ_T direction, $L_T \cos\theta_T$. The transmitter effective aperture size is illustrated in Figure 44 by the length of the array of dashed circles at the transmitter end.

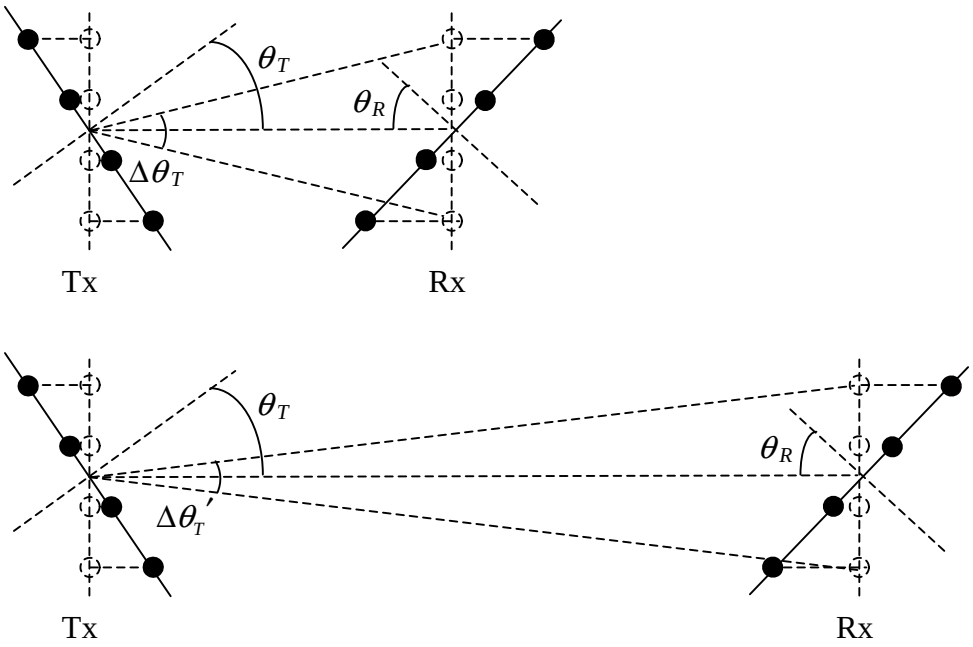

Figure 44: How rotation of arrays and longer range affects the subtended angle $\Delta\theta_T$.

Similarly a linear receive array which is rotated an angle θ_R away from the broadside orientation subtends a smaller angle $\Delta\theta_T$ as viewed from the transmit array, and is therefore more likely to fall within the threshold angle. Therefore (103) may be further generalized to

$$R_{th} = 4L_T L_R \cos\theta_T \cos\theta_R . \tag{104}$$

For example, when two arrays are perpendicular or when they are at the endfire side of each other, the distance R_{th} is equal to 0 because at least one of the DOA or DOD is equal to 90°. In that case, the plane wave model is appropriate for any distance and the channel capacity achieves the minimum value. Finally, Figure 44 shows how the longer range of the lower drawing causes $\Delta\theta_T'$ to be smaller than $\Delta\theta_T$ of the upper drawing, which shows why the plane wave model is appropriate for long range.

Although not tested specifically in this paper, non-linear arrays are conjectured to have the same threshold distance as (103), with L_T and L_R replaced by the effective aperture lengths of the transmit and receive arrays as presented to the directions of each other.

Next, we consider the minimum element spacing to achieve the maximum capacity in the context of beams [85]. With an N-element uniform linear array, totally N orthogonal beams can be formed, and the directions of the beams θ_i, $i = 1, 2, \ldots, N$, satisfy

$$\sin\theta_i = \frac{\left(i - \frac{N+1}{2}\right)}{Nd}, \tag{105}$$

where d is the element spacing in the unit of wavelength [41]. Each beam has its peak gain where the gains of other beams are equal to 0. Therefore, if N receive antennas are placed, respectively, in the directions of the orthogonal beams formed by the transmit array, the channel matrix is close to $N\mathbf{I}$ where $\mathbf{I}$ is the identity matrix [85]. Assuming the element spacings of the transmit array and the receive arrays are d_T and d_R in units of wavelength, respectively, and assuming each receive antenna is placed in the direction of a different orthogonal beam, we have

$$\begin{aligned} \sin\theta_N &= \sin\left(\frac{\Delta\theta}{2}\right) = \frac{(N-1)}{2Nd_T} = \frac{\frac{(N-1)d_R}{2}}{\sqrt{R^2 + \left(\frac{(N-1)d_R}{2}\right)^2}} \\ \Rightarrow d_R &= \frac{2R}{\sqrt{(2Nd_T)^2 - (N-1)^2}} \end{aligned}. \tag{106}$$

When $d_T \gg \left(\frac{N-1}{2N}\right)$, the receive element spacing d_R can be approximated by

$$d_R \approx \frac{R}{Nd_T}. \tag{107}$$

For example, when R = 100, $N = 4$, and $d_T = d_R$, the minimum receive element spacing to achieve the full rank is 5λ, which is consistent with our previous simulation result.

When MIMO is applied to the indoor wireless LAN using 4 antennas with the center frequency at 5.8 GHz, the threshold distances are around 1.86m, 7m, and 16.8m for the antenna spacings of 1λ, 2λ, and 3λ, respectively. This indicates that the spherical wave model should be used, and antenna spacings in excess of 1λ should be considered, for MIMO in indoor wireless LAN applications where the client platform, such as a laptop computer or flat-panel TV, might support larger element spacings.

6.2.2 The Elevation Angle of DOA and DOD

Since MIMO capacity depends on the difference among the DOAs and the differences among the DODs for different elements, the performance can be affected by changing the elevation angle, which is defined as the angle between the LOS path and Z-axis, as shown in Figure 6. For example, when the arrays are at the endfire side of each other, i.e. the azimuth angles (θ_T, θ_R)=(-90°, -90°) and the elevation angles $\phi_T = \phi_R = 90°$ (Tx and Rx on the same plane), the system has minimum capacity. As the elevation angle grows from this point, the relative geometry between the arrays is the same as though both arrays were in the same horizontal plane and the azimuth angles were following the $\theta_T = \theta_R$ line. This implies that increasing the elevation angle corresponds to an increase in capacity.

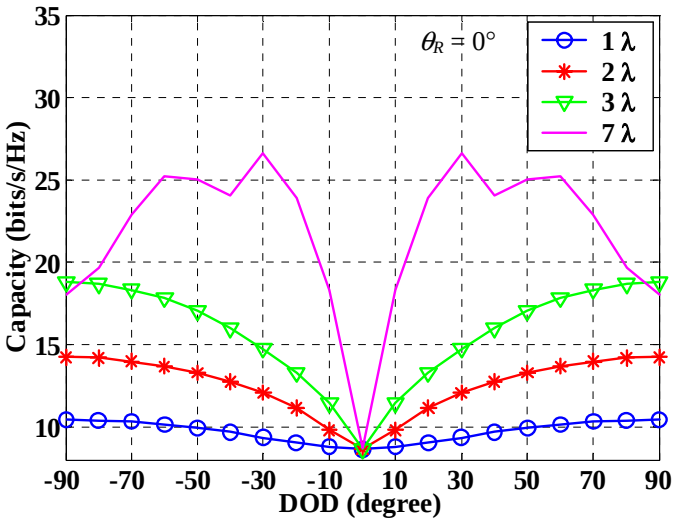

Figure 45: The impact of elevation angle to the MIMO system with different antenna spacing. The azimuth DOA is fixed at 0°, the T-R distance is 100 λ, and the SNR is 20 dB.

The previous azimuth variations do not capture relative twists between the arrays. Figure 45 shows the capacity when ϕ_T = 0° (i.e. when one array is directly above the other), for various relative azimuth angles. In the simulation, the θ_R is fixed at 90° and the θ_T varies from -90 to 90°. For all four antenna spacings, the minimum channel capacity occurs at θ_T = 0°, i.e. when Tx and Rx arrays are orthogonal to each other. The average capacities are 9.7, 12.5, 15.8, and 21.9 bits/s/Hz for 1, 2, 3, and 7λ, respectively. Comparing these to the corresponding average capacities of 8.6, 8.6, 8.7, 9.9 bits/s/Hz when the elevation angle ϕ_T = 90°, the improvement ranges from 12.8% to 121.2%, increasing with antenna spacing. Since the channel capacity is dominated by the LOS when it is available, the results suggest that the access point should be placed on the ceiling and element spacing should be several wavelengths to increase the performance of the MIMO system.

6.2.3 Array Geometry

The MIMO capacity also changes with the array shape in free space when the spherical wave model is utilized. For instance, the channel with (θ_T, θ_R)=(-90°, -90°) is the same as (θ_T, θ_R)=(0°,0°) when the transmitter and receiver are uniform rectangular arrays (URAs); however, these two conditions correspond to the maximum and minimum capacity when the ULAs are employed instead. In Figure 46, we compare the performance of the arrays with different combinations, including ULA-ULA, ULA-URA, and URA-URA. Because of the reciprocity of the MIMO channels, the performance of URA-ULA is the same as for ULA-URA. The SNR is 20 dB, the element spacing is 2λ, and two ranges are considered, which yield T-R distance to element spacing ratios of 50 and 10, as indicated in Figure 46. The average and standard deviation of the capacity are derived assuming the DOA and DOD are independent random variables and both uniformly distributed over [-90°, 90°]. In Figure 46, the length of the vertical line on each curve represents the standard deviation for the corresponding array arrangement and elevation angle.

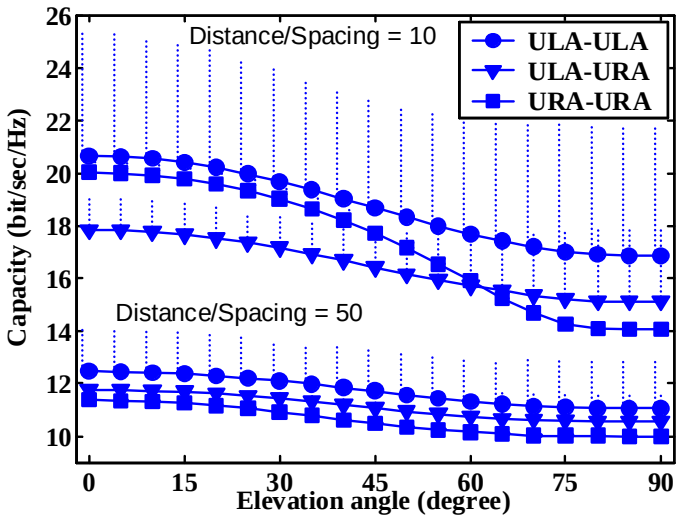

Figure 46: The average and standard deviation of MIMO capacity of different array geometries: The distance-to-spacing ratios are 50 and 10.

First we notice that the average capacities of the arrays with small distance-to-spacing-ratio are higher than that of the arrays with the larger ratio. The ULA-ULA combination has the best average capacity for all cases, but its standard deviation is also the largest. The average capacity of URA-URA surpasses ULA-URA at most elevation angles when the distance-to-spacing ratio is 10 (i.e. for the shorter ranges). In all cases, the capacity achieves its maximum when the elevation angle is close to 0°. The elevation angle effect is more significant when the distance-to-spacing ratio is smaller. For example, when the ratio is 10, the maximum variation of the average capacity is about 6 bits/s/Hz for URA-URA system. In addition, URA-URA has the feature of smallest variance compared with the other two combinations. In other words, the performance of URA-URA is more robust to relative rotation of the arrays. Finally, we note that on the average, element spacing improves the URA-URA channel by about the same amount, 10 bits/s/Hz, at the zero elevation as it does the ULA-ULA configuration.

6.3 Channels With Multipath

In the previous section, we considered the capacity of the MIMO link when the LOS is the only path in the channel. However, in reality there are multiple paths caused by the reflection, refraction, and scattering of the objects around the antennas. In this section, we compare the plane and spherical wave models in a square room using 2D ray tracing with the image method [86]. The reflection coefficient ρ of the walls can be expressed as [84,87]

$$\rho = \frac{\sqrt{\varepsilon - \sin^2\theta} - \varepsilon\cos\theta}{\sqrt{\varepsilon - \sin^2\theta} + \varepsilon\cos\theta}, \tag{108}$$

where ε is the relative permittivity of the wall, and θ is the incident angle. This formula assumes the antenna is vertically polarized. In the simulation, we assume ε = 5 and the room size is (160 × 160) λ. The SNR is 20 dB. When the frequency is 5.8 GHz, the room size is about (8m × 8m), which is the size of a typical office. Both Tx and Rx are 4-element ULAs, and they are located at random and in the same horizontal plane in the room. The orientation of the array is also uniformly distributed in azimuth over [-90°, 90°]. With up to n times of reflection, the total number of reflected paths is equal to $2n(n+1)$. In our simulation, up to 20 reflections are considered, so the number of total paths is 840. The number of trials in the simulation is 5000. Figure 47 shows the average capacities for normalized channel matrices with the plane and spherical wave models. As illustrated in Figure 47, the discrepancy between these two models is negligible when the antenna spacing is less than one wavelength, but the error increases with the antenna spacing. We observe the difference of the average capacity is about 3 bits/s/Hz at 5λ

when LOS is not included. If the LOS is included in the simulations, bringing the total number of paths to 841, the discrepancy increases to 6.2 bits/s/Hz. In the plane wave model, the average capacity tends to saturate when the antenna spacing exceeds 1 λ, whereas in the spherical wave model, the performance improves continuously for antenna spacing up to 5 λ. The antenna spacings beyond 5 λ are not considered in the simulation because large array size restricts the array locations to be in a very small area of the room.

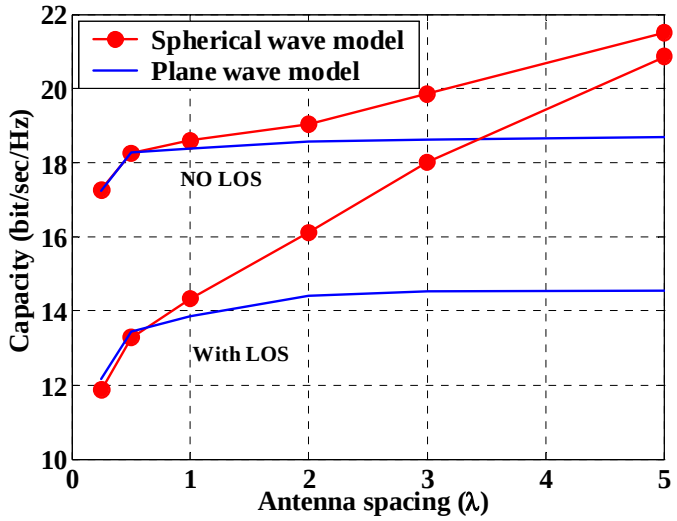

Figure 47: Comparison of the average capacities using spherical and plane wave models. The discrepancy becomes obvious when the spacing exceeds 1λ. This discrepancy is exacerbated when LOS path is included.

6.4 Validation With Measurement

In Section 5.2, we compare different estimation schemes in terms of the difference of the measured and reconstructed capacities. In this section, the first experiment with LOS in Section 5.2 is employed to demonstrate the performance underestimation of plane wave model. The Delay-DOADOD, which is the most reliable estimation scheme according to the result in Chapter 5, is applied to estimate the path parameters. The channels are then reconstructed using both plane and spherical wave

models. Figure 48 shows the average capacity error as a function of the LOS model and the array geometries.

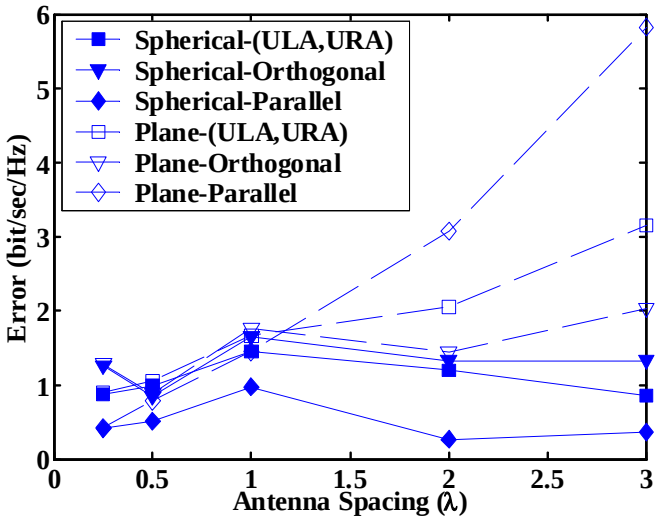

Figure 48: Comparison of measured and estimated capacities: Difference between the mean capacities of the directly measured and reconstructed channels.

The array geometries considered include the (4,2×2) systems and the (4,4) MIMO systems where the ULAs at both ends are either parallel or orthogonal to each other. In all cases, the difference increases with the antenna spacing when plane wave model is used, while the difference is maintained at a low level for various antenna spacings when spherical wave model is applied. We observe that the plane wave model obviously underestimates the measured capacity when the antenna spacing is 1λ or larger. When the antenna spacing is 3λ, the error in capacity resulting from use of the plane wave model is as large as 6 bits/sec/Hz. In contrast, the estimated capacity based on the spherical wave model has much better agreement with the measured capacity.

6.5 Chapter Summary

In this chapter, we considered the pure LOS channel as well as multipath channels based on ray-tracing methods and on measurements. We showed that when the LOS is present, the spherical wave model is more appropriate than the plane wave model for MIMO systems when the T-R distance is short or the antenna spacing is large. A threshold distance was determined empirically and generalized using beamspace arguments. We also showed that, unlike the plane wave model, the spherical wave model enables the performance of the short-range LOS MIMO system to be significantly improved by properly adjusting the DOA, DOD, and the array geometries. In particular, capacity can be dramatically improved by increasing the antenna spacing at both ends of the link. According to the simulations, better capacity can be achieved by placing the base station on the ceiling, provided the LOS is available. The results suggest that greater-than-single wavelength element spacing should be considered for non-handheld user platforms such as the applications of WLAN. In this chapter, we considered only the narrowband flat-fading channel. However, wide bandwidth is employed in some applications like WLAN. In addition, the effect of antenna polarization is also not considered here. These two issues are suggested as a subject for future investigation.

Chapter 7

Effect Of Array Element Spacing and Interference

7.1 Introduction

In the previous chapter, we saw that the array geometry plays an influential role in the performance of MIMO systems. The performance could be significantly changed by simply changing the element spacing, manipulating the orientation of the arrays, or modifying the shape of the arrays. In this section, we concentrate on the element spacing and explore its effect on MIMO channels in a real indoor environment through measurement. The experiments were conducted in the Residential Laboratory at the Georgia Institute of Technology. After introducing the experimental environment, we first consider channels without interference, and then proceed to the more complicated channels with interference. Interferences with different levels of correlation with the intended signals are considered in the discussion. Since stream control is important for interfering MIMO links [34,88], we consider cases with and without stream control. We will show that the antenna spacing that achieves the best capacity in channels without interference is a good choice with interference only when the number of the transmit streams is limited.

According to the discussion in Chapters 5 and 6, the MIMO channel capacity can be enhanced by changing the array geometries. In [80], the author considered some

simple environments like free space channel, and sought particular geometries that could yield channel matrices with full rank, with which the maximum capacity can be achieved. The primary drawback of this method is that the geometry cannot be found in more complicated channels. Some research groups have found significant SNR improvements for spatial multiplexing over simulated channels by adaptively selecting only a subset of the available transmit antennas [37,38,89,90]. The disadvantages of this method include the cost of those unused antennas and the insertion loss of the switch. One other group has considered theoretically how optimization of the antenna element locations at both ends of a normalized link might affect the distribution of singular values of the channel matrix for the best and worst cases of Shannon capacity [25,26]. This latter work may be thought of as an adaptive element location approach. They concluded that at high SNR, the maximum capacity can be achieved when all singular values are the same, while at low SNR the capacity is optimized when one singular value dominates with the others close to zero. A part of this chapter is dedicated to implementing the adaptive-position arrays to verify their conclusions and measure the capacity enhancement potential of this method.

7.2 Measurement Environments and Settings

The experiments were conducted in the Residential Laboratory at the Georgia Institute of Technology. The walls in this building are constructed with wood and plasterboard. As shown in Figure 49, there were two receive array locations and eight transmit array locations. The Tx and Rx are both at a height of approximately 1.35m. The transmitter was a virtual 25-element (5×5) square array and the receiver was a virtual 5-

element uniform linear array. For each Tx-Rx pair, five measurements were sequentially performed to acquire the channel matrices for five antenna spacings: 0.25λ, 0.5λ, 1λ, 2λ, and 3λ. From each (5×5,5) channel matrix, we extracted 20 (4,4) channel matrices of uniform linear arrays. Each component of the channel matrix is in fact the wideband frequency response with 51 frequency samples over a bandwidth of 500 MHz centered at 5.8 GHz. The abundant frequency samples are utilized to increase the number of outcomes in the calculation of ergodic narrowband channel capacity. In summary, at each Tx-Rx location, we obtain 20×51=1020 realizations of (4,4) flat fading channel matrices, and 20 wideband channel matrices with 500 MHz bandwidth.

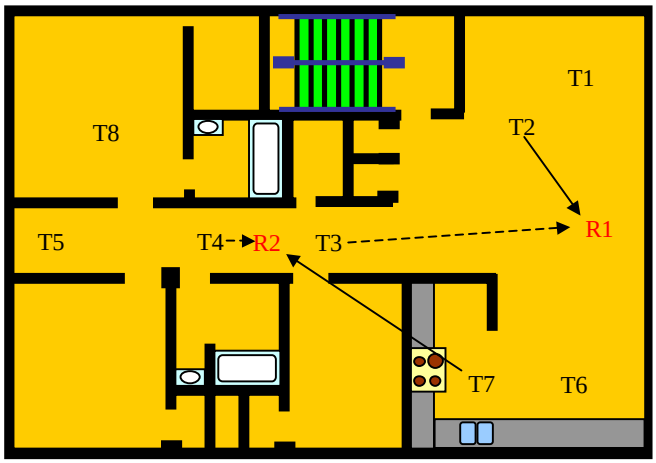

Figure 49: Floor plan of the Residential Laboratory at the Georgia Institute of Technology.

7.3 Model and Normalization Schemes for Channels with Interference

Next, we introduce the network model that we use to analyze the effects of interference. As shown in Figure 50, the network model comprises two pairs of co-channel MIMO links and will be represented as (Node 1–Node 2, Node 3–Node 4). Node

1 transmits the data to the desired user Node 2, while it also causes interference to the other receiver Node 4. Likewise, the receiver at Node 2, the desired receiver of Node 1, receives interference from Node 3. This simple 4-node network model is also employed in [35]. The throughput C_{tot}, defined as the summation of the capacities of two intended links C_{12} and C_{34}, is employed as the performance criterion in the subsequent discussions.

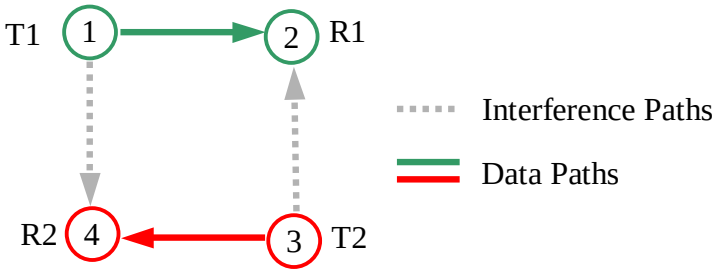

Figure 50: The 4-node network model with interference.

Four representative configurations will be considered in the following sections, including Conf. I: (T2-R1, T7-R2), Conf. II: (T8-R1, T6-R2), Conf. III: (T3-R1, T4-R2), and Conf. IV: (T3-R1, T5-R2). The first two configurations represent channels with less correlated interference because the directions of data and interference paths are angularly separated for both links. For the last two configurations, the data and interference for both links are spatially more correlated because of the confinement of the hallway. In order to illustrate the configurations of the links, the first and third configurations are shown in Figure 49 with solid and dashed arrows, respectively.

Two kinds of normalizations are used in the following two chapters. The first normalization, indicated as distance-preserving normalization, takes into account the effects of the network topology, i.e. node distances. In this normalization scheme, data link of Link 1 (the first in the ordered pair notation) is scaled such that its channel matrix has a Frobenius norm of 4 (each element has approximately unity mean square value). Then the same scaling factor is used for the other data link and the two interference links.

Through this kind of normalization, different levels of path loss caused by different distances of the link are faithfully reflected. Assuming the transmit power of both transmit nodes is the same, the average link SNRs are generally not equal because of varying node distances. With this approach, we can better observe the effects of LOS and node distances among different configurations. This approach will be employed in this chapter, where we discuss the effects of element spacing on the LOS, and stream control.

The second normalization scheme, denoted as equal-SINR normalization, normalizes all four links (data and interferences) individually such that every channel matrix has a Frobenius norm of 4. This approach maintains the angular spread of the multipath, while removing the range-dependent effects. This normalization scheme results in comparable interferences in each configuration, and the effect of interference will primarily be dependent upon the multipath angular spread instead of the distance. Take Conf II as an example: the power of data link T8-R1 is quite weak because of the long distance and obstruction of multiple walls, while the power of the interference link T6-R1 is extremely strong because of the availability of LOS and short distance. After equal-SINR normalization, the power of T8-R1 will be commensurate with T6-R1, and the spatial correlation between the data and the interfering links become the dominant factor to the overall throughput. This type of normalization will be used later in Chapter 8, where the focus is on the comparison of beam selection and antenna selection scenarios.

7.4 Channels Without Interference

Having described the network model and normalization schemes, we are now in a position to analyze the effects of various factors on the performance of MIMO channels

based on the measured data. In this section, the element spacings, availability of LOS, and stream control are three central points that we are going to discuss. We will start from the channels without interference and use them as references in the subsequent discussion of channels with interference.

In this section, all four antennas are used at both ends, and the (4,4) channel matrix is normalized such that its Frobenius norm is 4 before the calculation of its OL-MIMO capacity.

In Figure 51, Link T2−R1, where LOS is available, is considered. We find that the capacity grows with spacing larger than 0.5λ. This short-range MIMO property is explained in Chapter 6. At 20 bits/s/Hz, a 4 dB SNR improvement is obtained by increasing the spacing from 0.5λ to 3λ. Furthermore, the increase of antenna spacing also causes higher capacity slope. At high SNR range, the slope is only 2.88 bits per 3dB at 0.25λ, while at 3λ the slope rises to 3.78 bits per 3dB, which is already close to the theoretical limit of 4 bits/3dB with 4 data streams.

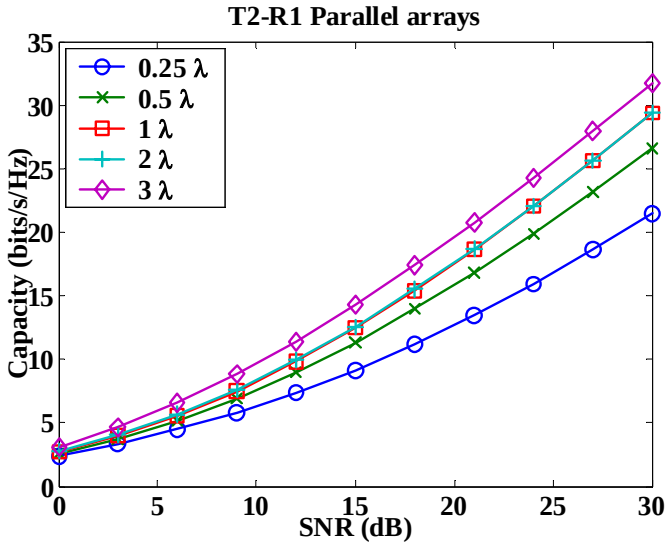

Figure 51: Capacities of Link T2-R1 with five different antenna spacings. There is no interference, and the LOS is available.

While the general shapes of the T7-R2 capacity curves are the same as for T2-R1, both the capacity values and the curve slopes become stabilized after 0.5λ. For example, at 0.25λ, the slope is only 3.14 bits/3dB, but it is increased to 3.86 bits/3dB at 0.5λ. At 3λ, the slope is 3.91 bits/3dB. No apparent benefit is observed using large antenna spacing in this case, which tells us that the spacing of 0.5λ is already sufficient to provide the decorrelation because of larger angular spread of multipath. This measurement result with obstructed LOS is consistent with the conclusion made in [29] based on ray-tracing and [27] based on the one-ring model.

Comparing these normalized LOS and OLOS links, we find that the maximum capacity of the channel without LOS (34.731 bits/s/Hz) is about 3 bits/s/Hz better than the channel with LOS (31.736 bits/s/Hz). It must be noted that the signal power factor is not included in the comparison since the normalization is applied to these two channels separately. Therefore, it would be fallacious to make a conclusion that the LOS should be obstructed on purpose as to obtain better performance for the MIMO systems. In fact, the power of Link T2-R1 is about 24.3 dB stronger than Link T7-R2. If the additional path loss of 24.3 dB is considered, the maximum capacity of the obstructed channel T7-R2 is only 7.22 bits/s/Hz.

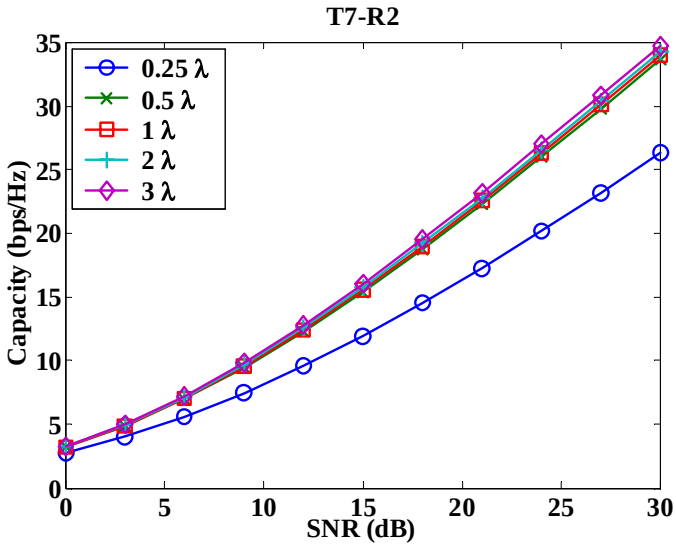

Figure 52: Capacities of Link T7-R2 with five different antenna spacings. There is no interference, and the LOS is obstructed.

So far we have provided only two realizations of indoor channels as representative examples. In the LOS case, large antenna spacing is beneficial, but it is not when the LOS is obstructed. In order to realize the general impact of the element spacing to the performance of MIMO systems in the indoor environment, we considered all 16 measured Tx-Rx locations, as shown in Figure 49. We found that by increasing the spacing from 0.5 to 3λ, the capacity improvement ranges from 8% to 70% with an average of 30%, indicating that half a wavelength is generally not sufficient to decorrelate the signals of MIMO channels even though the multipath is rich in the indoor environment. This situation is particularly obvious when the performance is dominated by the LOS or a few strong paths.

7.5 Channels With Interference

Figure 53 shows the throughputs of the configurations with less correlated interference without stream control. Increasing the spacing tends to reduce the slope of

the curve at high SNR. The explanation for the phenomenon is that wider antenna spacing increases the average effective rank of the channel matrix in the MIMO system and because of the whitening, the signal-to-interference ratio decreases for every transmitted stream. For Conf. I, the slope at 0.25λ at high SNR is only 1.92 bits/3dB, indicating that whitening has reduced the effective rank of each link to less than one. When the spacing is increased to 3λ, the slope is further reduced to 0.836 bits. For Conf. II, because Link T8-R1, a data link with weak signal, is normalized to achieve the intended SNR, distance-preserving normalization makes T6-R1 an extremely strong interference. Under the circumstances, the slope of 0.25λ at high SNR is already dropped to 0.733 bits/3dB at high SNR. When the antenna spacing is further increased to 3λ, almost all data streams are wiped out by the interference, and the slope is only 0.016 bits/3dB. The increase of SNR has little benefit to the throughout. The throughput in Conf. II is much less than Conf. I for the larger spacings. We attribute this to the following. While the larger element spacing benefits the LOS link T2-R1, as was shown in Figure 51, that benefit is offset by the increased rank of the interference links T7-R1 and T2-R2. In Conf. II, on the other hand, only the strong interference link T6-R1 has LOS, so increased spacing offers only degradation.

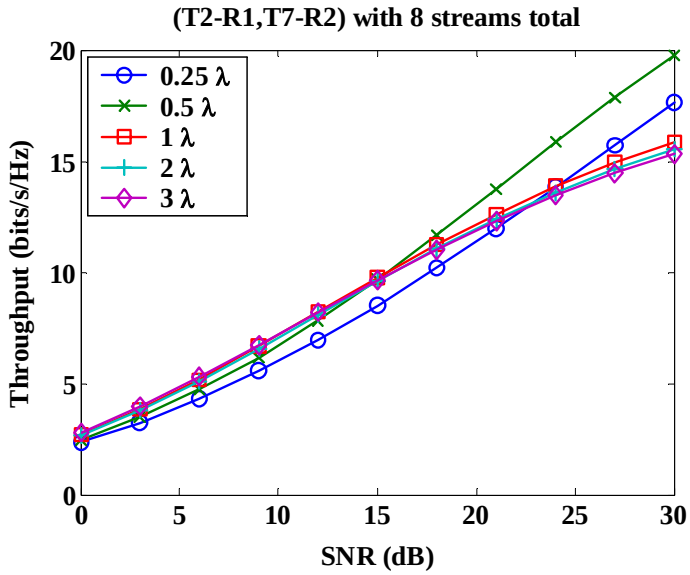

(a) Conf. I

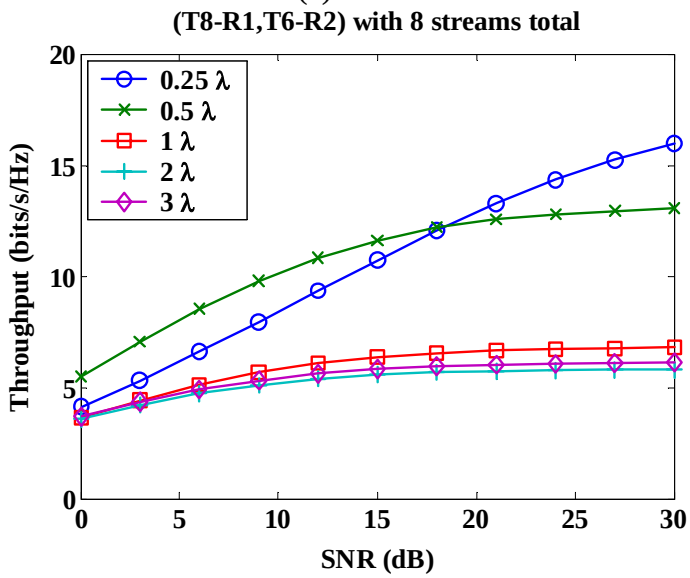

(b) Conf. II

Figure 53: Throughputs of configurations with less correlated interference. No stream control: (a) Conf. I (b) Conf. II.

Figure 54 shows the performance of Conf. III without stream control. The larger spacings perform best at low SNR. This happens because all links have LOS, while the SIR is about -5 dB on T4-R2, and about 2 dB on T3-R1. This means larger spacing gives an overall advantage to the links, even at low SNR. However, as the SNR increases, the rank of the interference dominates, forcing the capacity slopes of the highest spacings to

zero. The capacity slopes of the largest spacings are forced down sooner (i.e. at lower SNR) for Conf. IV because the SIR of Link T5-R2 is -11 dB. As in Confs. I and II, the widest spacings hurt performance. The performance in Conf. IV is similar to Conf. III because of similar topology, but the slope-decreasing phenomenon for wide antenna spacing is even worse than Conf. III. In Conf. IV, the performance at 0.25λ already overpasses 2λ when the SNR is larger than 23 dB, while in Conf. III the throughput with 2λ is still better untill 28 dB. Although the slopes of the widest spacing are reduced to less than 1 bit/3dB, the throughputs of these two highly correlated configurations are better than Conf. II. This can be explained by the short distance of the interference link T6-R1, which results in extremely small SINR for the data link T8-R1.

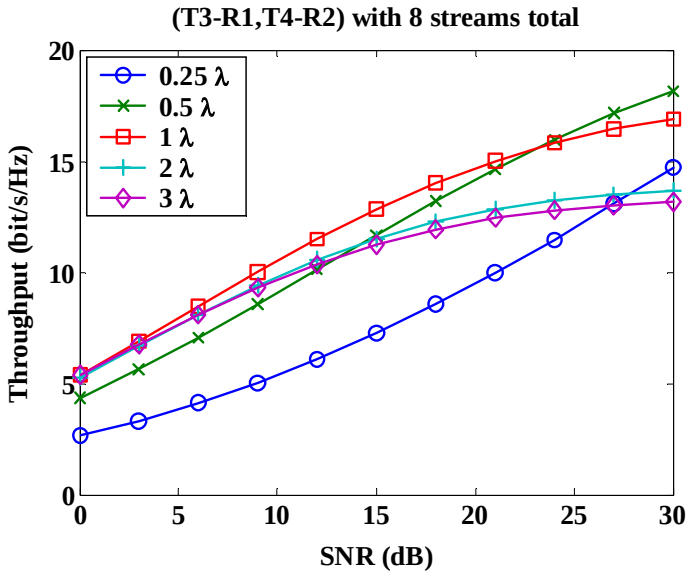

(a) Conf. III

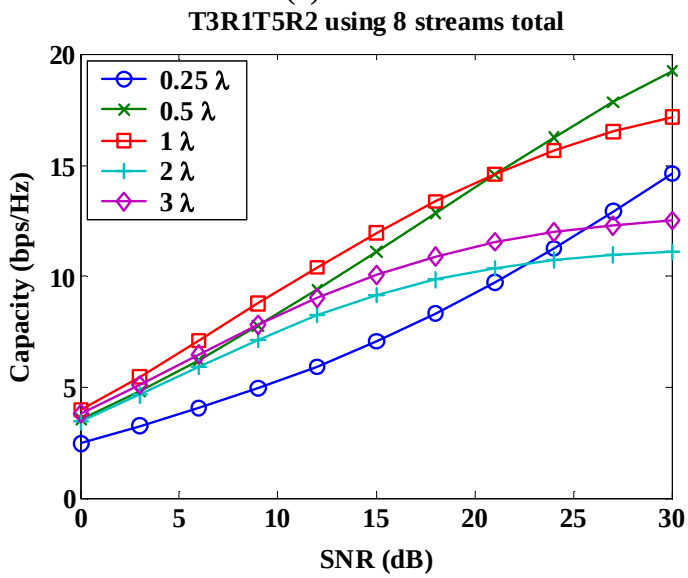

(b) Conf. IV

Figure 54: Throughputs of Conf. III with highly correlated interference. No stream control: (a) Conf. III (b) Conf. IV.

Now, let us consider the throughputs with stream control. Stream control avoids the situation that the total number of streams is greater than the number of receive antennas. With OL-MIMO, stream control implies antenna subset selection. The selection can be made optimal with respect to some criterion, such as capacity; this is done in

Chapter 8. In this section, however, we wish to study element spacing effects, so here we use deterministic selection. Specifically we always choose the first two elements.

Stream control gives spatial filtering in the linear receiver a chance to work. In the best case, the array response vectors (i.e. spatial signatures) of all streams are orthogonal to each other. In this case, the weight vectors that are simply matched to the two desired streams naturally suppress the interference and naturally give the highest SNR to the desired streams. For short-range LOS MIMO links, increased spacing can make the desired streams spatial signatures orthogonal to each other [91]. For an array with small element spacing, the interference signature will be nearly orthogonal to the desired signature when their respective angles of arrivals are sufficiently separated. In this case, the array can suppress the interference (implicit in the whitening process in our approach) with little SNR degradation to the desired stream, which is the case of less-correlated interference. However, as the DOA separation decreases, there will be more degradation to the desired stream SNR because of the inability of the array pattern to make a rapid (with respect to angle) transition between a peak and a null. Increased element spacing can help the correlated interference problem, because the pattern can make more rapid transitions.

With stream control, all throughput curves have *shapes* similar to those of Figure 51. Therefore, to save space, we show only the throughput values at the relatively high SNR of 21 dB, in the form of the bar charts in Figure 55. The first thing we notice is that stream control provides significant improvement in the throughputs. For instance, without stream control, the throughputs of antenna spacing 3λ in Confs. I to IV are 12.30, 6.02, 12.45, and 11.52 bits/s/Hz, respectively at 21 dB. Using stream control, the throughputs

are raised to 12.50, 27.86, 27.09, and 23.72 bits/s/Hz. In other words, the improvements are 1.62%, 362.6%, 117.7%, and 105.9% in these four configurations. The improvement is the largest for Conf. II, where the power of the interference on data link 1 is particularly large. In addition, the phenomenon of slope decreasing with increase of SNR in no-stream-control conditions is eliminated. With the spacing of 3λ, the curve slopes (not shown) in Confs. I to IV are 2.96, 3.94, 3.9, and 3.88 bits per 3dB at high SNR. The last three configurations almost achieve the ideal value of 4 bits per 3 dB, indicating that using stream control, all 4 data streams are available and contribute to the overall throughput. As a consequence, at higher SNR the influence of stream control will be even more significant.

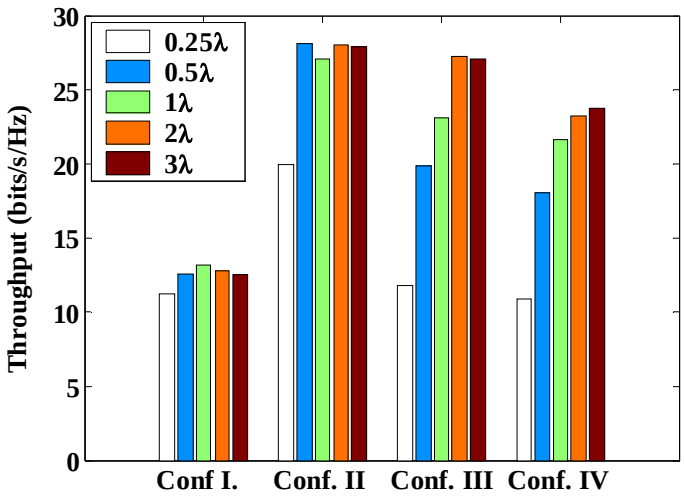

Figure 55: Throughputs of four configurations with stream control at SNR = 21 dB.

One may notice that with stream control the throughput of Conf. I is particularly small compared to the other three configurations, and Conf. II is the best. Yet without stream control, the opposite is true (see Figures 53 and 54). We can explain this reversal from the perspective of SNR and SINR in each configuration. Without stream control the throughputs are dominated by interference. Conf. I has the weakest interference and Conf.

II has the strongest. However, with stream control, Conf. II not only outperforms Conf. I but turns out to be the best among all configurations. When the stream control reduces the influence of interference, the throughput becomes dominated by the SNR. Assuming the SNR of the first receiver is 21dB, the SNR of the second receiver varies with configuration. In Conf. I, the SNR of the second receiver is only –2dB, whereas the SNRs of the second receivers in the other three configurations are 26dB, 26dB, and 20dB. Therefore, in Conf. I, only the first link (T2-R1) contributes much to the throughput, whereas in the other configurations, both links contribute.

After demonstrating the effect of stream control in multi-link networks, we now return to the subject of spatial correlation between the data and interference links. The throughputs of the configurations with less correlated interferences, Confs. I and II, tend to saturate when the antenna spacing achieves 0.5λ. On the other hand, for the highly correlated interference configurations, the throughputs keep increasing till the antenna spacing is larger than 2λ. This difference can be accounted for by the availability of LOS and the correlation level between the desired signal and the interference.

As we mentioned earlier, in Conf. I, the throughput is primarily contributed from the first link T2-R1 due to the extremely low SNR of the other data link. On the other hand, because of the low correlation, the interference link T7-R1 can be substantially suppressed with a small array aperture. Since the capacity of Link T2-R1 is sensitive to element spacing because of the existence of LOS as shown in Figure 51, one might expect the throughput with interference to be also sensitive to the element spacing. However, on the contrary, the measured throughput is *not sensitive* to the element spacing, as shown in Figure 55. The reason is that in Figure 51, all four data streams are

transmitted, therefore wide element spacing of the receive array is required to achieve full rank, which is equal to four. On the other hand, in Figure 55, only two data streams are transmitted; therefore, a rank of two can be achieved with relatively small array aperture. The measured results show that 0.5λ is sufficient to obtain a rank of two.

As for Conf. II, the throughput is not sensitive to element spacing because of the wide angular spread and the low correlation, as we expected. In Confs. III and IV, the spatial correlation is high because the LOS components of the desired and the interference links are available and almost overlapped. This highly correlated interference causes more degradation with smaller spacing because the receive array has less ability to resolve the clusters of critical paths. Wider antenna spacing allows better spatial resolution of signal and interference, and the throughputs achieve their no-interference values. This explains why the throughputs of Conf. III and IV are sensitive to element spacing. As shown in Figure 55, the throughput of Conf. III improves as much as 36.4% when the antenna spacing is increased from 0.5λ to 2λ at 21dB.

To sum up, the measurement results in this section demonstrate that stream control plays a critical role in the throughput of MIMO multi-user networks that do linear receiver processing, particularly when wide antenna spacing is employed, LOS is available, or the SNR is large. With stream control, half a wavelength spacing is usually sufficient when the correlation is low. Higher correlation causes more degradation at small spacing, while the difference becomes negligible at large spacing.

7.6 Capacity Enhancement by Adapting the Element Locations

7.6.1 Potential of Adaptive-Position Array

To investigate how the OL-MIMO channel capacity changes with the array geometry, and how much benefit we can get by adapting the element locations, we conducted an experiment to measure the channel matrix of a virtual array with finely separated elements. We made the measurements in the SARL. The Tx and the Rx arrays were placed at locations T3 and R4 in Figure 16. In the experiment, the transmitted signal was a single tone at 5.8 GHz. Let the notation (n_T, n_R) indicate the number of transmit (n_T) and receive (n_R) elements in the MIMIO channel. At both the Tx and Rx, we synthesized 61-element ULAs, with the sample spacing of 0.1λ. The channel matrices of a large number of unequally spaced arrays can be determined from the subsets of the measured (61,61) MIMO channel.

First, we investigate the capacity of the (4,4) MIMO link with unequally spaced arrays. The antenna locations of the Tx and Rx arrays are denoted as $\mathbf{x}_T = (x_{T1}, x_{T2}, x_{T3}, x_{T4})$ and $\mathbf{x}_R = (x_{R1}, x_{R2}, x_{R3}, x_{R4})$, respectively. To simplify the situation, at first we use the fixed uniform array at the Tx site, and allow only the second and third antennas of the Rx array to be changed. In other words, the antenna locations of both arrays are

$$\begin{aligned} \mathbf{x}_T &= (0, 2\lambda, 4\lambda, 6\lambda) \\ \mathbf{x}_R &= (0, x_{R2}, x_{R3}, 6\lambda) \end{aligned} \tag{109}$$

where

$$x_{R2} \in \{n \times 0.1\lambda \,|\, 2 \le n \le 59\}$$
$$x_{R3} \in \{m \times 0.1\lambda \,|\, n < m \le 60\} \tag{110}$$

Figure 56 shows the measured capacities of the MIMO system with varying x_{R2} and x_{R3} when SNR is 30 dB.

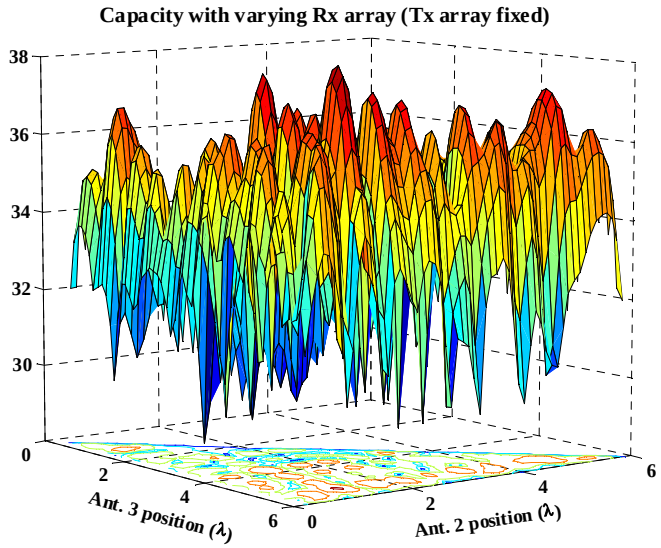

Figure 56: MIMO capacity with varying spacing in the Rx array.

According to the results, the capacity is 34.04 (bits/sec/Hz) for the single MIMO channel when the Rx array is uniform. The maximum capacity of 38.29 (bits/sec/Hz) is achieved when $\mathbf{x}_R = (0, 1.1\lambda, 5.3\lambda, 6\lambda)$, while the minimum capacity of 28.59 (bits/sec/Hz) occurred when $\mathbf{x}_R = (0, 0.6\lambda, 2.9\lambda, 6\lambda)$. When the second and third antennas in the Tx array are also changeable, the capacity can be further improved. In this case, the maximum capacity is 40.94 (bits/sec/Hz) when $\mathbf{x}_T = (0, 0.8\lambda, 3.3\lambda, 6\lambda)$ and $\mathbf{x}_R = (0, 1.1\lambda, 4.3\lambda, 6\lambda)$. In reference to (2) for the measured uniform linear array, adapting the two Rx elements or the four Tx and Rx elements yields SNR improvement of 3 dB or 5 dB, respectively.

It is of interest to see how the capacities of the arrays with adapted element locations compare to the ensemble of capacities that are possible with a uniform array. To measure the ensemble, we conducted another experiment where the Tx and Rx array platforms were in the same locations as the previous measurement. In this experiment, 6-element uniform linear arrays with antenna spacing 2λ were synthesized at both the Tx and Rx. Accordingly, nine (4,4) MIMO channels based on 4-element ULAs can be extracted from the acquired (6,6) channel matrix. The number of sample matrices is increased by repeating the measurements at 51 different frequencies with 2 MHz spacing, centered at 5.8 GHz. Therefore, we obtained $9\times51=459$ outcomes of the capacity of a (4,4) equally spaced arrays. Figure 57 shows the cumulative distribution function (CDF) of these outcomes, as well as the capacity CDF of the ideal channel which is simulated by 2000 trials of i.i.d. complex Gaussian MIMO channel matrix. The capacities of the arrays with adapted element locations are included as symbols. The capacities of the arrays with adapted element locations are included as symbols in Figure 57, which also includes the capacity CDF of the ideal channel which is simulated by 2000 trials of i.i.d. complex Gaussian MIMO channel matrix.

Notice that the maximum capacity (38.29 bit/sec/Hz) obtained by moving Rx antennas has surpassed the maximum *measured* capacity 37.67 of (4,4) ULAs. It is interesting to observe that by moving antennas at both ends the maximum capacity nearly coincides with the highest capacity of the ideal i.i.d MIMO channel. This means that for this given real multipath environment, enough variation of the channel matrix was induced to reach the extreme outcome by moving just 4 of the total of 8 elements. In

other words, this result suggests that, as the subsets of elements are moved in time, the resulting capacity has an ergodic variation.

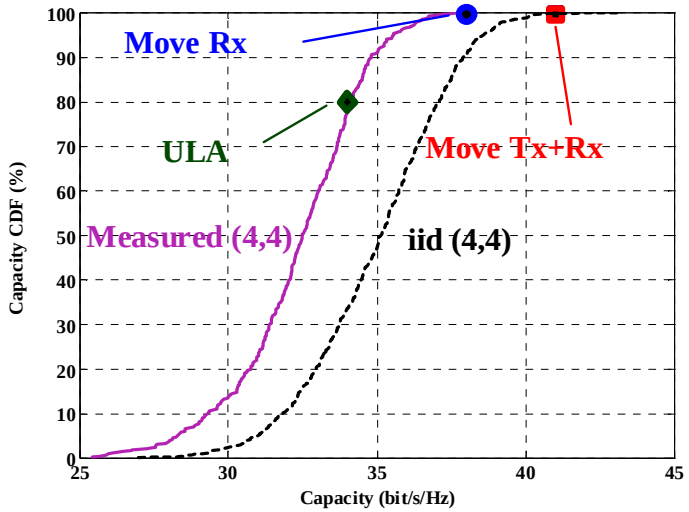

Figure 57: Comparison of unequally spaced MIMO with equally spaced and ideal MIMO channel capacities.

Figure 58 shows the singular value distribution and the antenna positions that achieve the maximum capacity by moving both arrays for SNR=30dB. We observe that the capacity enhancement results not only from the flatter distribution but also the increased receive power.

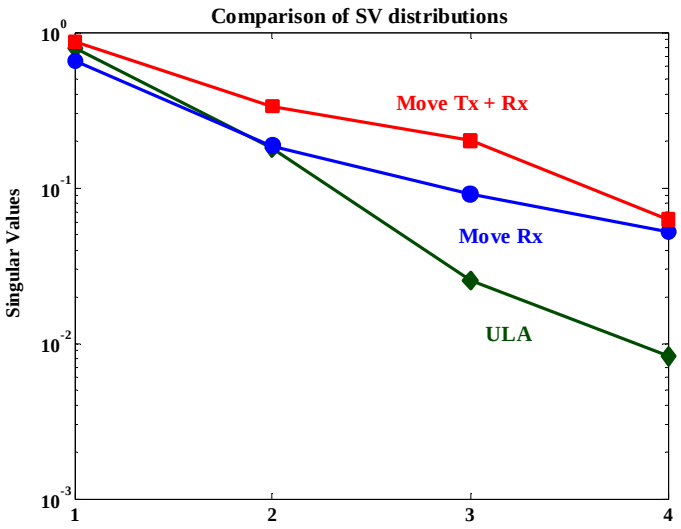

(a)

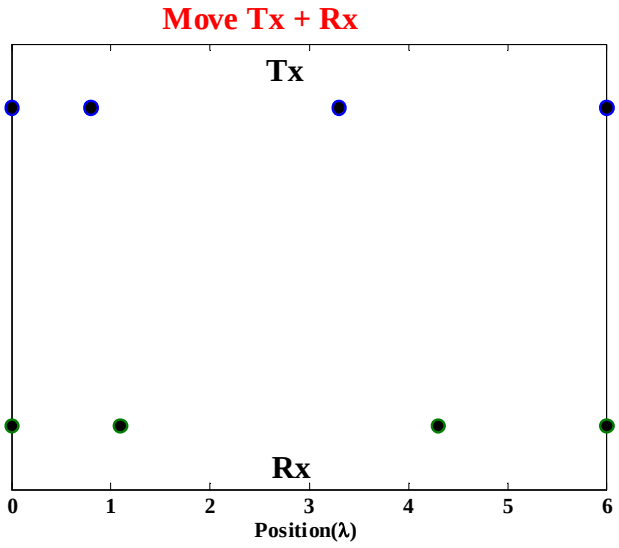

(b)

Figure 58: High SNR. (a) Singular value distribution and (b) Tx and Rx antenna locations.

Next we consider the low SNR condition. Assume the SNR = -10 dB, the maximum capacity by moving the Rx or both arrays are 0.85 and 1.28 bit/sec/Hz, and the capacity of ULA is 0.61 bit/sec/Hz. In Figure 59, we found that by moving both Tx and Rx the second singular value is more than 15 dB smaller than the first singular value,

making the channel matrix nearly rank one (the 4th antenna is fixed), thereby experimentally confirming the conclusions of [26].

We note that the optimal locations for the low SNR case could not be achieved practically because elements cannot be so close, nor could mutual coupling effects be ignored when elements become close.

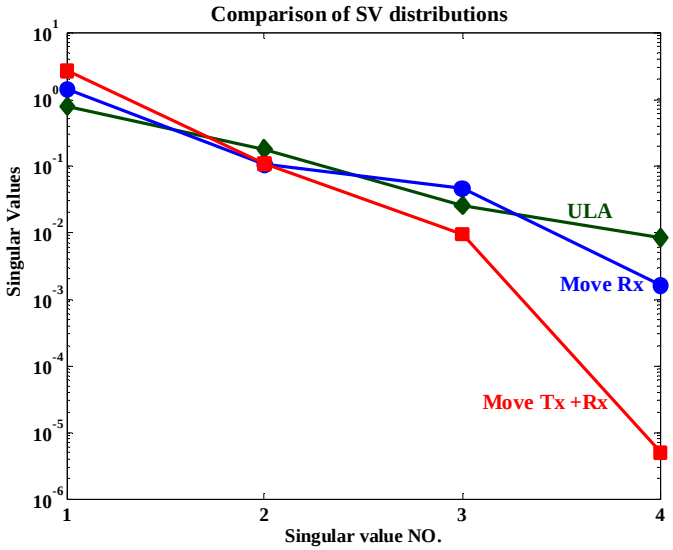

(a)

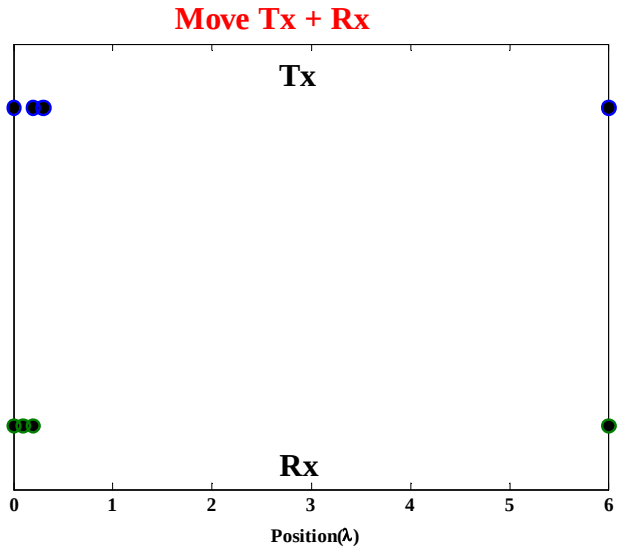

(b)

Figure 59: Low SNR. (a) Singular value distribution and (b) Tx and Rx antenna locations.

7.6.2 Implementation of Adaptive-Position Array

We next use the steepest descent algorithm to iteratively move all of the transmit and receive antennas to achieve a local maximum of the capacity. The detailed steps are as follows:

(1) Decide the initial locations of Tx and Rx. In the experiment, the Tx and Rx are ULA with four antennas and the antenna spacing = 2λ.

(2) Calculate the MIMO channel matrix and its capacity.

(3) Move each antenna slightly, e.g., 0.01λ to calculate the capacity gradient. (each real array is emulated by virtual array)

(4) Move the antennas along the direction of gradient. Use quadratic interpolation method [92] to determine the optimum step size.

(5) Repeat steps 2-4 until the step size is less than specified value. The specified value is $0.0006\ \lambda$ in the experiment.

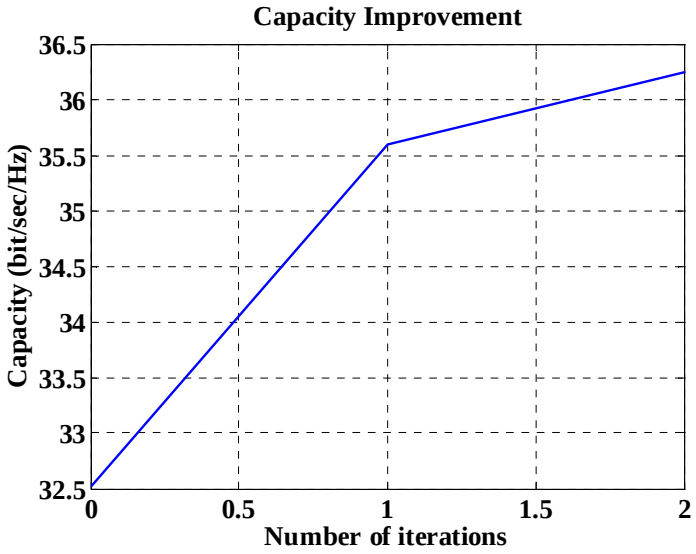

(a)

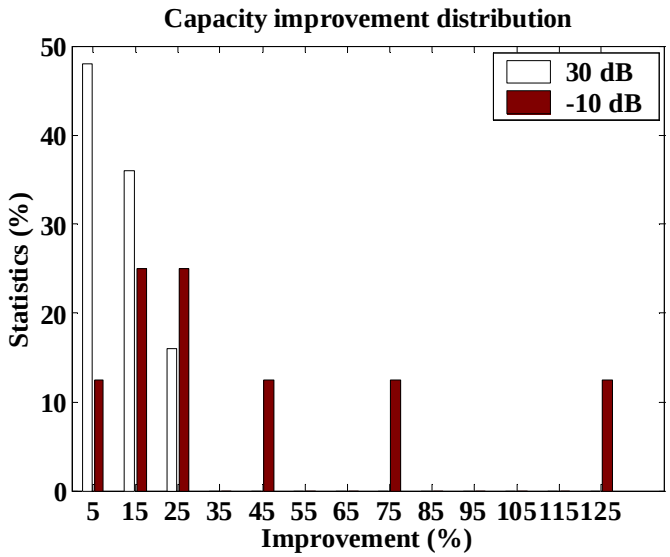

(b)

Figure 60: Capacity improvement using adaptive-position array at high SNR (30 dB). (a) An example, which has 9.2 % capacity improvement at the first iteration and totally 11.6 % capacity improvement. (b) Capacity improvement statistics of 25 experimients.

The experiment results for SNR = 30 dB are shown in Figure 60. Figure 60(a) shows an example where the capacity converges after two iterations. In this example, the improvement is about 9.2 % from the first iteration, and the total improvement is about 11.6%. Histograms of percent improvement in capacity resulting from adapting the element locations are shown in Figure 60(b). The white and black histograms correspond

to SNRs of 30dB and –10dB, respectively. Each histogram is based on 25 runs of the experiment, where the initial element locations in each run of experiment were progressively shifted by 2λ in the direction perpendicular to the array to obtain independent outcomes. Overall, the improvements range from 0.09 to 7.29 bit/sec/Hz (or 0.24% to 23.03%), and the average improvement is 3.35 bit/sec/Hz (10.19%). The maximum required number of iterations is 4, and the percentages of the experiments that need 1 to 4 iterations are 48%, 32%, 16%, and 4%, respectively. In other words, more than 80% of the experiments achieve the local maximum within 2 iterations. For the low SNR case (-10 dB), the minimum and maximum improvements are 0.05 bit/sec/Hz (9.3%) and 0.67 bit/sec/Hz (129.05%), respectively. The average improvement is 21.3%. The maximum required iterations is 5. 62.5% of the experiments need only one iteration. The percentages of the experiments that need 2, 3, and 5 iterations are the same and equal 12.5%. Therefore, more than 70% of the experiments achieve the local maximum within 2 iterations.

7.7 Chapter Summary

Interference is generally present in the practical environment for wireless communications. Using the measured data obtained in the Georgia Tech Residential Laboratory, we showed the impact of interference to the performance of MIMO channels. The measurement results showed that wider antenna spacing is beneficial to the MIMO capacity of the channel without interference, but not for the channel with interference unless proper stream control is applied. For the less correlated interference, the throughput of the two-link network with stream control tends to saturate at 0.5λ, while

for the highly correlated interference, the throughput is sensitive to the antenna spacing and up to 36% of improvement can be achieved by increasing the spacing from 0.5 to 2λ. We noted that our conclusion that antenna spacing matters disagrees with the conclusions of [93]. The reason may be because of differing wall construction in the two measurement environments [94]. The walls environment in our measurement were constructed of wood and plasterboard, whereas the walls in [93] were of masonry materials. Several experiments were conducted to exploit the potential of capacity enhancement by adaptively moving the antenna locations. The OL-MIMO channel capacity improvement in the measurement results is up to 23.03% at high SNR and 129.05% at low SNR with a small number of iterations. One problem of the adaptive-position array is that the channel must be static during the adaptation in order to successfully achieve the local maximum capacity. However, this scheme can still be employed in the applications where the environments change relatively slowly. With the advancement of Micro-Electro-Mechanical systems (MEMs) [95], such adaptive positioning may be practical in the future.

Chapter 8

Beam Selection And Antenna Selection

8.1 Introduction

As mentioned in preceding chapters, MIMO channel can be improved by selecting the MIMO antenna elements from among a larger set of elements at one or both ends of a link [37,38]. An older technology, the switched-beam RF beamforming, which has simple implementations like the Butler matrix [40,41], have drawn tremendous attention in the arena of cellular systems because of their superior interference suppression feature and the space division multiple access (SDMA) capability. The theories of antenna and beam selection have been described in Section 2.1. Here we compare the performances of beam selection and antenna selection over a few real indoor environments that differ in terms of the existence of LOS, the channel bandwidth, the presence of interference, and the correlation between the intended signal and the interference. The measured data used here are a subset of the data used in Chapter 7, in particular only the arrays with half a wavelength antenna spacing are used. In the following sections, we will compare their performances in narrowband and wideband channels.

8.2 Narrowband Channels

8.2.1 No Interference

We consider links with and without LOS, or Link T2-R1 and Link T7-R2, respectively. First, we discuss the LOS results, shown in Figure 61. The label "All Antennas," indicates the condition when all four antennas are employed. Its results are used as a reference. The "No selection" curve is the performance of the system when the first two antennas are used at transmit and receive ends; in this case, $\mathbf{H}_{ant}$ and $\mathbf{H}_{beam}$ are 2×2 matrices. First, we observe that "All antennas" has the best performance in high SNR range because channel rank is larger than the others. Turning to the other curves in Figure 61, we observe that at 14 bits/s/Hz, beam selection outperforms antenna selection and no selection by 2.5 and 7.5 dB, respectively.

When the selection is only applied at the transmit end, $\mathbf{H}_{ant}$ and $\mathbf{H}_{beam}$ become 4×2 matrices. The capacity slopes (not shown) of these four methods is the same, but the gaps between beam selection and the other two selection methods are reduced to 1.5 and 4 dB respectively at 14 bits/s/Hz.

We also considered the frequency of usage of beams and antennas. The receive beam usages in the beam selection scheme for Beams 1 to 4 are 50%, 36.27%, 10.29%, and 3.43%, respectively. Evidently, the LOS and most of the multipath are contained in Beams 1 and 2. The other two beams, Beams 3 and 4, are hardly used. For the antenna selection method, each receive antenna is almost evenly used. The antenna usage distribution is 21.08%, 27.70%, 25.49%, and 25.74%. The reason for this is as follows. Antenna selection depends on the small-scale fading, which varies with frequency and

small spatial displacements. Therefore, the selected antennas at one frequency and subarray position are usually not the best choices for some other frequencies and positions if the two frequencies are separated by more than one coherence bandwidth or the two distances are separated by more than the coherence distance. This explains why the usage of antennas is close to uniformly distributed since the outcomes of channel matrices are sampled from the frequency bandwidth of 500 MHz and the subarrays are displaced by multiples of $\lambda/2$. Beam selection, on the other hand, depends on the path angles of arrival, which are the same for entire frequency band and small spatial displacements. This feature should make beam selection more attractive for the wideband application, which will be discussed in the next section.

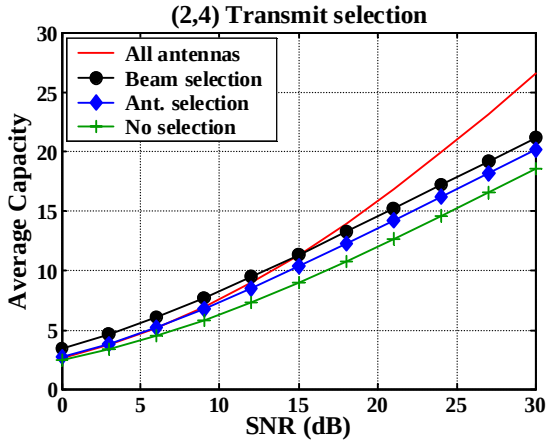

(a) Transmit selection

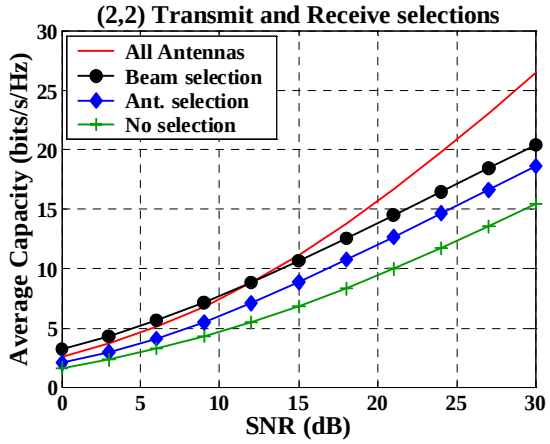

(b) Transmit & Receive selection

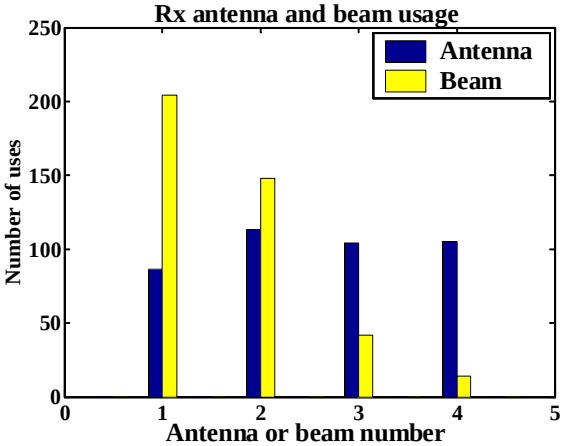

(c) Antenna and beam usage

Figure 61: With LOS (Link T2-R1) and no interference: (a) Transmit selection. (b) Transmit & Receive selection. (c) Antenna and beam usage.

Figure 62 shows the measured results for channel T7–R2 where the LOS is not available. In this case, the performance difference between beam and antenna selection is

reduced primarily because the angular spread is increased. We add that the receive beam usage distribution (20.6%, 12.5%, 26.96%, 39.95%) becomes more uniform than in the preceding example because the wide angular spread is across more than two beams. The receive antenna usage is still close to uniformly distributed.

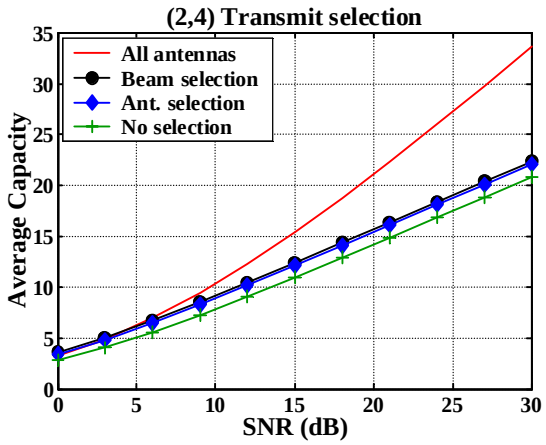

(a) Transmit selection

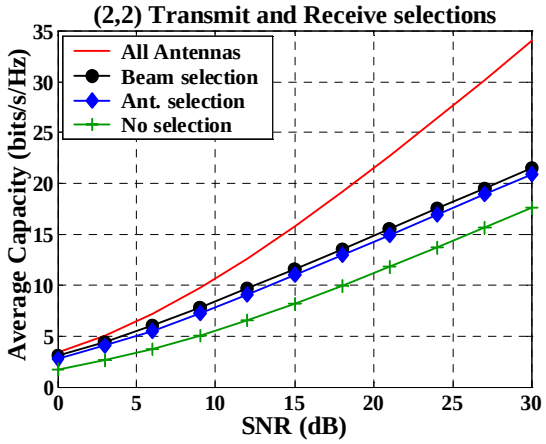

(b) Transmit & Receive selection

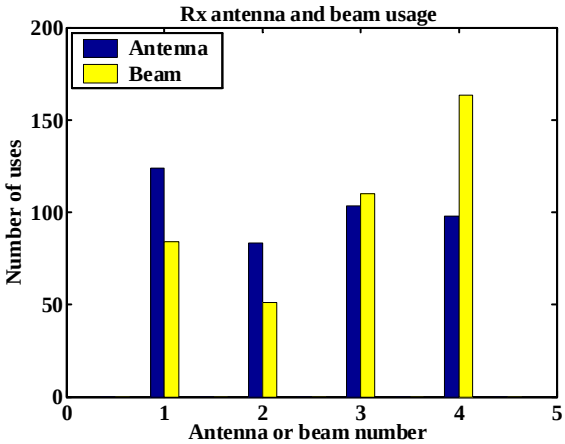

(c) Antenna and beam usage

Figure 62: No LOS (Link T7-R2) and no interference: (a) Transmit selection. (b) Transmit & Receive selection. (c) Antenna and beam usage.

8.2.2 With Interference

In the following discussion, the equal SINR normalization is performed for the capacity calculation. The throughputs in Conf. I, channels with less-correlated interferences, are demonstrated in Figure 63, where "T-Beam" ("T-Antenna") means that two beams (antennas) are optimally selected at the transmit site only, and "TR-Beam" ("TR-Antenna") means that two beams (antennas) are optimally selected at each of the Tx and Rx ends. The curve for "All Antennas," which indicates the condition when all four antennas are employed, is used as a reference. "No selection" curve shows the performance of the system when the first n_T or n_R antennas are used at transmit and receive ends.

The highest three curves in Figure 63 show the result of stream control [35]; no receiver is overwhelmed by too many streams. The slope of both transmit beam and transmit antenna selection is about 4 bits/3dB at high SNR, which is equal to the theoretical slope of systems with four data streams. T-Beam selection outperforms T-Antenna selection and no selection by less than 1 dB and more than 4 dB, respectively, at 20 bits/s/Hz.

When selection is applied to both ends, the performance degrades because each receiver's two channels are overwhelmed by four streams; this is the situation for the lowest three curves. It corresponds to a lack of stream control, which could occur because stream control requires extra signaling in a network, and therefore may not be used. Under this circumstance, the difference between the beam and antenna selection methods is increased to 6 dB, and the performance of no selection is far behind them.

The “All Antennas” case also corresponds to a situation of receiver overload, with eight streams falling on receivers that each have only four antennas. We believe that the “All Antennas” curve is higher than the “TR” curves because the “All Antennas” array aperture is larger.

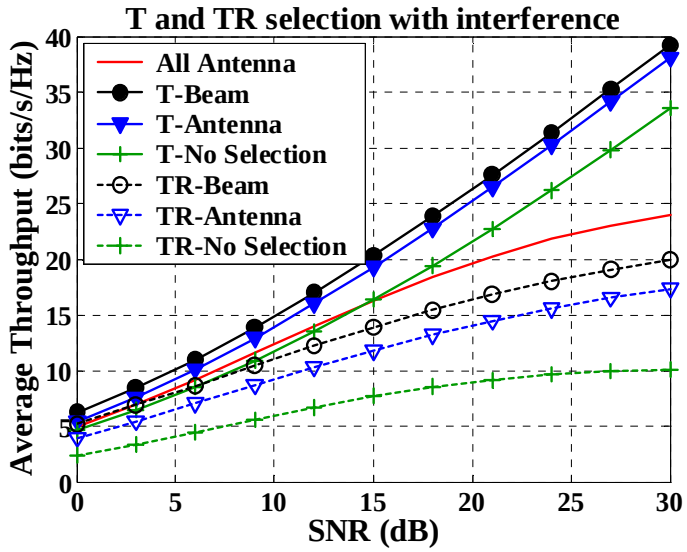

(a)

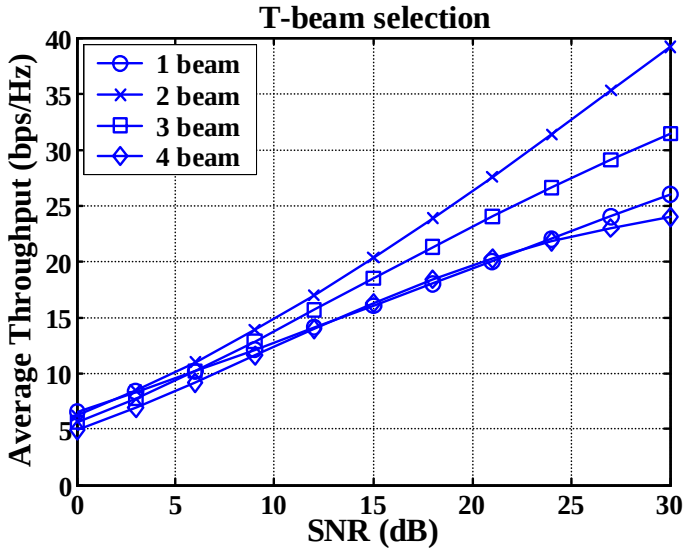

(b)

Figure 63: Narrowband channel with less correlated interference (T2−R1,T7−R2): (a) Throughput of various methods. (b) Performances with various numbers of beams.

When the interference is highly correlated with the signal, as in Figure 64, the overall throughput is decreased compared to the previous uncorrelated interference case. In this condition, the slope is reduced to 3bits/3dB at high SNR range. However, the relative performance difference among various methods discussed so far is about the same, and two-beam system still has the best performance.

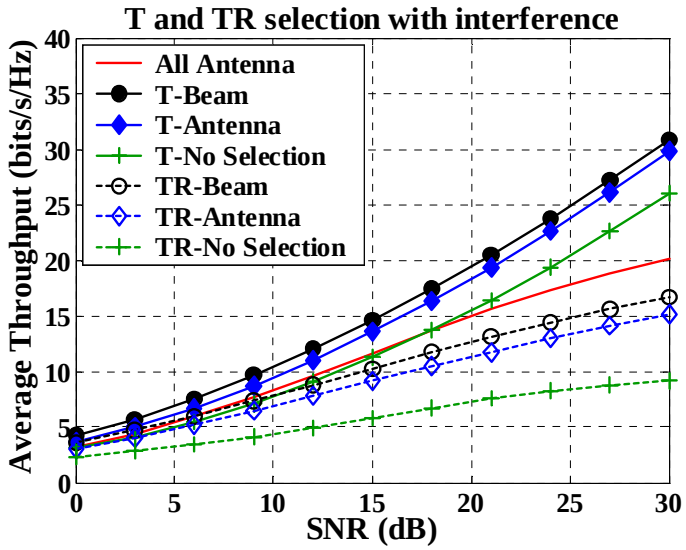

(a)

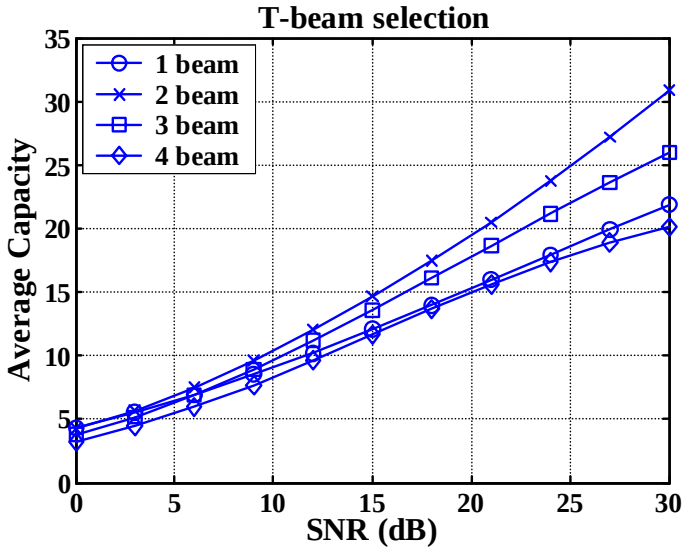

(b)

Figure 64: Highly correlated interference (T3–R1,T4–R2): (a) Throughput of various methods. (b) Performances with various numbers of beams.

8.3 Wideband Channels

The robustness of the beam selection method to frequency selection in wideband channels was hypothesized in the previous sections. We calculate the open-loop capacity of the wideband channels by averaging the flat-fading channel capacity over the 500 MHz bandwidth. The throughputs in wideband channels are shown in Figure 65.

The difference between T-Beam selection and T-Antenna selection is only about 1.5 dB at 20 bits/s/Hz for the channel with less correlated interference. With highly correlated interference, the difference is 1.8 dB at 20 bits/s/Hz, but the slopes for T-Beam and T-Antenna selection methods are reduced to 3bits/3dB. When the selection is employed at both ends, the performance difference increases to more than 15 dB at 10 bits/s/Hz. For the highly correlated interference, the difference is about 8 dB at 10 bits/s/Hz when selection is employed at both ends. Although TR-Beam is much better than TR-Antenna because of the interference suppression provided by the beam patterns, TR-Beam still suffers for lack of stream control. Overall, the throughput of selection at transmit end is better than the selection at both ends. However, under stream control, the difference between beam and antenna selection seems surprisingly small for such a wide bandwidth in the indoor environment. One possible reason for the small difference is the wide beamwidth caused by the small number of antennas, which impacts the interference suppression capability of the Butler matrix. The effect of increasing the number of antennas needs further investigation.

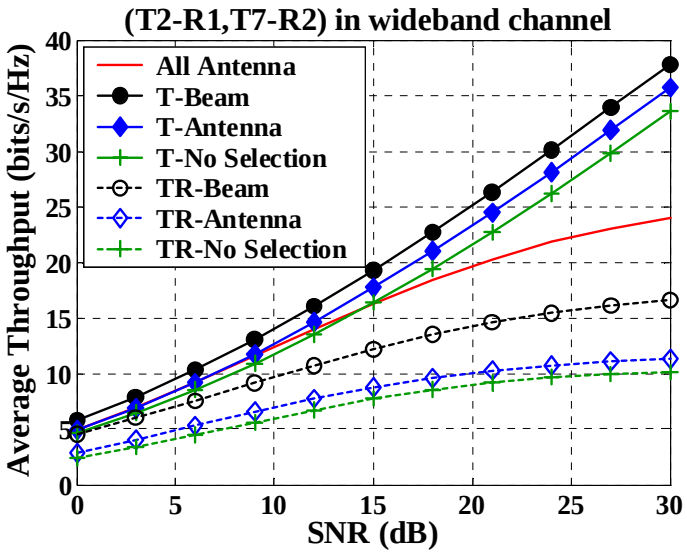

(a) Less correlated interference

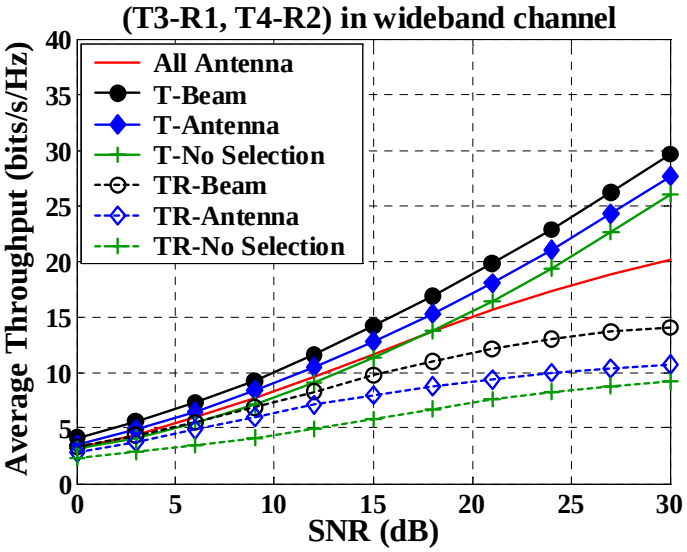

(b) Highly correlated interference

Figure 65: Wideband channels with (a) less correlated interference and (b) highly correlated interference.

8.4 Chapter Summary

When linear receiver processing is used, stream control is required to reach the highest network throughputs. Beam and antenna selection are two approaches of stream control. The comparison of beam selection and antenna selection in the (4,4) MIMO

system was demonstrated. These results are based on measured data from an indoor environment at 5.8 GHz. Selection of two antennas or beams from a total of four is considered. With stream control, and assuming lossless RF components, selection provides an improvement over no selection, and beam selection is slightly better than antenna selection. However, the SNR improvements of selection over non-selection are never more than 4dB. Since the insertion losses of real switches and beamformers could combine to be that much or more [96], there is little justification for using selection of two from four under stream controlled conditions. On the other hand, when there is no stream control, the SNR improvements of selection, and particularly beam selection, would more than compensate the insertion losses.

Chapter 9

Conclusions and Suggested Future Work

MIMO technology, which is expected to be applied to wireless communications of the next generation in the near future, has drawn much attention because it provides unprecedented channel capacity. Although MIMO technology has good performance in ideal i.i.d Rayleigh fading channels, various factors in the real environment could cause significant performance degradation. These factors include, for example, the array geometry, availability of the LOS component, external interference, and spatial correlation between the data and interfering links. In this dissertation, we have investigated the effects of the above factors on the performance of MIMO channels in several indoor environments around 5.8 GHz based on channel measurements, and compared the performance of various techniques that can be employed in combination with MIMO technology. The primary contributions are summarized as follows:

Propagation models for short-range MIMO channels: The plane wave propagation channel model has been used extensively in array signal processing. Although it has been pointed out that the plane wave assumption may result in the underestimation of the performance of MIMO channels, it is still employed by many research groups. Based on ray tracing, we have explored the underestimation phenomenon in the free space channel as well as channels with multipath. We have shown that for short-range MIMO, the spherical wave model is more appropriate than the

plane wave model for MIMO systems when the LOS is present, especially when the element spacing is larger. A threshold distance, under which the channel capacity is underestimated by 50% for uniform linear array in free space channels, is provided. We also show that, unlike the plane wave model, the spherical wave model enables the performance of the short-range LOS MIMO system to be significantly improved by properly adjusting the DOA, DOD, and the array geometries. In particular, capacity can be dramatically improved by increasing the antenna spacing at both ends of the link. The results suggest that greater-than-single wavelength element spacing should be considered for non-handheld user platforms in WLAN applications.

Detection of number of sources algorithms: We have proposed two novel number-of-sources detection algorithms. The purpose of these two algorithms is to provide robust detection for the applications where measurement distortion may be caused by non-uniform element spacing or varying element gains. We have shown that when the smoothing technique is utilized, these measurement distortions result in eigenspace estimation error, which causes the popular and traditional detection method MDL to fail. Although the first algorithm, REE, is robust, it has the disadvantage of huge computational complexity when the array size is large because estimation based on each assumed number is involved. The second algorithm, VTRS method, provides the advantage of robustness without intensive computation because estimation is not involved. Therefore, the VTRS algorithm is particularly suitable for real-time application under tough environment such as outdoor wireless communications.

Searching for appropriate path parameter estimation algorithms: For MIMO channels, the difficulty of parameter estimation is increased significantly compared to the

SISO, SIMO, and MISO channels, primarily because of the high complexity of the measurement system and larger number of channel parameters. We have implemented a 3D MIMO channel sounding testbed based on the virtual antenna array scenario to reduce the cost and complexity of the measurement system. Using the measurement system, we compare the accuracy of various versions of estimation based on ESPRIT algorithm. We conclude that the separate delay estimation followed by joint DOA-DOD estimation has better performance than sequential estimation, where the estimation error is accumulated in each separate estimation.

Exploitation of the effect of element spacing: We have investigated the effect of element spacing to the performance of MIMO channels without interference, and the throughput of four-node MIMO networks with interference. Without interference, the performance is sensitive to the element spacing when the LOS component is present. While this sensitivity is reduced when the LOS component is obstructed, the measurements in the Residential Laboratory have shown an average of 30% capacity improvement by increasing the element spacing from 0.5λ to $3\ \lambda$. When the interference is present, the increase of element spacing no longer guarantees better performance unless stream control is applied. We have shown that stream control strongly impacts the throughput of a MIMO multi-user network, particularly when wide antenna spacing is employed, LOS is available, or the SNR is large. We also investigated the effect of different levels of correlation between the data links and interfering links. It appears that higher-level of correlation causes more degradation at small spacing, while the difference becomes negligible at large spacing. Furthermore, the adaptive-position array is proposed to improve the performance of MIMO channels by iteratively varying the element

locations based on the steepest descent algorithm. The adaptive-position array has been tested by our measurement testbed and the measurement results show that the improvement is up to 23% at high SNR and 129% at low SNR.

Comparison of beam selection and antenna selection methods: We have compared the performance of beam selection and antenna selection using (4,4) MIMO channels. Beam selection appears to outperform antenna selection significantly when the selection is applied to both ends of the communication links and the receivers are overwhelmed from lack of stream control. However, the beam selection is only slightly better than the antenna selection when the stream control is applied, i.e. the selection is applied only on the transmit ends. Stream control is observed to have a strong impact on network performance over measured channels. As a consequence, the advantage of beam selection over antenna selection is diminished compared to the contribution of stream control. One possible reason to account for the minute difference is the wide beamwidth of the small array. When the number of antennas is increased, the beamwidth will be reduced and provide better interference cancellation. The effect of larger array will be investigated in the future.

Several other issues deserve attention in the future research. Although we have investigated several factors that affect the performance of MIMO channels, the antenna polarity, mutual coupling effects, and Doppler effects were excluded because of limitations of our virtual antenna array structure. These factors may also play important roles and need to be further explored using real antenna arrays. Another issue is that, in this dissertation, the performances of MIMO channels were evaluated based on Shannon's channel capacity, and no specific modulation and receiver signal processing

approach were assumed. A common and more practical criterion for the evaluation of a communications system is the bit error rate (BER). The conclusions of this dissertation should be tested using BER and on system prototypes.

BIBLIOGRAPHY

[1] G.J. Foschini and M.J. Gans, "On limits of wireless communications in a fading environment when using multiple antennas," *Wireless Personal Communications*, pp.311-335, 1998.

[2] G.G. Raleigh and J.M. Cioffi, "Spatio-temporal coding for wireless communication," *IEEE Trans. Communications*, vol. 46, pp. 357-366, Mar. 1998.

[3] J.H. Winters, "On the capacity of radio communication systems with diversity in Rayleigh fading environment," *IEEE Journal on Selected Areas in Communications*, pp. 871-878, Jun. 1987.

[4] D. Shiu, G.J., Foschini, M.J. Gans, and J.M. Kahn, "Fading correlation and its effect on the capacity of multielement antenna systems," *IEEE Trans. Communications*, vol. 48, pp. 502-513, Mar. 2000.

[5] D.W. Bliss, K.W. Forsythe, A.O. Hero, and A.F. Yegulalp "Environmental issues for MIMO capacity," *IEEE Trans. on Signal Processing*, pp.2128-2142, Sep. 2002.

[6] D. Gesbert, H. Bolcskei, D. Gore, and A. Paulraj, "MIMO Wireless Channels: Capacity and Performance Prediction," *GLOBECOM*, vol.2, pp. 1083-1088, 2000.

[7] D.P. Palomar, J.R. Fonollosa, M.A. Lagunas, "Capacity Results of Spatially Correlated Frequency-Selective MIMO Channels in UMTS," *IEEE Vehicular Technology Conference*, vol.2, pp. 553-557, Fall 2001.

[8] R.S. Blum, "Analysis of MIMO capacity with interference," *IEEE International Conference on Communications*, vol. 5, pp. 2991-2995, Apr. 2003.

[9] R.S. Blum, "MIMO capacity with antenna selection and interference," *IEEE International Conference on Acoustics, Speech, and Signal Processing*, vol. 4, pp. IV_824-IV_827, Apr. 2003.

[10] R.S. Blum, "MIMO capacity with interference," *IEEE Journal on Selected Areas in Communications*, vol. 21, pp. 793-801, Jun. 2003.

[11] R.B. Ertel, P.Cardieri, K.W. Sowerby, T.S. Rappaport, and J.H. Reed, "Overview of spatial channel models for antenna array communication systems," *IEEE Personal Communications*, pp. 10-22, Feb. 1998.

[12] R.O. Schmidt, *A signal Subspace Approach to Multiple Emitter Location and Spectral Estimation*, Ph.D. thesis, Standford Univ., Standford, CA, Nov. 1981.

[13] R. Roy, and T. Kailath, "ESPRIT-Estimation of signal parameters via rotational invariance techniques," *IEEE Trans. on Acoustics, Speech, and Signal Processing*, vol.37, pp. 984-995, Jul., 1989.

[14] M. Steinbauer, D. Hampicke, G. Sommerkorn, A. Schneider, A.F. Molisch, R. Thoma, E. Bonek, "Array measurement of the double-directional mobile radio channel," *IEEE Vehicular Technology Conference*, pp. 1656-1662, 2000.

[15] A.F. Molisch, M. Steinbauer, M. Toeltsch, E. Bonek, R.S. Thoma, "Capacity of MIMO systems based on measured wireless channels," *IEEE Journal on Selected Areas in Comm.*, vol. 20, NO. 3, pp. 561-569, Apr. 2002.

[16] A. Richter, D. Hampicke, G. Sommerkorn, R.S. Thoma, "Joint estimation of DOD, time-delay, and DOA for high-resolution channel sounding," *IEEE Vehicular Technology Conference*, pp. 1045-1049, 2000.

[17] H. Akaike, "A new look at the statistical model identification," *IEEE Trans. Automat. Contr.*, vol. AC-19, no. 6, pp. 716-723, Dec. 1974.

[18] J. Rissanen, "Modeling by shortest data description," *Automatica*, vol. 14, pp. 465-471, 1978.

[19] M. Wax, and T. Kailath, "Detection of signals by information theoretic criteria," *IEEE Trans. ASSP*, vol. 33, pp. 387-392, Apr. 1985.

[20] D.H. Johnson and D.E. Dudgeon, *Array signal Processing, Concepts and Techniques*, Prentice Hall, 1993.

[21] D.T. Paris, *Basic Electromagnetic Theory*, McGraw-Hill Book, 1969.

[22] P.W. Wolniansky, G.J. Foschini, G.D. Golden, R.A. Valenzuela, "V-BLAST: an architecture for realizing very high data rates over the rich-scattering wireless channel," *URSI International Symposium on Signals, Systems, and Electronics*, pp. 295-300, Sept. 29 – Oct. 2, 1998.

[23] S.M. Alamouti, "A simple transmit diversity technique for wireless communications," *IEEE Journal on Select Areas in Communications*, vol. 16, pp. 1451-1458, Oct. 1998.

[24] J.G. Proakis, *Digital Communications, 2nd edition*, McGraw-Hill, 1989.

[25] N. Chiurtu and B. Rimoldi, "Varying the antenna locations to optimize the capacity of multi-antenna Gaussian channels," *IEEE International Conference on Acoustics, Speech, and Signal Processing*, vol. 5, pp. 3121-3123, 2000.

[26] N. Chiurtu, B. Rimoldi, and E. Telatar, "On the capacity of multi-antenna Gaussian channels," *IEEE International Symposium on Information Theory*, pp. 53, Jun. 2001.

[27] A. Abdi and M. Kaveh, "A space-time correlation model for multielement antenna systems in mobile fading channels" *IEEE Journal on Selected Areas in Communications*, vol. 20, Apr. 2002.

[28] J.W. Wallace, A. Jensen, A.L. Swindlehurst, and B.D. Jeffs, "Experimental characterization of the MIMO wireless channel: Data acquisition and analysis," *IEEE Trans. Wireless Communications*, vol. 2, pp. 335-343, Mar. 2003.

[29] V. Pohl, V. Jungnickel, T. Haustein, and C.V. Helmolt, "Antenna spacing in MIMO indoor channels," *IEEE Vehicular Technology Conference*, vol.2, pp. 749-753, Spring 2002.

[30] D. Chizhik, F. Rashid-Farrokhi, J. Ling, and A. Lozano, "Antenna separation and capacity of BLAST in correlated channels," *IEEE Antenna and Propagation for Wireless Communications Conference*, pp. 183-185, 2003.

[31] C-N. Chuah, G.J. Foschini, R.A. Valenzuela, D. Chizhik, J. Ling, and J.M. Kahn, "Capacity growth of multi-element arrays in indoor and outdoor wireless channels," *IEEE Wireless Communications and Networking Conference*, vol. 3, pp. 1340-1344, 2000.

[32] L. Schumacher, K.I. Pedersen, and P.E. Mogensen, "From antenna spacings to theoretical capacities – guidelines for simulating MIMO systems," *The 13th IEEE International Symposium on Personal, Indoor, and Mobile Radio Communications*, vol.2, pp. 587-592, Sep. 15-18, 2002.

[33] S. Catreux, P.F. Driessen, and L.J. Greenstein, "Simulation results for an interference-limited multiple-input multiple-output cellular system," *IEEE Communication Letters*, vol.4, pp. 334-336, Nov. 2000.

[34] M.F. Demirkol, and M.A. Ingram, "Power-controlled capacity for interfering MIMO links," *IEEE Vehicular Technology Conference*, vol.1, pp. 187-191, Fall 2001.

[35] M.F. Demirkol, and M.A. Ingram, “Control using capacity constraints for interfering MIMO links, ” *IEEE Personal, Indoor, and Mobile Radio Communications*, vol.3, pp. 1032-1036, 2002.

[36] M.F. Demirkol and M.A. Ingram, “Stream control in networks with interfering MIMO links,” *Proc. of IEEE Wireless Communications and Networking Conference*, Mar. 2003.

[37] R.W. Heath, S. Sandhu, and A. Paulraj, “Antenna selection for spatial multiplexing systems with linear receivers,” *IEEE Communications Letters*, vol. 5, pp. 142-144, Apr. 2001.

[38] D. Gore and A. Paulraj, “Space-time block coding with optimal antenna selection,” *IEEE International Conference on Acoustics, Speech, and Signal Processing*, vol. 4, pp. 2441-2444, 2001.

[39] R.S. Blum and J.H. Winters, “On optimum MIMO with Antenna Selection,” *IEEE International Conference on Communications*, vol. 1, pp. 386-390, Apr. 2002.

[40] J.C. Liberti, Jr. and T. S. Rappaport, *Smart Antennas for Wireless Communications: IS-95 and Third Generation CDMA Applications*, Prentice Hall PTR, 1999.

[41] R.J. Mailloux, *Phased Array Antenna Handbook*, Artech House, 1994.

[42] M. Viberg, and H. Krim, “Two decades of statistical array signal processing,” *IEEE Signals, Systems, & Computers*, vol.1, pp. 775-777, 1997.

[43] H. Krim and M. Viberg, “Two decades of array signal processing research,” *IEEE Signal Processing Magazine*, vol. 13, pp. 67-94, Jul. 1996.

[44] B.D. Van Veen and K.M. Buckley, "Beamforming: A Versatile Approach to Spatial Filtering," *IEEE ASSP Magazine*, pp. 4-24, Apr. 1988.

[45] A.J. Barabell, “Improving the resolution performance of eigenstructure-based direction-finding algorithms,” in *Proceeding ICASSP*, Boston MA, pp. 336-339, 1983.

[46] B.D. Rao and K.V.S. Hari, “Performance analysis of root-MUSIC,” *IEEE Trans. on Acoustics, Speech, and Signal Processing*, vol. 37, pp. 1939-1949, 1989.

[47] M. Haardt, and J.A. Nossek, "Unitary ESPRIT: How to obtain increased estimation accuracy with a reduced computational burden," *IEEE Trans. Signal processing*, vol. 43, pp. 1232-1242, May 1995.

[48] M.D. Zoltowski, M. Haardt, and C.P. Mathews, "Closed-form 2-D angle estimation with rectangular arrays in element space or beamspace via unitary ESPRIT," *IEEE Trans. Signal processing*, vol. 44, pp. 316-328, Feb., 1996.

[49] M. Haardt, and J.A. Nossek, "Simultaneous Schur decomposition of several nonsymmetric matrices to achieve automatic pairing in multi-dimensional harmonic retrieval problems." *IEEE Trans. Signal Processing*, vol. 46, pp. 161-169. Jan. 1998.

[50] H. Saarnisaari, "TLS-ESPRIT in a time delay estimation," *IEEE Vehicular Technology Conference*, vol. 3, pp. 1619-1623, May 1997.

[51] A-J. Van Der Veen, M.C. Vanderveen, A. Paulraj, "SI-JADE: an algorithm for joint angle and delay estimation using shift-invariance properties," *IEEE Signal Processing Advances in Wireless Communication*, pp. 161-164, Apr. 1997.

[52] A-J. Van Der Veen, M.C. Vanderveen, A. Paulraj, "Joint angle and delay estimation using shift-invariance techniques," *IEEE Trans. Signal Processing*, vol. 46, pp. 405-418, Feb. 1998.

[53] K-H. Huarng and C-C. Yeh, "A unitary transformation method for angle-of-arrival estimation," *IEEE Trans. on Acoustics, Speech, and Signal Processing*, vol. 39, pp. 975-977, Apr. 1991

[54] J.E. Evans, J.R. Johnson, and D.F. Sun, "Applications of advanced signal processing techniques to angle of arrival estimation in ATC navigation and surveillance systems," *Tech. Rep. Lincoln Lab.*, MIT, 1982.

[55] T.J. Shan, M. Wax, and T. Kailath, "On spatial smoothing for direction-of-arrival estimation of coherent signals," *IEEE Trans. Acoust. Speech, Signal Processing*, vol. ASSP-34, pp. 806-811, Aug. 1985.

[56] T-J. Shan, A.A. Paulraj, and T.Kailath, "On smoothed rank profile tests in eigenstructure methods for directions-of-arrival estimation," *IEEE Trans. Acoustics, Speech, and Signal Processing*, vol. ASSP-35, pp. 1377-1385, Oct. 1987.

[57] A. Kuchar, J. Rossi, E. Bonek, "Directional macro-cell channel characterization from urban measurements," *IEEE Trans. on Antennas and Propagation*, vol. 48, pp. 137-146, Feb. 2000.

[58] M. Wax and I. Ziskind, "Detection of the number of coherent signals by the MDL principle," *IEEE Trans. Acoustics, Speech, and Signal Processing*, vol. 37, pp. 1190-1196, Aug. 1989.

[59] M. Wax, "Detection and localization of multiple sources via the stochastic signals model," *IEEE Trans. Signal Processing*, vol. 39, pp. 2450-2455, Nov. 1991.

[60] T.W. Anderson, "Asymptotic theory for principal component analysis," *Ann. J. Math. Stat.*, vol. 34, pp. 122-148, 1963.

[61] G. Xu, R.H. Roy, and T. Kailath, "Detection of number of sources via exploitation of centro-symmetry property," *IEEE Trans. Signal Processing*, vol. 42, pp. 102-112. Jan. 1994.

[62] M.E. Kotanchek and J.E. Dzielski, "Subspace stability in high resolution direction finding and signal enumeration," *IEEE Proceedings on Autonomous Underwater Vehicle Technology*, pp. 192-199, Jun. 1996.

[63] Y. Shaolin, K. Hengyu, H. Jiechang, W. Xiongbin, T. Jiansheng, and W. Biyang, "Detection of the number of signal sin super-resolution ocean surface current algorithm for OSMAR2000," *IEEE Conference and Exhibition on Oceans*, vol. 2, pp. 962-966, 2001.

[64] J-S. Jiang, M. Ingram, "Path Models and MIMO capacity for measured indoor channels at 5.8 GHz," *IEEE International Symposium on Antenna Technology and Applied Electromagnetics*, pp. 601-607, Aug. 2002.

[65] A. Di and L. Tian, "Matrix decomposition and multiple source location," *ICASSP*, vol. 9, pp. 722-725, Mar. 1984.

[66] A. Di, "Multiple source location – A matrix decomposition approach," *IEEE Trans. Acoustics, Speech, Signal Processing*, vol. ASSP-33, pp. 1086-1091, Oct. 1985.

[67] H. Krim and J.H. Cozzens, "A data-based enumeration technique for fully correlated signals," *IEEE Trans. Signal Processing*, vol. 42, pp. 1662-1668, Jul. 1994.

[68] W. Chen, K.M. Wong, and J.P. Reilly, "Detection of the number of signals: A predicted Eigen-Threshold Approach," *IEEE Trans. Signal Processing*, vol. 39, pp. 1088-1991, May 1991.

[69] M. Wax, "Detection and localization of multiple sources in noise with unknown covariance," *IEEE Trans. Signal Processing*, vol. 40, pp. 245-249, Jan. 1992.

[70] C-M. Cho and P.M. Djuric, "Detection and localization of multiple sources via Bayesian and predictive densities," *IEEE International Conference on Acoustics, Speech, and Signal* Processing, vol. 4, pp. 57-60, Apr. 1993.

[71] S.D. Silverstein, "A new use of ESPRIT for detection and model order estimation," *IEEE Signals Processing Letters*, vol. 1, pp. 147-149, Oct. 1994.

[72] K. Pahlavan and A. H. Levesque, *Wireless Information Networks*, John Wiley & Sons, Inc. 1995.

[73] J. Fuhl, J.P. Rossi, and E. Bonek, "High-resolution 3-D direction-of-arrival determination for urban mobile radio," *IEEE Trans. on Antennas Propagation*, vol. 45, pp. 672-682, Apr. 1997.

[74] M. Stoytchev, J.B. Raveche, and H.F. Safar, "Joint spatial and temporal characterization of the wideband wireless communication channel for MIMO applications," *IEEE Radio and Wireless Conference*, pp. 233-236, Aug. 2001.

[75] H. Xu, V. Kukshya, and T.S. Rappaport, "Spatial and temporal characteristics of 60-GHz indoor channels," in *IEEE Journal on Selected Areas in Communications*, vol. 20, pp. 620-630, Apr. 2002.

[76] Manufacturer's product specification for cable UFB142C (Micro-coax). The URL of the manufacturer is http://www.microcoax.com.

[77] K. Fukunaga, *Introduction to Statistical Pattern Recognition, 2nd Edition*. Boston: Academic Press, Inc., 1990.

[78] B. Efron, "Estimating the error rate of a prediction rule: Improvement on cross-validation," J. Amer. Statist. Ass. Vol. 78, pp. 316-331, 1983.

[79] D. Chizhik, G.J. Foschini, M.J. Gans, R.A. Valenzuela, "Keyholes, correlations, and capacities of multielement transmit and receive antennas," *IEEE Trans. Wireless Communications*, vol. 1, pp. 361-368. Apr. 2002.

[80] P.F. Driessen, G.J. Foschini, "On the capacity formula for multiple input-multiple output wireless channels: A geometric interpretation," *IEEE Trans. Communications*, vol. 47, pp. 173 – 176, Feb. 1999.

[81] P. Kyritsi, "MIMO capacity in free space and above perfect ground: Theory and experimental results," *IEEE Symposium on Personal, Indoor, and Mobile Radio Communications*, vol.1, pp. 182-186, Sep. 2002.

[82] A. Hutter, F. Platbrood, and J. Ayadi, "Analysis of MIMO capacity gains for indoor propagation channels with LOS component," *IEEE International Symposium on Personal, Indoor and Mobile Radio Communications*, vol. 3, pp. 1337-1341, Sep. 2002.

[83] K-H Li, M.A. Ingram, and A.V. Nguyen, "Impact of clustering in statistical indoor propagation models of link capacity," *IEEE Trans. Communications*, vol. 50, pp. 521-523, Apr. 2002.

[84] A. Burr, "Evaluation of capacity of indoor wireless MIMO channeling using ray tracing," *IEEE International Seminar on Broadband Communication*, pp. 28-1 – 28-6, 2002.

[85] M.A. Ingram, "Measurement, modeling and performance of the MIMO channel," in *Adaptive Antenna Arras: Trends and Applications*, Satish Chandran, ed., Springer Verlag, ISBN 3-540-20199-8, to appear April 2004.

[86] M.C. Lawton, J.P. McGeehan, "The application of a deterministic ray launching algorithm for the prediction of radio channel characteristics in small-cell environment," *IEEE Trans. Vehicular Technology*, vol. 43, pp. 955-969, Nov. 1994.

[87] S.R. Saunders, *Antennas and propagation for wireless communication systems*, Wiley, 1999.

[88] R.S. Blum, J.H. Winters, and N.R. Sollenberger, "On he capacity of cellular systems with MIMO," *IEEE Communication Letters*, vol. 6, pp. 242-244, Jun. 2002.

[89] S. Sandhu, R.U. Nabar, D.A. Gore, and A. Paulraj, "Near-optimal selection of transmit antennas for a MIMO channel based on Shannon capacity," *IEEE Conference on Signals, Systems, and Computers*, vol. 1, pp. 567-571, 2000.

[90] A.F. Molisch, M.Z. Win, "MIMO systems with antenna selection," *IEEE Microwave Magazine*, vol. 5, pp. 46-56, Mar. 2004.

[91] J-S. Jiang and M.A. Ingram, "Distributed source model for short range MIMO," *to be published in IEEE Vehicular Technology Conference*, Fall 2003.

[92] J.H. Mathews, *Numerical Methods for Computer Science, Engineering, and Mathematics*, Prentice-Hall, Inc., 1987.

[93] V. Jungnickel, V. Pohl, and C. von Helmolt, "Experiments on the element spacing in multi-antenna systems," *IEEE Vehicular Technology Conference*, vol. 2, pp. 1124-1126, Apr. 22-25, 2003.

[94] Personal communication with V. Jungnickel, Mar. 2004.

[95] R.L. Bratter, "Commercial success in the MEMs marketplace," *IEEE International Conference on Optical MEMs*, pp. 29-30, Aug. 2000.

[96] K. U-Yen and S.J. Kenney, "An optimization technique for low-loss nxm microwave switch matrices," *IEEE Radio and Wireless Conference*, pp. 341-344, Aug. 10-13, 2003.

[97] H. Lee and F. Li, "An eigenvector technique for detecting the number of emitters in a cluster," *IEEE Trans. Signal Process.*, vol. SP-42, pp. 2380-2388, Sep. 1994.

[98] P. Kyritsi, D.C. Cox, R.A. Valenzuela, and P.W. Wolniansky, "Correlation analysis based on MIMO channel measurements in an indoor environment," *IEEE Journal On Selected Areas in Communications*, vol. 21, pp. 713-720, Jun. 2003.

[99] D.P. McNamara, M.A. Beach, P. Karlsson, and P.N. Fletcher, "Initial characterization of multiple-input multiple-output (MIMO) channels for space-time Communication," *IEEE Vehicular Technology Conference*, vol. 3, pp. 1193-1197, Fall 2000.

[100] G.L. Turin, "Communication through noisy, random-multipath channels," in *1956 IRE Convention Record*, Part 4, pp. 154-166.

[101] M.J. Gans, "A power spectral theory of propagation in the mobile radio environment," *IEEE Trans. Vehichlar Technology*, vol. VT-21, pp. 27-38, Feb. 1972.

[102] W.C.Y. Lee, *Mobile Communications Engineering*, McGraw Hill Publications, NY, 1982.

[103] S.P. Stapleton, X. Carbo, and T. Mckeen, "Tracking and diversity for a mobile communications base station array antenna," *IEEE Vehicular Technology Conference*, pp. 1695-1699, 1996.

[104] P. Petrus, *Novel Adaptive Array Algorithms and Their Impact on Cellular System Capacity*, Ph.D. Dissertation, Virginia Tech, Blacksburg, VA, Mar. 1997.

[105] P. Petrus, J.H. Reed, and T.S. Rappaport, "Effects of directional antennas at the base station on the Doppler spectrum," *IEEE Communications Letter*, vol. 1, Mar. 1997.

[106] J.C. Liberti, *Analysis of CDMA Cellular Radio Systems Employing Adaptive Antennas*," Ph.D. Dissertation, Virginia Tech, Blacksburg, VA, Sep. 1995.

[107] J.C. Liberti and T.S. Rappaport, " A geometrically based model for line-of-sight multipath radio channels," *IEEE Vehicular Technology Conference*, pp. 844-848, Apr. 1996.

[108] P. Zetterberg and B. Ottersten, "The spectrum efficiency of a base station antenna array system for spatially selective transmission," *IEEE Vehicular Technology Conference*, 1994.

[109] P. Zetterberg, *Mobile Communication with Base Station Antenna Arrays: Propagation Modeling and System Capacity*, Thesis, Royal Institute of Technology, Stockholm, Sweden, Jan. 1995.

[110] P. Zetterberg and P.L. Espensen, "A downlink beam steering technique for GSM/DCS1800/PCS1900," *IEEE International Symposium on Personal, Indoor and Mobile Radio Communications*, Taipei, Taiwan, Oct. 1996.

[111] H. Hashemi, "The indoor radio propagation channel," *Proceedings of IEEE*, vol. 81, pp. 943-968, Jul. 1993.

[112] G.L. Stuber, *Principles of Mobile Communication, 2nd Printing*, Kluwer Academic Publishers, 1996.

[113] G.D. Durgin, T. S. Rappaport, "Theory of multipath shape factors for small-scale fading wireless channels," *IEEE Trans. on Antenna and Propagation*, vol. 48, pp. 682-693, May 2000.

[114] J.A. Cadzow, "Multiple source location – The signal subspace approach," *IEEE Trans. Acoustics, Speech, and Signal Processing*, vol. 38, pp. 1110-1125, Jul. 1990.

[115] M. Viberg and A.L. Swindlehurst, "A Bayesian approach to auto-calibration for parametric array signal processing," *IEEE Trans. Signal Processing*, vol. 42, pp. 3495-3507, Dec. 1994.

[116] J.H. Cozzens and M.J. Sousa, "Source enumeration in a correlated signal environment," *IEEE Trans. Signal Processing*, vol. 42, pp. 304-317, Feb. 1994.

[117] S. Prasad and B. Chandna, "An augmented smoothed rank profile algorithm for determination of source coherency structure," *IEEE Trans. Signal Processing*, vol. 37, pp. 1144-1146, Jul. 1989.

[118] F.R. Hill and R.L. Pickholtz, "Estimating the number of signals using the eigenvalues of the correlation matrix," *IEEE Military Communications Conference*, vol. 2, pp. 353-358, Oct. 1989.

[119] J.A. Cadzow, " Signal subspace method of multiple source location," *IEEE 5th Workshop on Spectrum Estimation and Modeling*, pp. 74-78, Oct. 1990.

[120] J.A. Cadzow, Y.S. Kim, W.Ma, and D.C. Shiue, "Resolution of spatially close broadband coherent sources incident on a general array," *International Conference on Acoustics, Speech, and Signal Processing*, vol. 5, pp. 2662-2665, Apr. 1988.

[121] J.P. Rossi, J.P. Barbot, and A.J. Levy, "Theory and measurement of the angle of arrival and time delay of UHF radiowave using a ring array," *IEEE Trans. Antennas Propagation*, vol. 45, pp. 876-884, May 1997.

[122] Y.L.C. de Jong and M.H.A.J. Herben, "High-resolution angle-of-arrival measurement of the mobile radio channel," *IEEE Trans. Antennas Propagation*, vol. 47, pp. 1677-1687, Nov. 1999.

[123] Q.H. Spencer and A.L. Swindlehurst, "Some results on channel capacity when using multiple antennas," *IEEE Vehicular Technology Conference*, vol. 2, pp. 681-688, Fall 2000.

[124] A.L. Swindlehurst, B. Ottersten, R. Roy, and T. Kailath, "Multiple Invariance ESPRIT" *IEEE Trans. Signal Processing*, vol.40, pp. 867-881. Apr. 1992.

[125] Q. Spencer, M. Rice, B. Jeffs, and M. Jensen, "Indoor wideband time/angle of arrival multipath propagation results," *IEEE Vehicular Technology Conference*, vol. 3, pp. 1410-1414, May 1997.

[126] Q. Spencer, M. Rice, B. Jeffs, and M. Jensen, "A statistical model for angle of arrival in indoor multipath propagation," *IEEE Vehicular Technology Conference*, vol. 3, pp. 1415-1419, May 1997.

[127] J.W. Wallace and M.A. Jensen, "Modeling the indoor MIMO wireless channel," *IEEE Trans. Antennas and Propagation*, vol. 50, pp. 591-599, Mar. 2002.

[128] H.B. Lee, "Eigenvalues and eigenvectors of covariance matrices for signals closely spaced in frequency," *IEEE Trans. Signal Process.*, vol. SP-40, pp. 2518-2535, Oct. 1994.

[129] W. Xu, J. Pierre, and M. Kaveh, "Practical detection with calibrated arrays," *Proc. Sixth IEEE-SP Workshop Statistical Signal Array Processing*, Oct. 1992.

[130] C.M. Tan, M.A. Beach, and A.R. Nix, "Enhanced-SAGE algorithm for use in distributed-source environments," *Electronics Letters*, vol. 39, pp. 697-698, April 17, 2003.

[131] J.B. Andersen and K.I. Pedersen, "Angle-of-arrival statistics for low resolution antennas," *IEEE Trans. on Antennas and Propagations*, vol. 50, pp. 391-395, Mar. 2002.

[132] C.C. Chong, D.I Laurenson, C.M. Tan, S. McLaughlin, M.A. Beach, and A.R. Nix, "A.R. Joint detection-estimation of directional channel parameters using the 2-D frequency domain SAGE algorithm with serial interference cancellation," *IEEE International Conference on Communications*, vol. 2, pp. 906-910, May 2002.

[133] J.A. Fessler and A.O. Hero, "Space-alternating generalized expectation-maximization algorithm," *IEEE Trans. Signal Processing*, vol. 42, pp. 2664-2677, Oct. 1994.

[134] B.H. Fleury, M. Tschudin, R. Heddergott, D. Dahlhaus, and K.I. Pedersen, "Channel parameter estimation in mobile radio environments using the SAGE algorithm," *IEEE Journal on Selected Areas in Communications*, vol. 17, pp. 434-450, Mar. 1999.

[135] S. Catreux, L.J. Greenstein, and V. Erceg, "Some results and insights on the performance gains of MIMO systems," *IEEE Journal on Selected Areas in Communications*, vol. 2, pp. 839-847, Jun. 2003.

[136] R.A. Valenzuela, "A ray tracing approach for predicting indoor wireless transmission," *Proc. IEEE Vehicular Technology Conference*, pp. 214-218,1993.

[137] A. Paulraj and T. Kailath, "Eigenstructure methods for direction of arrival estimation in the presence of unknown noise fields," *IEEE Trans. Acoustics, Speech, and Signal Processing*, vol. ASSP-34, pp. 13-20, Feb. 1986.

[138] A.A.M. Saleh and R.A. Valenzuela, "A statistical model for indoor multipath propagation," *IEEE Journals on Selected Areas of Communications*, SAC-5:128-13, Feb. 1987.

PUBLICATIONS

[1] J-S. Jiang and M.A. Ingram, "Spherical wave model for short range MIMO," *2nd revision, submitted to IEEE Trans. Communications.*

[2] J-S. Jiang and M.A. Ingram, "Throughputs of two interfering open-loop MIMO links over measured whitened channels at 5.8 GHz," *submitted to IEEE Trans. on Communications.*

[3] J-S. Jiang and M.A. Ingram, "Robust detection of number of sources using the transformed rotational submatrix," *submitted to IEEE Signal Processing Letters*.

[4] J-S. Jiang and M.A. Ingram, "Enhancing the performance of measured MIMO channels by adapting the element positions," *submitted to IEEE Wireless Communications Letters*.

[5] J-S. Jiang and M.A. Ingram, "Robust Detection of Number of Sources Using the Transformed Rotational Matrix," *IEEE Wireless Communications and Networking Conference*, Atlanta, GA, Mar. 21-25, 2004.

[6] J-S. Jiang, M.F. Demirkol, and M.A. Ingram, "Measured capacities at 5.8 GHz of indoor MIMO systems with MIMO interference," *IEEE Vehicular Technology Conference*, Fall 2003.

[7] J-S. Jiang and M.A. Ingram, "Distributed source model for short range MIMO," *IEEE Vehicular Technology Conference*, Fall 2003.

[8] J-S. Jiang and M.A. Ingram, "Comparison of beam selection and antenna selection techniques in indoor MIMO systems at 5.8 GHz," *IEEE Radio and Wireless Conference*, pp. 179-182, Aug. 2003.

[9] J-S. Jiang and M.A. Ingram, "Enhancing measured MIMO capacity by adapting the locations of the antenna elements," *IEEE International Symposium on Personal, Indoor, and Mobile Radio Communications*, vol.3, pp. 1027-1031, Sep. 2002.

[10] J-S. Jiang and M.A. Ingram, "Path models and MIMO capacity for measured indoor channels at 5.8 GHz," *IEEE International Symposium on Antenna Technology and Applied Electromagnetism*, pp. 601-607, Aug. 2002.

VITA

Jeng-Shiann Jiang was born in Tainan City, Taiwan, on August 26, 1970. He obtained the Bachelor of Science and Master of Science degrees in Electrical Engineering at National Sun Yat-Sen University, Kaohsiung, Taiwan, in June 1992 and June 1994, respectively. From August 1994 to May 1996, he served as an Army Lieutenant in Taiwan. From 1996 to 1997, he was a hardware circuit design engineer in D-Link Network Corporation, responsible for the circuit design of IEEE 802.3 Fast Ethernet adapters. From 1997 to 1998, he was a software engineer with the Industrial Technology Research Institute (ITRI) in Taiwan. In September 1998, he enrolled in the graduate school at Georgia Institute of Technology. From 1999 to 2000, he was a teaching assistant with the School of Electrical and Computer Engineering at the Georgia Institute of Technology. From 2000 to the present, he has been a research assistant of Smart Antenna Research Laboratory at the Georgia Institute of Technology. He obtained the Master of Science and the Doctor of Philosophy degrees in Electrical and Computer Engineering at Georgia Institute of Technology in May 2000 and July 2004, respectively. His research interests include MIMO technology, wireless channel measurement and modeling, parameter estimation, orthogonal frequency division multiplexing (OFDM), and space-time coding.